2020-11-26 14:11:03 B(nT) I=50(kA) h0= 95 D= 21(km)

Swarm4Anom - Final Report

CBK
AGH
Obsee

Contract No.: 4000112769/14/ NL /FF/gp

http://swarm4anom.cbk.waw.pl/s4a/s4aTLEINDD

This document provides a summary of activities performed within the Swarm4Anom project.

- Section 1 describes output files from theoretical analysis utilizing the TIEGCM model. This part was used in the analysis concentrated on the long-term trends and climatological approach in the ionospheric studies.

- Section 2 describes capabilities of Swarm in detection of magnetic field fluctuations related to strong lightning activity.

References

[1] - M. Strumik, J. Slominski, E. Slominska, J. Mlynarczyk, J. Blecki, R. Haagmans, A. Kulak, M. Popek, K. Martynski, R. Wronowski, *Experimental Evidence of a Link Between Lightning and Magnetic Field Fluctuations in the Upper Ionosphere Observed by Swarm*, accepted for Geophysical Research Letters, doi number will be provide as soon as possible.

[2] - Slominska, E., Strumik, M., Slominski, J., Haagmans, R., Floberghagen, R. (2020). *Analysis of the impact of long-term changes in the geomagnetic field on the spatial pattern of the Weddell Sea Anomaly*. Journal of Geophysical Research: Space Physics, 125, e2019JA027528. `https://doi.org/10.1029/2019JA027528`

Access to data

- Access to Swarm A/B/C magnetic field fluctuations data
  `http://swarm4anom.cbk.waw.pl/gauss/SIG/`
- Access to Swarm A/B/C I_{NDD} index product:
  `http://swarm4anom.cbk.waw.pl/s4a/prodcdf/`
- Access to the TIEGCM output data product (netcdf files)
  `http://swarm4anom.cbk.waw.pl/TIEGCM_OUT/`

Project webpage: `http://swarm4anom.cbk.waw.pl/s4a/s4aTLEINDD`

1 Climatological approach based on the TIEGCM model

Main result from the first part of the study was published in (2), which discusses the impact of long-term changes in the geomagnetic field on the spatial pattern of the Weddell Sea Anomaly (WSA). The Weddell Sea Anomaly, belonging to the region near the tip of the Antarctic Peninsula, Falklands, and surrounding seas, is the best-known example of ionospheric reversed diurnal cycle. The study investigates whether and to what extent long-term changes in the geomagnetic field influence spatial morphology of the WSA. The major concept centers on a normalized density difference index, serving as a measure of difference between dayside and nightside ionospheric density. Through combined analysis of in situ ionospheric electron density data from past mission CHAMP, ongoing ESA mission Swarm, and simulations based on the NCAR TIEGCM model, we examine changes in the spatial pattern of the WSA-like anomalies, which could be linked to long-term changes in the geomagnetic field. A series of simulations provides theoretical analysis of changes in the morphology of the WSA on time scales longer than several decades. Numerical analysis shows that from the time when the WSA was discovered (around 1960) till present, maximum of the WSA has migrated by approximately 7° in longitude towards the Pacific Ocean, showing clear westward drift, consistent with temporal evolution of the geomagnetic dipole component.

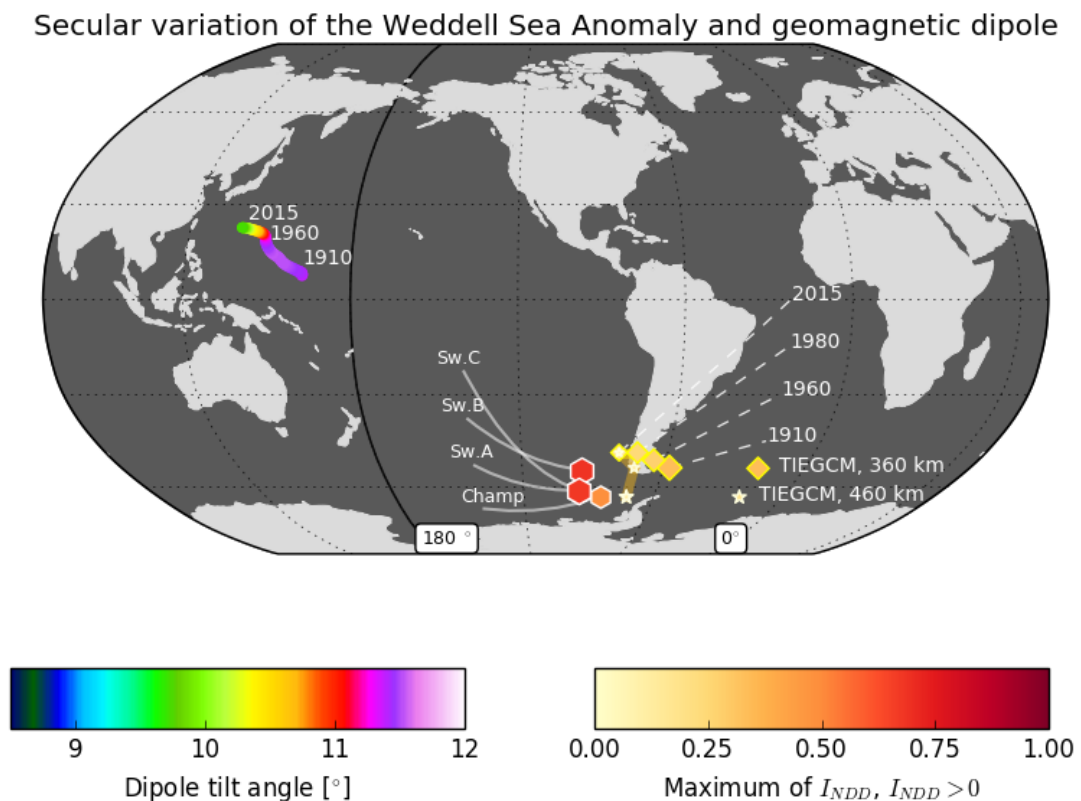## 1.1 Ionospheric representation derived from the TIEGCM model

Figure 1: Drift of the central part of the WSA, juxtaposed with derived drift of magnetic dipole component

In a part of the project related to the investigation of the WSA-related phenomena, the TIEGCM

model was studied as providing possibly more accurate predictions in comparison with the standard IRI model of the ionosphere. The TIEGCM model incorporates fundamental ionospheric physics that make it potentially helpful in interpretation of Swarm (and other satellite) measurements. The inner boundary condition in this model is determined by the atmospheric dynamics (including tides). The influence of the ionizing solar UV irradiance can be included by using F10.7-index proxy, while the state of the magnetosphere may be parameterized, e.g., by using the cross-tail potential and the hemispheric power of auroral precipitation. The elements of the TIEGCM setup that we describe here are only one possible choice from several options of setting up a TIEGCM simulation. With a properly prepared setup, the TIEGCM code solves an appropriate set of partial differential equations and phenomenological relations generating a time-dependent solution on a spherical grid (formally based on constant-pressure levels) extending from approx. 100 to 700 km above the Earth. Numerical solutions from the TIEGCM model can be directly compared with satellite measurements. As an example illustrating possible utilization of the numerical solutions,
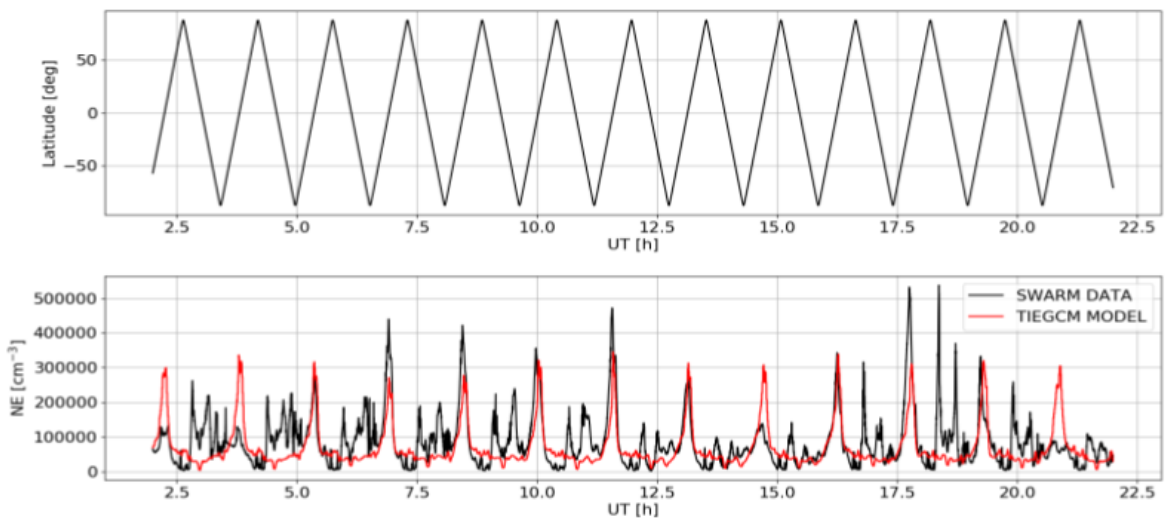

Figure 2: Comparison of the simulated (red line) electron density and measurements (black line) along the Swarm trajectory (lower panel). Upper panel shows the geographic latitude evolution for the time interval presented in the lower plot.

Fig.2 contains a comparison of the electron density obtained satellite measurements. We can see a general correspondence between the two time series, although the model (red line) shows a more regular (almost periodic) pattern as compared to the satellite measurements (black line) that are more irregular. One should note that in this simulation, the TIEGCM model was run with constant solar-input parameters, thus the obtained solution corresponds to quiet-Sun conditions with fixed irradiance and solar wind parameters. The real Swarm measurements obviously contain entire variability occurring in nature. This type of direct comparison opens up many possibilities of investigating the residua between the simulation and measurements and identifying physical mechanisms responsible for departures. In this regard, an interesting option is related to a long (2002-2020) time-dependent TIEGCM simulation, where the model is driven by direct measurements of F10.7 index and geomagnetic indices. Such simulation would provide a well-established basis for direct comparisons with measurements from low-Earth-orbit satellites.

During the project a number of visualization techniques was studied that made it possible to obtain a 3D insight into the simulated ionospheric dynamics. Examples of the visualizations are presented below.
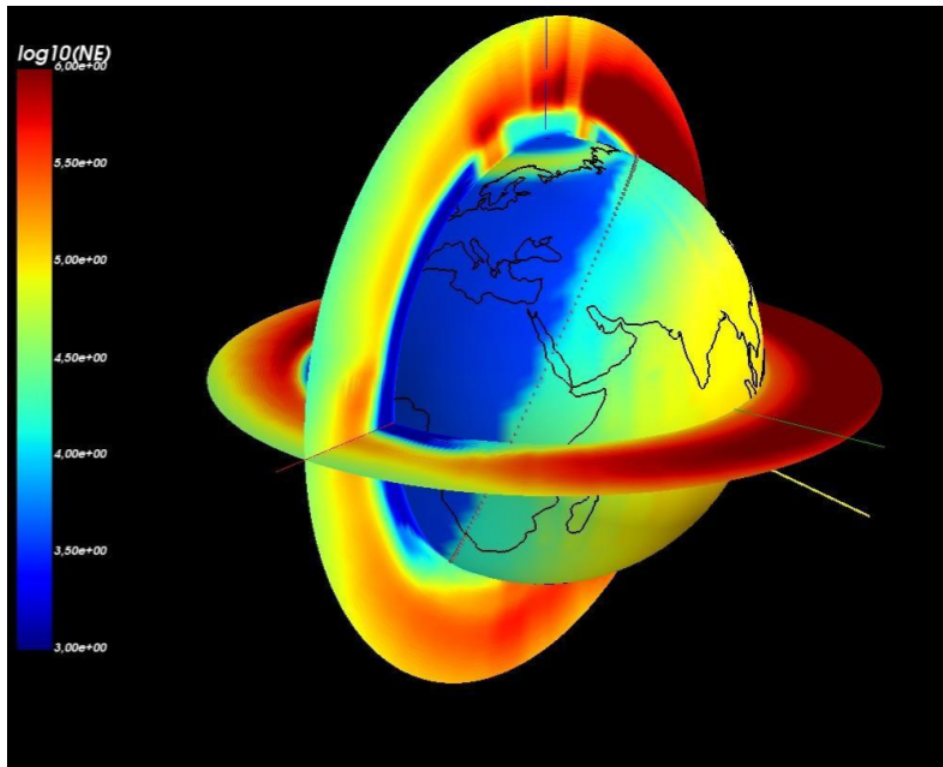
Figure 3: Tomographic view of the electron density in the simulated ionosphere.

Fig.3 shows a tomographic view of the electron density N_e in the simulated ionosphere. A spherical surface shows N_e distribution at approx. 100 km above the Earth, close to the inner boundary condition in the TIEGCM model. Two mutually perpendicular discs show the distribution of NE in the ionospheric volume. Yellow line shows the direction towards the Sun, continents are shown by black contours, and the solar terminator - by black dots that coincide with abrupt density change on the sphere. The aspect ratio of the ionosphere thickness and the Earth radius was increased here purposely, to better visualize the distribution of NE in the ionospheric volume.
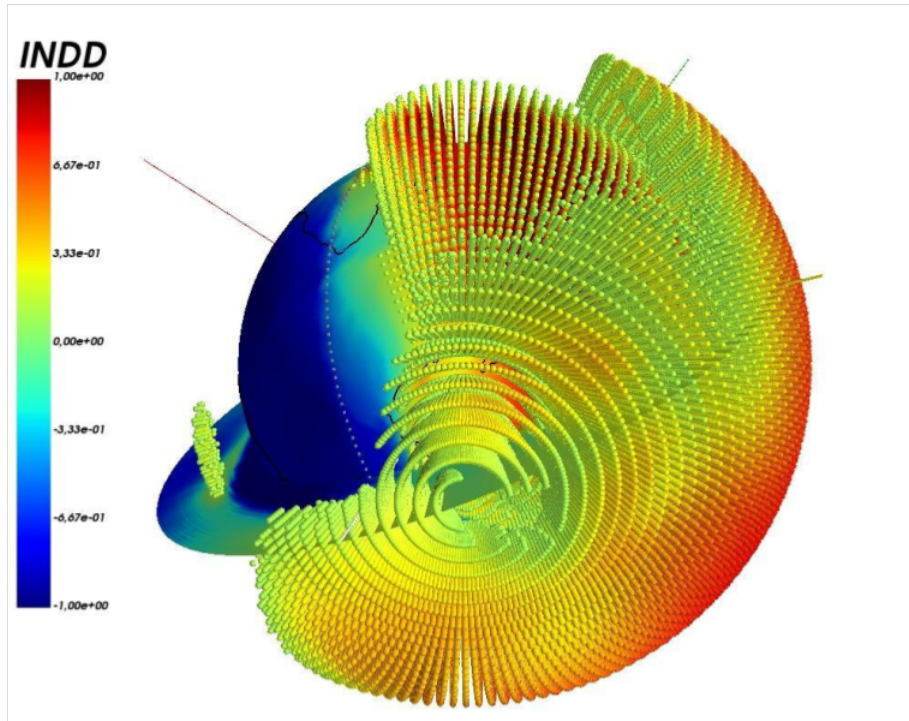

Figure 4: Visualization of grid points for which the index INDD>0.1, illustrating mechanisms related to the WSA phenomenon and similar anomaly in the equatorial region.

Other visualization presented in Fig.3 shows points of the TIEGCM grid, for which the INDD index is larger than 0.1. By using this type of visualization in the form of a movie, it is possible to identify a detailed scenario that leads to the appearance of the WSA. The time-dependent visualization (i.e. the movie) shows that the volume where INDD>0.1 crosses a meridional midnight-local-time plane periodically (every 24 hours) in the simulation.

The occurrence of INDD>0.1 volume at the meridional plane is correlated approximately with the midnight local time at the geographic location of the Weddell Sea. Interestingly enough, the TIEGCM solution also contains an equatorial anomaly seen in Fig.4 (small yellow-green group of points on the left). This type of visualization links commonly-used approaches based on constant-local-time maps used for investigating WSA with transient events occurring in a sequence of constant-universal-time maps. Since the TIEGCM model provides also information on the neutral and ExB velocity components, further development of this type of visualization/analysis techniques gives a possibility of pinpointing
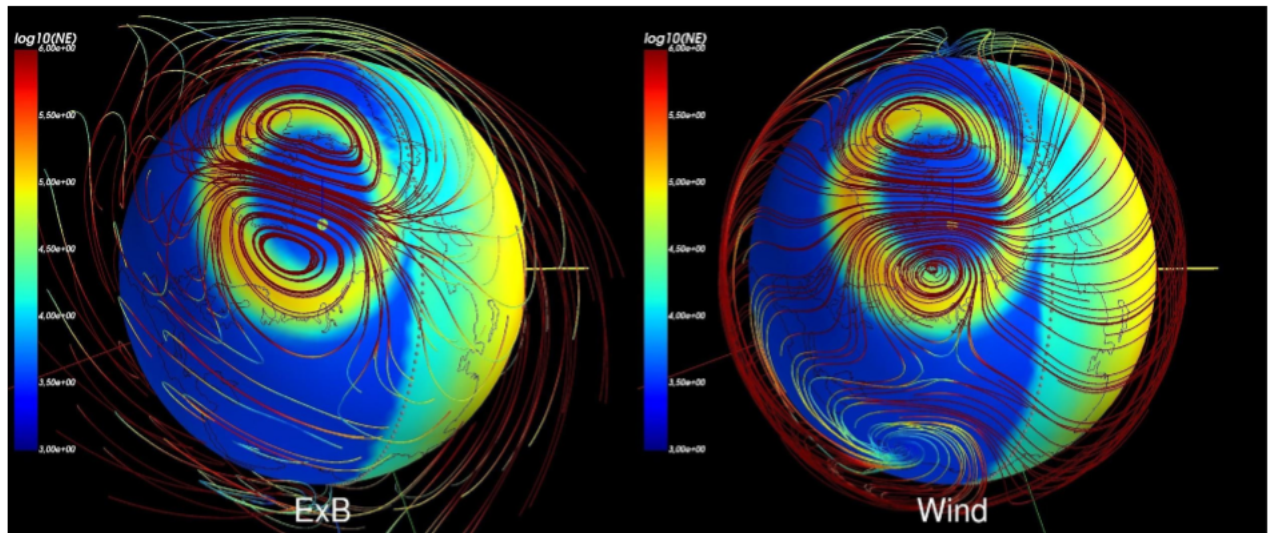
Figure 5: Streamline tracking of simulated ExB drift and neutral wind over-plotted onto the distribution of the electron density.

a detailed mechanism of generation of the WSA-like phenomenon in the simulation. This simulated mechanism can be then rigorously validated against satellite measurements by comparison of different physical quantities. Other visualization techniques investigated during the project combines the spatial distribution of a given scalar quantity (e.g., the electron density N_e) with streamline tracking for vector quantities (e.g., neutral and ExB velocity, magnetic field). An example of this type of visualization is shown in Fig. 5, where the electron density at the altitude of approx. 100 km is visualized on a sphere. Above the sphere, at higher altitudes, streamlines for ExB drift (on the left) and neutral velocity (on the right) are shown. The streamlines are locally tangent to the velocities. The visualization shows a north view, with the northern convection pattern visible as clearly associated with the location of the auroral oval. Different character of ExB and neutral flows is also seen in the plot, with the neutral velocity having much smaller radial component. In a movie containing a sequence of plots for different times, the time evolution of the simulated flows can be investigated as over-plotted on scalar quantities visualized on the sphere surface.

Combining streamline-tracking technique and surface-distribution or tomographic cuts can be useful for visualizing the physics of the ionosphere with the Swarm (or other satellite) trajectory over-plotted onto distributions of different physical quantities. Time-dependent visualizations of this type are particularly useful in the context of presenting temporal evolution of surface or volume distributions of various quantities with the emphasis on the understanding how the phenomena are translated into time series measured by a satellite. An example of such a plot is shown in Fig. 6.

These visualization techniques can be helpful in understanding connections between different physical quantities describing the state of the ionosphere.

1.2   TIEGCM for modeling of long-term trends in the ionosphere

Synthetic index I_{NDD} derived from the TIEGCM model supplements in-situ registrations from Swarm. For the present work, the TIEGCM 2.0 version is used with the double-resolution. Such configuration provides a grid of 2.5°×2.5° for latitude and longitude, and 58 pressure levels in the vertical direction. The lower boundary of the model is at approximately 97 km, and the upper boundary ranges from 400 to 700 km depending on the solar activity and settings of solar flux. The option for lower boundary forcing is switched off to minimize the contribution from factors other than the magnetic field. The purpose of using TIEGCM is to reconstruct the I_{NDD} index at the altitude of a satellite, thus we make an approximation between neighboring pressure levels in order to obtain the optimal agreement for the scale height.

Focusing on the role of the Earth's magnetic field and its impact on the formation of the WSA-like phenomena, we examined independent scenarios for the TIEGCM runs:

- Scenario #1: TIEGCM runs with a realistic magnetic field configuration determined by the IGRF model for a set of selected years.

- Scenario #2: Simplified magnetic field model reduced to dipole representation, with various configurations reflecting different eccentricity and tilt angle of the magnetic dipole.

Through all simulations, we used identical configuration of controlling parameters describing solar minimum and quiet geomagnetic conditions. The following parameters were used in the TIEGCM standalone runs: the solar flux ($F107 = 70$), the cross-tail potential ($CTPOTEN = 30$) and the hemispheric power ($POWER = 18$).

The model web-page (`http://www.hao.ucar.edu/modeling/tgcm/tiegcm2.0/userguide/html/`) provides more details on the physical meaning of the parameters used in the configuration and physics included in the model. Such configuration of model runs, minimizes the variability of the index originating from varying solar conditions and allows to isolate effects related to changes in the main magnetic field.
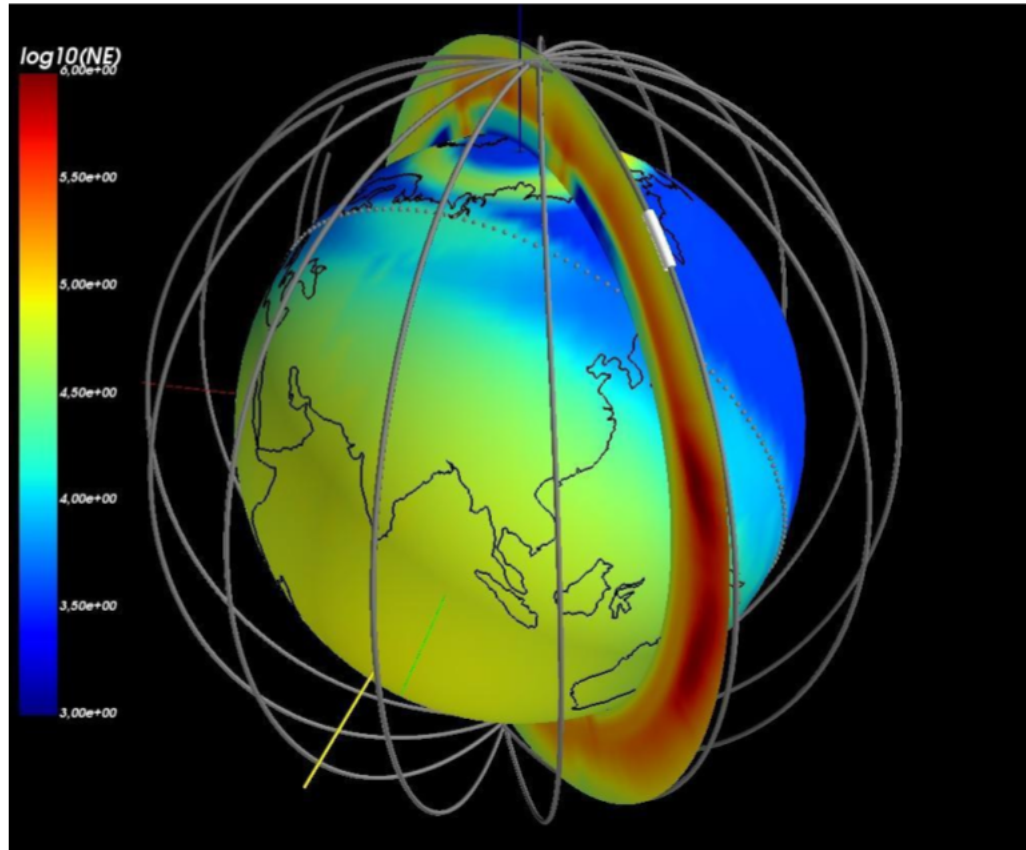
Figure 6: Visualization of the Swarm A trajectory overplotted onto the distribution of the electron density.

Before the index is computed, the TIEGCM output for the diagnostic field of the electron density N_e is converted to the LT frame. Using configurations defined above, we performed 5-day standalone runs, with the time-resolution of 10 minutes for March equinox, at two separate altitudes 360 km and 460 km. Simulations were carried out for the years 1910, 1960,1980, 2005, and 2015. Data are accessed from the following repository: `http://swarm4anom.cbk.waw.pl/TIEGCM_OUT/`.

- Earth's magnetic field represented as an straight dipole, placed in the centre of the Earth: tiegcm2.0_res2.5_mareqx
- Earth's magnetic field represented as a tilted dipole, placed in the centre of the Earth: tiegcm2.0_res2.5_mareqx_smin_sec_123_GSWN0_1900_004.nc
- Earth's magnetic field represented as dipole tilted in an opposite direction, placed in the centre of the Earth: tiegcm2.0_res2.5_mareqx_smin_sec_12-3_GSWN0_1900_004.nc
- Earth's magnetic field represented as an eccentric tilted dipole: tiegcm2.0_res2.5_mareqx_smin_sec_678_GSWN0_1900_004.nc
- Realistic Earth's magnetic field based on the IGRF model for years: 1910, 1960, 2005, 2015: tiegcm2.0_res2.5_mareqx_smin_sec_all_GSWN0_{1910,1960,2005,2016}_004.nc

2 Detection of magnetic field fluctuations related to lightning

Algorithm developed during the project allowed us to identify nearly 200 occurrences of magnetic field fluctuations, which originate from strong lightning activity. Three separate maps (Figure 7) for every spacecraft provide global representation of identified cases. Gathered minimal dataset gives opportunities to further study the phenomenon of wave propagation in the upper ionosphere.

The following section provides:

- Description of the algorithm applied to the detection of magnetic field fluctuations
- Description of lightning product prototype
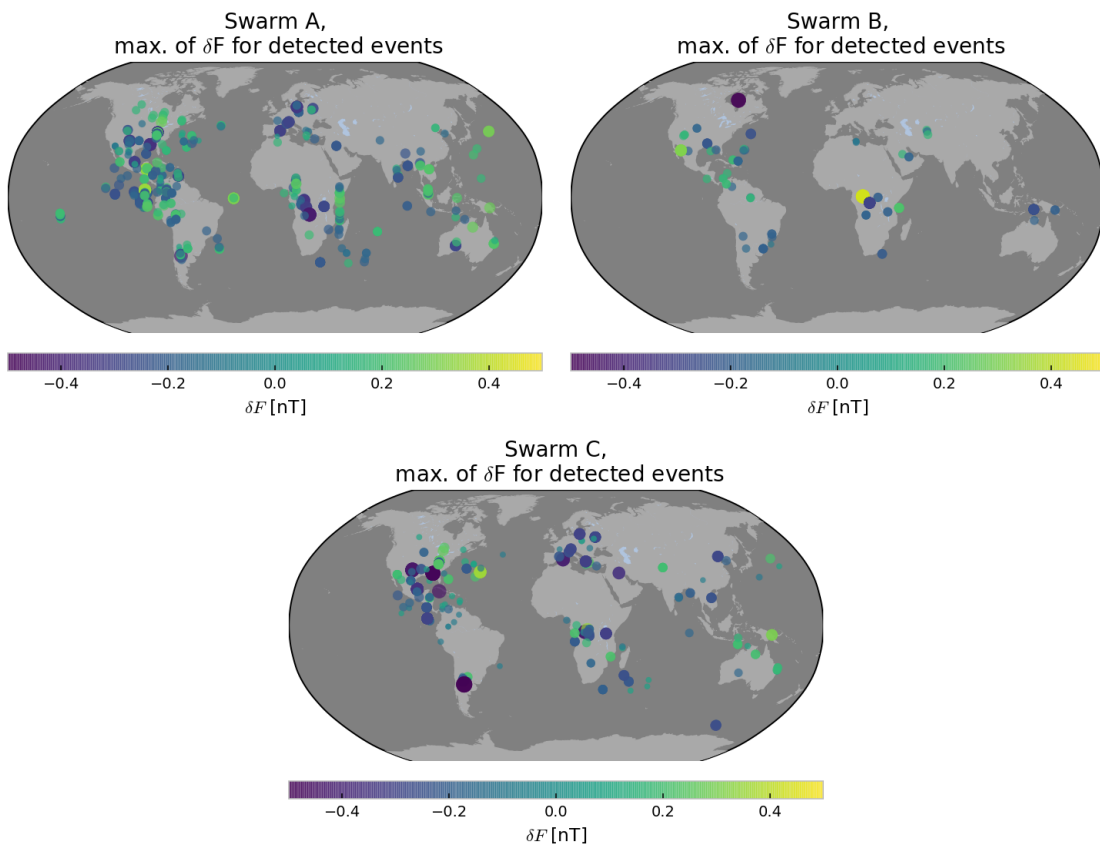- Example of successful case validated with ground-based observations

Figure 7: Global representation of lightning-triggered fluctuations detected by Swarm

2.1 Algorithm and data description

The algorithm for automatic detection exploits:

- 50 Hz magnetic field readings of the Vector Field Magnetometer (VFM) (SW_MAGx_HR data)
- Auxiliary dataset of lightning activity derived from the Worldwide Lightning Location Network. At the current stage of the product, only low-resolution dataset is used. In case of measurements taken over North and South America and surrounding Oceans, verification is performed with the

GLM (Global Lightning Mapper) dataset, high-resolution lightning data acquired onboard the geostationary satellites GEOS-16/17.

The algorithm distinguished following steps:

1. Scalar field (F) is computed from three components provided in the NEC frame

2. Fourth order polynomial approximation is applied over 128 samples (5-second time interval) to remove the main trend and extract perturbed signal.

3. If the fluctuation level of the scalar field exceeds minimal threshold (setup at the level of δ F>0.16 nT) signal is flagged as possible response to the lightning event.

4. Simultaneously it is checked if auxiliary data indicate occurrence of lightning events along the satellite track within the specified radius (up to 5 degrees on both sides). If it is so, differentiated gaussian source pulse function is fitted to obtain a set of parameters characterizing detected fluctuation.

5. Quality of the fit determines whether the signal is saved as an evidence of the lightning triggered signal.

Successful cases are stored in the CDF format under the following link:

http://swarm4anom.cbk.waw.pl/gauss/SIG/

The naming convention is as follows:

SIG_[A/B/C]_YYYY-MM-DDTHH:MM:SS.SS0000__xxxxx_????_256_vv.cdf

xxxxx - stands for the record number in the original MAGx_HR file

???? - denotes maximum amplitude of the detected peak vv - denotes type of data used for lightning information:

_00, _20, _40 - lightning information is taken from the GLM data

_0a - high-resolution lightning data, obtained by individual request for precise verification of events

_0w - low-resolution lightning data, acquired from the WWLLN server

Structure of the file is provided in the Table

Name of Variable	Description
Timestamp_light	Timestamp of the lightning event
light_lon	Lightning longitude
light_lat	Lightning latitude
light	Lightning event description [longitude, latitude, longitude_projected_onto_magnetic_field_line, latitude_projected_onto_magnetic_field_line, distance_to_the_satellite(km)]
Tim_resid	Timestamp of magnetic field residuals
T	Time in seconds around the detected spike
Lon_resid	Longitude of residuals along the satellite track
Lat_resid	Latitude of residuals along the satellite track
Trend	Three components and scalar field of the main trend [N,E,C,F] based on polynomial approximation
B_NEC	Three components [N,E,C] of the main trend
SIG	Residuals of three components of magnetic field [δN,δE,δC]
B_SIG	Residuals of the scalar magnetic field [δF]
Radius	Radius from the Earth Center

2.1.1 QuickLook data

In addition to the CDF SIG files, so called QuickLook data, representing all detected fluctuations, can be accessed from the following link: `http://swarm4anom.cbk.waw.pl/gauss/`. Three categories of images are provided:

- global representation of fluctuations detected on the selected day, separately for ascending and descending passes (example Figure 8). Naming convention of files helps to distinguish fluctuations only related to lightning events (files ending with suffix "_g.png") from all registered on the following day (files ending with suffix "_a.png").
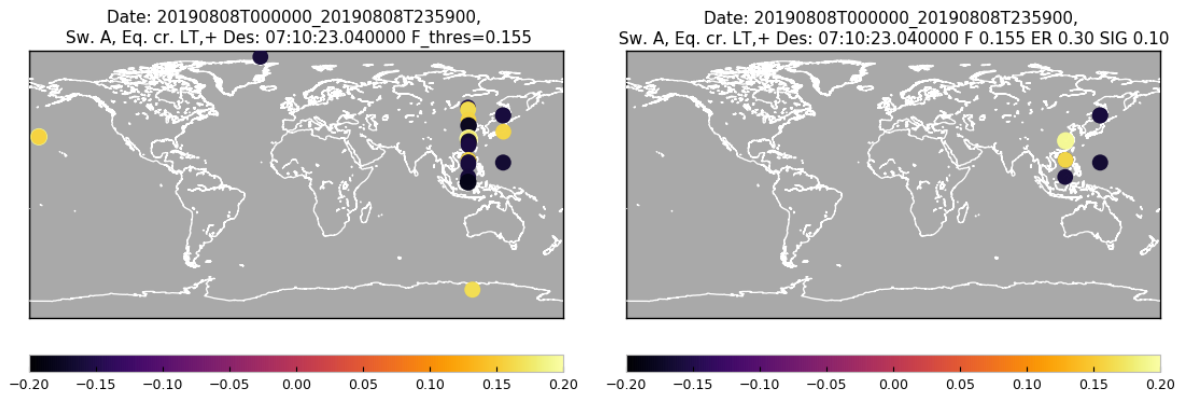

Figure 8: Global distribution of detected fluctuations on 20190808. Left panel: all cases - files ending with suffix "_a.png"; right panel: cases with verified lightning events - files ending with suffix "_a.png". Color scale represents amplitude of fluctuations of the scalar field

- plots showing synthetic function, and 30 samples of data representing detected peak. Each file of this type included coordinates of the peak (where it was detected), and exact UTC time (example Figure 9)
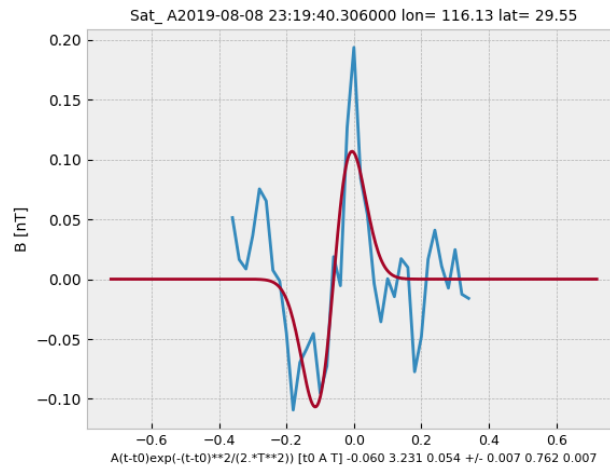

Figure 9: Synthetic function and Swarm fluctuations

  - Original file Swarm HR MAG file, in which fluctuation was detected:
    SW_OPER_MAGA_HR_1B_20190808T000000_20190808T235959_0505_

- – Repeated date and version of the algorithm:
  20190808_000000_20190808_235959_Mod12.012_
- – Timeframe of detected event: HHMMSS **_231940_**
- – Longitude and latitude, of detected fluctuation: **_116.1_29.5_**
- – Amplitude of fluctuation and quality of fit (under ideal condition second parameter should be equal to 1): **_0.19_0.24_f.png**

- Summary plot showing: spectrum of magnetic field fluctuations, time series derived from spectral fits, waveform of δF and combination of plasma parameters: N_e, T_e. Red stars denote lightning activity, while blue star indicated detected peak (example: Figure 10)
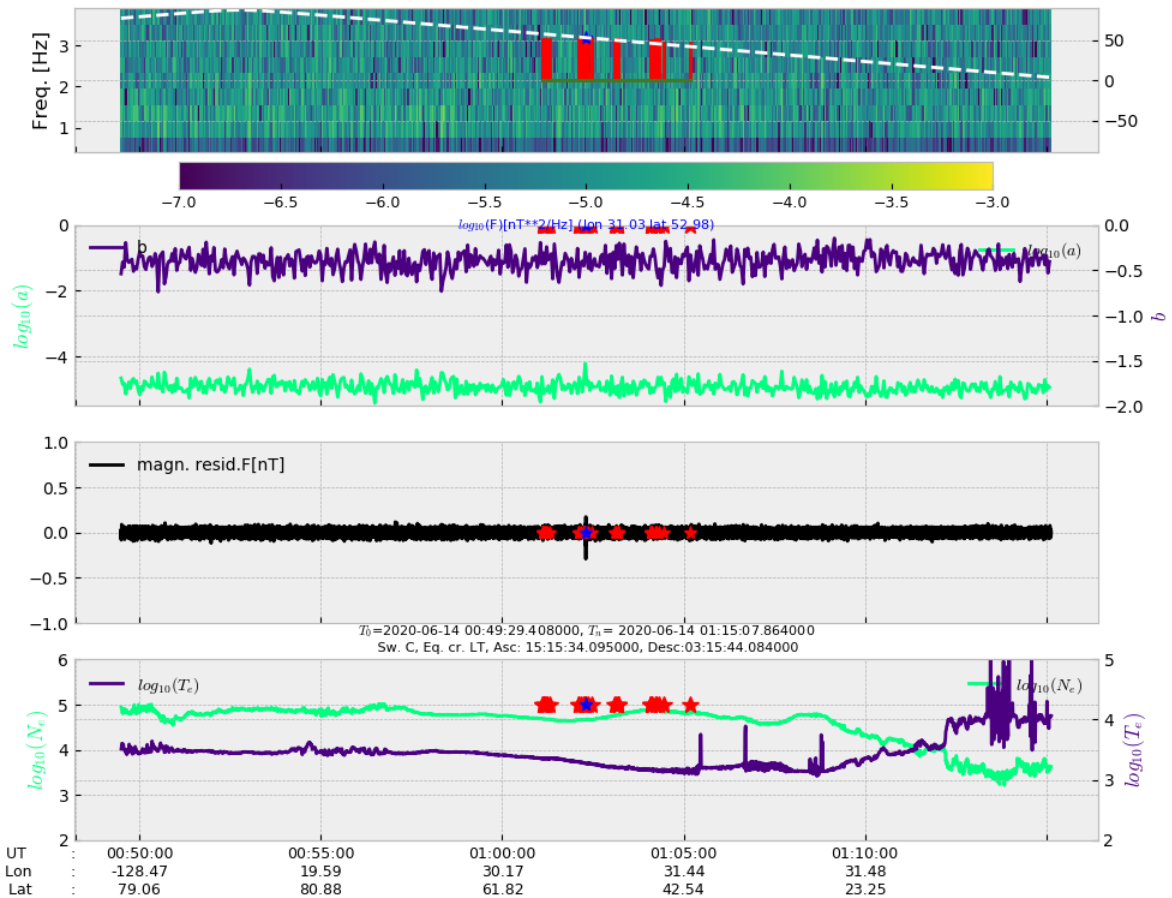

Figure 10: Power spectrum and waveform of magnetic field, combined with registered plasma parameters.

2.2 Data validation

Ground observations derived from the WERA ELF system were used for the cross-validation of selected cases. The system uses broadband low noise magnetometers designed by the Krakow ELF team, enabling us to observe very strong atmospheric discharges occurring anywhere on Earth. The WERA ELF system operates in the full configuration and consists of three stations, the Hylaty ELF station is located in a sparsely populated area of Poland, near the Bieszczady National Park, the Hugo station,

installed in May 2015, in located in Colorado, USA, and the Patagonia station, installed in March 2016, in southern Patagonia, Argentina.

Additionally for two separate cases, we managed to obtain optical confirmation of TLEs detected by the observer in Nydek, Czech Republic. These events were perfectly coinciding with the Swarm location (TLE location within the radius of 500 km from the magnetic field line leading to the Swarm satellite).
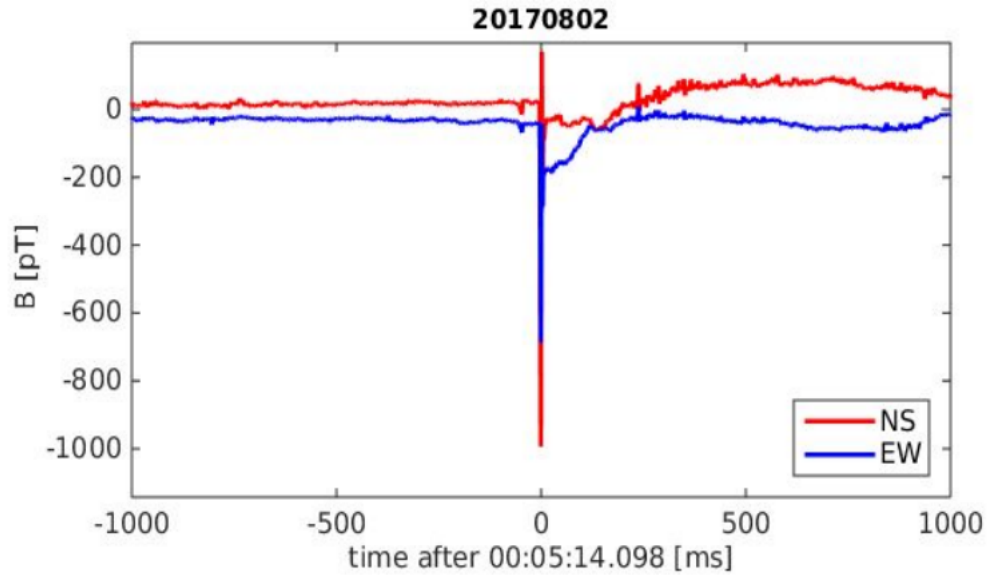

Figure 11: Ground observations of TLE events observed on August, 2 2017, timeseries of ULF data from the Hylaty station.

Figure 12: Ground observations of TLE events observed on August, 2 2017 - optical registrations captured in Nydek.

One of the successful cases is presented in Figures 11 - 13. Consecutive frames from the registered optical observations are juxtaposed with time-series from the Hylaty station as well as registrations from Swarm Alpha and Charlie.

Swarm registrations enclosing the timeframe of optical observations are presented in Figure 13, as simultaneous measurements of scalar field magnetic residuals derived from Swarm A (blue line), Swarm C (red line). A yellow vertical line denotes the time of the event displayed in the bottom panel. As one can notice, the prominent increase in the magnetic field readings is observed nearly 0.4 seconds after
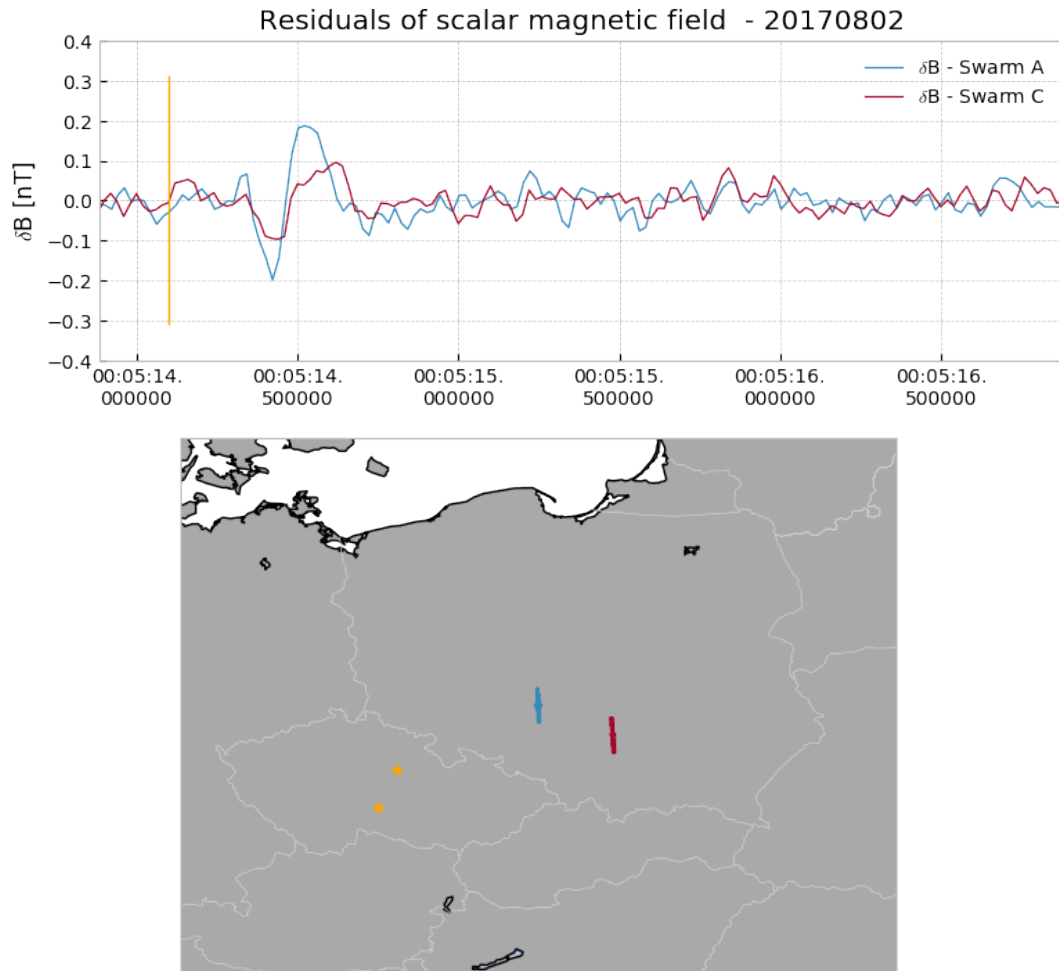
15

Figure 13: Upper panel: Time-series of scalar magnetic field fluctuations derived from Alpha and Charlie VFM registrations corresponding to the August, 2 2017 case. Bottom panel: Situational map showing the distance between the two Swarm satellites (Swarm A - blue, Swarm C - red) and lightning storm center (yellow points).

the ground-based observer registered the event. More intense fluctuations were detected on Swarm A, showing that the distance between the satellite track and the event plays a significant role in successfully detecting lightning-triggered signals onboard the spacecraft.
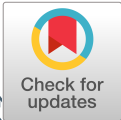
2.3 Scientific significance of delivered product - Cross-analysis with other satellite missions dedicated to lightning detection

A part of results regarding Swarm satellite observations of lightning effects as obtained during the project was discussed in a paper of Ref. (1) submitted for publication in Geophysical Research Letters. The paper focuses on providing an evidence of a causal relationship between lightning events and certain types of waveforms measured by the vector magnetometer onboard the Swarm satellites. To our knowledge this is the first direct experimental confirmation of a link between lightning and magnetic field fluctuations in the upper ionosphere in the ULF range. During the project a large number of cases was identified showing spatiotemporal correlation between lightning events and magnetic fluctuations measured by Swarm satellites in the upper ionosphere. The cases have been found all around the Earth, but in Ref. (1) only 11 cases were discussed, which had been confirmed by available data from the Geostationary Lightning Mapper (GLM) and the World ELF Radiolocation Array (WERA). Due to a limited coverage of GLM, these cases were located in the North and South America and adjacent oceanic regions. The paper of Ref. (1) describes data selection process that was used to identify spatiotemporal correlations between lightning and corresponding waveforms seen by Swarm satellites. The process involves searching for time intervals in the Swarm data stream that show good matching to a pre-defined signature derived during the project. Preliminary correlation with lightning events was done using public-access World Wide Lightning Location Network (WWLLN) data, while the final verification involved exact timing and location information from GLM. In Ref. (1) typical conditions are identified that make it possible to link lightning observations and associated magnetic fluctuations measured by low-Earth-orbit satellites. The conditions require the lightning-satellite geographic distance to be less than $5°$, while a typical time delay between lightning occurrence and associated satellite detection is 0.2-0.5 s. Typical amplitude of the fluctuations is 0.3-1.3 nT if the maximum variance component of the vector fluctuation is considered. These amplitudes were found to be linked to lightning events characterized by the charge moment from 375 to 11000 C km, as estimated from WERA radiolocator measurements. In terms of the fluctuation of the magnetic field strength, the amplitude is typically approx. 2 times smaller relative to the maximum-variance amplitude due to slightly elliptical polarization of the magnetic perturbations. Causal association between the lightning events and the magnetic fluctuations is evidenced in Ref. (1) by investigating relations between lightning and fluctuation properties. In this context, we discuss a relationship between the lightning charge moment and the amplitude of the fluctuations observed by satellites. Generally we found that correlation between the fluctuation amplitude and WERA-based charge moment estimates was better than that between the fluctuation amplitude and the intensity of top-of-clouds optical emissions seen by GLM. Another relation is also described in Ref. (1), which links the time delay between measurements of the same fluctuation by two Swarm satellites (A and C) and a difference in the distance of the satellites to the lightning location as inferred from the GLM observations. The findings described above are discussed in a more detail in Ref. (1) attached to this report. It is important to note that many other cases of possible correlation between lightning events and the magnetic fluctuations were found during the project. However since the cases are not located in the region covered by GLM observations, they were not described in Ref. (1).

2.4 Summary

- Currently Swarm is the only satellite mission which allows to study wave activity triggered by intense lightning in the frequency range below 10 Hz, on a daily basis.

- In particular analysis of fluctuations of all vector components should be considered as a next step of analysis, in order to allow classification of types of waves triggered various types of TLEs. In particular this would allow to determine when triggered wave has a typical character of an Alfven wave, or it is more magneto sonic type.

- Tested methodology proves, that combination of measurements from Alpha and Charlie clearly shows that amplitude of magnetic fluctuations with respect to the distance from the lightning source. Altitudinal dependence could be obtained from detailed analysis between lower pair and upper satellite.

- Although limited to the region of both American continents, cross-analysis with the GLM data provides a glimpse of possibilities for the joint-studies with other satellite missions, in particular obtained results are of high importance for upcoming Meteosat Third Generation Program. Meteosat Third Generation Program will provide lightning image data thanks to the Lightning Imager instrument, to support nowcasting applications. This will give opportunity to monitor the thunderstorm activity on the African continent.

Reprints of published papers

Correspondence to:
E. Slominska,
eslominska@icloud.com

Analysis of the Impact of Long-Term Changes in the Geomagnetic Field on the Spatial Pattern of the Weddell Sea Anomaly

Ewa Slominska[1] [iD], Marek Strumik[2] [iD], Jan Slominski[2] [iD], Roger Haagmans[3], and Rune Floberghagen[4]

[1]OBSEE, Warsaw, Poland, [2]Space Research Center PAS, Warsaw, Poland, [3]ESA ESTEC, Noordwijk, Netherlands, [4]ESA ESAC, Madrid, Spain

Abstract We simulated the impact of long-term changes in the geomagnetic field on the spatial pattern of the Weddell Sea Anomaly (WSA). The Weddell Sea Anomaly, belonging to the region near the tip of the Antarctic Peninsula, Falklands, and surrounding seas, is the best-known example of ionospheric reversed diurnal cycle. This paper investigates whether and to what extent long-term changes in the geomagnetic field influence spatial morphology of the WSA. The major concept centers on a normalized density difference index, serving as a measure of difference between dayside and nightside ionospheric density. Through combined analysis of in situ ionospheric electron density data from past mission CHAMP, ongoing ESA mission Swarm, and simulations based on the NCAR TIEGCM model, we examine changes in the spatial pattern of the WSA-like anomalies, which could be linked to long-term changes in the geomagnetic field. A series of simulations provides theoretical analysis of changes in the morphology of the WSA on time scales longer than several decades. Numerical analysis shows that from the time when the WSA was discovered (around 1960) till present, maximum of the WSA has migrated by approximately 7° in longitude towards the Pacific Ocean, showing clear westward drift, consistent with temporal evolution of the geomagnetic dipole component.

1. Introduction

Reversed ionization diurnal cycle is one of the distinctive features of the Earth's ionospheric *F* region, which can be briefly characterized by higher values of the peak electron concentration, N_mF2, observed in the post-sunset hours rather than around local noon. From the historical perspective, the first evidence of such behavior was found in the ionosphere of the Southern Hemisphere, close to the Antarctic Peninsula and surrounding seas. Bellchambers and Piggott (1958) and Penndorf (1965) commenced to call this specific behavior of the ionosphere, as the Weddell Sea Anomaly (WSA). Further studies, utilizing ground-based data and augmented by increasing number of satellite observations, showed that also in the Northern Hemisphere similar behavior of the ionosphere is registered. In the North, main area of interest concentrates on the Russian sector with Kamchatka, the Bering Sea, and the Sea of Okhotsk as focal points. In the literature, we can find also references to the Yakutsk Anomaly (Klimenko et al., 2015) or "the Siberian effect" (Eyfrig, 1963).

Initially, the occurrence of the anomaly was assigned to summertime conditions; thus, the phenomenon got broader name as the midlatitude nighttime summer anomaly (MNSA; Thampi et al., 2009, 2011). In consequence, numerous papers devoted to the problem of the WSA or MNSA focus on June and December solstices. Nevertheless, there are proofs that this type of ionospheric behavior remains still strong during both equinoxes. This is confirmed in climatological studies exploiting the total electron content (TEC) registrations from TOPEX/JASON-1 (Jee et al., 2009), in analysis of ionospheric plasma parameters (N_i, $T_{e,i}$, plasma drifts and fluxes) derived from the DMSP data set (Horvath & Lovell, 2010), or by Zhang et al. (2013) who examined the TIMED/GUVI data with interest in occurrence of midlatitude arcs. The term midlatitude arcs refer to enhancements in the electron density in nightside ionosphere, spatially spread across magnetic latitudes of 20° to 40°. Using in situ electron density registrations from the CNES mission DEMETER, Slominska et al. (2014) showed that above the altitude of 600 km, nighttime plasma density enhancements are an inherent ionospheric attribute, which exhibits modifications in strength and spatial extent due to seasonal variations of the ionosphere.

While the existence of the WSA-like phenomena is undoubted, mechanisms responsible for their appearance are being discussed. Most often, the occurrence of the WSA-like phenomena is attributed to the role of neutral winds (Lomidze et al., 2016; Richards et al., 2017, and references therein) and the morphology of the Earth's magnetic field (the role of declination and inclination) in the regions where anomalous behavior occurs (Horvath & Essex, 2003). While ionospheric ionization is mainly determined by solar radiation, transport of ionospheric plasma is tightly organized by the geometry of the magnetic field, which has an impact on thermospheric winds, generated electric fields, and system of ionospheric currents. The magnetic field structure, which organizes the ionospheric dynamics, is mentioned as a possible cause of some of the regional and global peculiarities in the ionospheric electron density. Horvath and Lovell (2009) stressed out the crucial role of the thermospheric neutral winds in the development of the WSA, by analyzing vertical plasma flows around the WSA site. Thanks to neutral winds, plasma accumulated at lower layers of the ionosphere can be elevated to upper altitudes (Jee et al., 2005; Rishbeth, 1998). Furthermore, confronting the role of neutral winds and vertical E × B drift, Cnossen and Richmond (2008) and Chen et al. (2011) showed that equatorward neutral winds dominate the plasma transport and are more fundamental for formation of the WSA in comparison with the ion drift.

In a quantitative analysis focused on the WSA, Richards et al. (2017, and references therein) reviews previous works and states that widely used interpretation that the WSA results from effects of the geomagnetic declination and inclination on the neutral wind is insufficient to cause longitudinal variation of the ionospheric electron concentration. Additionally, Richards et al. (2017) questions the concept that downward flux of plasmaspheric plasma is needed for the maintenance of nighttime density enhancements and points out that no additional sources are required. According to an interpretation adopted by the authors, the WSA develops from longitudinally organized distribution of the neutral winds and neutral densities. Furthermore, as noted by Richards et al. (2017), these longitudinal variations occur because the proximity to the auroral zone is not equal along latitudinal direction.

Nevertheless, the role of the Earth's magnetic field cannot be neglected. Direct relation linking components of neutral wind and the geomagnetic field parameters (inclination I and declination D) was discussed by Titheridge (1995) and Rishbeth (1998). To describe the effective neutral wind that trails the plasma along the magnetic field, we need to map both components, meridional (W_M) and zonal (W_Z), on magnetic field lines. This is obtained through the following formula (Jee et al., 2009):

$$V_{eff} = 0.5 \cdot \sin 2I \cdot (W_M \cos D \mp W_Z \sin D). \tag{1}$$

Depending on the hemisphere under consideration, "-" is used for the North, while "+" for the South. Diurnal variations of the neutral winds are observed: Predawn zonal winds are primarily westward, while post-sunset—mainly eastward. Also, meridional winds change their direction from daytime poleward to nighttime equatorward (Titheridge, 1995). The daytime poleward wind can be expected to transport the plasma to lower altitudes, where the recombination rate is larger, resulting in smaller plasma density in the dayside region. The equatorward nighttime wind acts in the opposite direction, elevating the plasma to higher altitudes and effectively retaining a relatively high density of plasma in the nightside region.

Previous studies of the WSA-like phenomena have been mainly focused on possibly accurate representation of factors contributing to the formation of the WSA (Horvath, 2006; Horvath & Essex, 2003; Horvath & Lovell, 2009, 2010; Ren et al., 2012; Richards et al., 2017), as well as has examined the impact of changing solar activity (Jee et al., 2009; Slominska et al., 2014). Chen et al. (2011) and Thampi et al. (2011) employed dipole field approximation for successful reconstruction of the WSA and MNSA; however, the contribution of secular variation in the Earth's magnetic field has been excluded from the discussion. It is worth to stress out that, on time scales longer than decades, changes in the magnetic field may introduce changes in V_{eff} and in consequence could affect the spatial distribution of the WSA-like phenomena.

As indicated by Rishbeth (1997), the secular variation leads to a gradual shift in the location of the magnetic poles and the equator, which prompts the migration of the electrojet as well as the deformation of equatorial ionospheric structures. As indicated by Rishbeth (1997), a gradual shift in the location of the magnetic poles and the equator is the strong evidence of the secular variation. In turn, it is expected to observe the migration of the electrojet and possible deformation of equatorial ionospheric structures. On scales of decades, developing variations in inclination and declination can be expected to cause a detectable effect on the structure of the F2-layer, especially in those areas where the influence of winds is remarkably strong due to the

morphology of the geomagnetic field. The Atlantic Ocean sector is considered as the region with the most evident signs of the geomagnetic secular variation (Finlay et al., 2016). Although not in the context of the WSA, Cnossen and Richmond (2008) confirmed findings obtained by Rishbeth (1997) and showed that in the time frame of 50 years, changes in the global distribution of the horizontal neutral wind are mainly in charge of fluctuations of the maximum height and peak concentration of the $F2$-layer. The authors emphasize a significant role of changes in the declination and the inclination as related to the $\sin(2I)$ term. In addition, taking into account that the Earth's magnetic field dipole moment has decreased by nearly 30% over the past two millenniums, in which almost 9% took place since 1840, modelers speculate (Olson & Amit, 2006) that the ongoing episode of the dipole-moment downtrend can be considered as an indication of a geomagnetic polarity reversal. During the reversal, which may last for several centuries, the dipole field maintains at a diminished level, while the residual field may form an unusual shape, leading to perplexing structures in the ionosphere (Rishbeth, 1997).

Performing extensive analysis of the global representation of TEC data from the TOPEX mission, Horvath and Essex (2003) brought back the interest in the phenomenon of the WSA in the current century. The authors pointed out that due to the vast extent of the anomaly, its central part lay west of the Faraday ionosonde station over the Bellingshausen Sea instead of the Weddell Sea, and proposed that the more appropriate name should be the Bellingshausen Sea Anomaly. Although the name of the phenomenon has not been changed, this finding suggested an inquiry about the possible migration of this large-scale ionospheric feature.

Focusing on temporal scales corresponding to decades and changes in the Earth's main magnetic field (so-called core field), the aim of this paper is to quantify how and to what extent steadily changing magnetic field impacts the formation of the WSA. On the other hand, we need to keep in mind that ionospheric changes purely related to the magnetic field secular variation are small, when compared with typical diurnal, seasonal, solar, and magnetic activity related variations of the ionosphere. A combination of measurements of in situ electron density, from two satellite missions, ongoing mission Swarm and past mission CHAMP, provides insight into overall dynamics of the spatial distribution of the WSA-like phenomena, registered by the two missions. Unfortunately, the time frame covered by these two missions is roughly 15 years, which in terms of analysis of secular variation represents a rather scanty data set and remains insufficient to derive conclusive results. Therefore, the discussion of the role of the Earth's magnetic field and interpretation of observed trends demands additional analysis employing a physics-based ionospheric model. The NCAR TIEGCM (Thermosphere-Ionosphere-Electrodynamics General Circulation Model) model is selected as a state-of-the-art model suitable for the study. TIEGCM is a time-dependent model, which solves the three-dimensional momentum, continuity, and energy conservation equations for neutral and ion species in three spatial dimensions (Richmond et al., 1992). The International Geomagnetic Reference Field (IGRF–12th generation, Thébault et al., 2015) model is implemented in TIEGCM to represent the Earth's main field and its secular variation. It is worth to mention that the latest set of Gauss coefficients, $g_{n,m}$, and $h_{n,m}$ provided by IGRF includes high-quality satellite measurements of the magnetic field collected by the Swarm mission.

Presented analysis is divided into four sections. Section 2 provides description of the proposed methodology based on the normalized density difference index I_{NDD}. Then in section 3 we introduce satellite data used for the study, as well as describe scenarios examined in the numerical modeling. Comparison between results from satellite data and numerical modeling is provided in section 4 and discussed in section 5. Section 6 sums up the analysis.

2. Methodology—Normalized Density Difference Index (I_{NDD})

For detection of the WSA-like phenomena, Slominska et al. (2014) examined the concept of the normalized density difference index (I_{NDD}), defined as follows:

$$I_{NDD}(\lambda, \theta) = \frac{N_e^{night}(\lambda, \theta) - N_e^{day}(\lambda, \theta)}{N_e^{night}(\lambda, \theta) + N_e^{day}(\lambda, \theta)} \tag{2}$$

Satellite registrations of in situ electron density acquired in a local time frame (LT) at the altitude determined by the satellite's orbit are binned into a grid. For each grid node with coordinates, λ as geographic longitude

and θ as geographic latitude, N_e^{night} and N_e^{day} denote median electron density measured on ascending and descending passes respectively, separated by 12 hr resulting from the satellite's quasi Sun-synchronous circular orbit. Based on observations of ionospheric plasma density registered by the CNES mission DEMETER, taken at two local times (22:15 - nighttime and 10:15 - daytime), the authors obtained global representation of regions in which ionosphere can be characterized by the reversed diurnal cycle. Under regular conditions (daytime N_e subtracted from nighttime N_e), the index is negative and represents typical ionospheric behavior. If I_{NDD} is greater than 0, it serves as an indicator of the reversed diurnal cycle and manifests possible nighttime enhancements. I_{NDD} is a sort of metric that quantifies a contrast between two ionospheric states separated by 12 hr, thus intervals when the I_{NDD} function peaks exhibit the highest contrast and preferable conditions for NPDEs (Nighttime Plasma Density Enhancements) detection. Since I_{NDD} is normalized, it has a well-defined range of changes from -1 to 1, making it a versatile parameter for comparison between independent data sources and models. Additionally, I_{NDD} operates on relative values instead of absolute measures, which minimize discrepancies originating from instrumental settings, but also provides the capability to track certain trends and large-scale patterns in ionospheric behavior. In contrast to climatological approach, the index eliminates small-scale plasma irregularities and perturbations, originating from quickly varying solar and geomagnetic disturbances, which are observed on time-scales corresponding to several hours or days. Therefore, by means of I_{NDD}, we aim to quantify whether long-term changes in the Earth's main magnetic field impact the spatial morphology of the WSA-like phenomena.

3. Data and Model

3.1. Satellite Data—Swarm and CHAMP

The analysis utilizes in situ satellite data of ionospheric electron density, measured by the Langmuir probe, onboard the Swarm constellation and the single-satellite mission CHAMP. The study exploits global maps of the I_{NDD} index, which are composed of monthly sets of data that are binned into a grid with spatial resolution $10° \times 1°$ in longitudinal and latitudinal direction, respectively. One-day running median is used to remove spikes and fluctuations in the electron density readings. Such procedure is performed over available Swarm dataset assigned with processing version v0501. In the same manner we process the CHAMP dataset.

Swarm mission allows to simultaneously measure plasma properties at two separate altitudes, with three satellites (Alpha [SwA], Bravo [SwB], and Charlie [SwC]) placed in two different polar orbits. Since completion of the orbit acquisition phase in April 2014, one satellite (SwB) is flying in a higher orbit with an inclination of 87.8° and an altitude decreasing from 520 km. The lower pair of satellites, SwA (trailing) and SwC (leading), was placed at an initial altitude of 473 km, an inclination of 87.4° and an ascending node difference of 1.4°. The CHAMP's orbit was lower than the pair from the Swarm constellation, with almost circular, near-polar orbit and slow precession. The launch of CHAMP took place in July 2000. CHAMP was placed into a near-polar orbit with an inclination of 87° and its initial altitude was 454 km. The mission lasted 10 years, and in its final stage the orbit was decayed to about 250 km. Unlike DEMETER, Swarm and CHAMP provide full local time coverage, but Swarm A/C, Swarm B, and CHAMP have different LT precession rates. For the two lower satellites, Swarm A/C, it takes 265 days to cover 24 hr of LT (for an individual node of the orbit), and for the higher-orbit spacecraft, Swarm B, it is 280 days. In case of CHAMP, 24 hr of LT are covered in approximately 260 days. Taking into account that the drift of LT is roughly 3 hr per month, for each monthly set, we extract LT of the middle day of the month as representing mean LT. The following pairs of monthly sets from CHAMP and Swarm A/C meet selection criteria of seasonal consistency and LTs suitable for observations of NPDEs (± 2 hr around local midnight/noon):

- March case: CHAMP 2009 (alt. 325 km), Swarm Alpha 2016 (alt. 455 km) (LT:2200-2300)
- December case: CHAMP 2004 (alt. 376 km), Swarm Alpha 2016 (alt. 451 km) (LT:2200)
- August case: CHAMP 2005 (alt. 363 km), Swarm Alpha 2018 (alt. 446 km) (LT: 0000-0100)

While DEMETER-based analysis was oriented on the single pair of local times, Swarm and CHAMP provide capability to expand this analysis. Additionally, extended LT coverage allows to provide reconstruction of the index in the universal time (UT) frame and proves that the WSA is the strongest example of the diurnal reversed cycle. Since this part of analysis is out of scope of the current paper, we only refer the reader to the animation provided in the supporting information.

3.2. TIEGCM Simulations

In situ measurements are supplemented with the synthetic index I_{NDD} derived from the TIEGCM model. For the present work, the TIEGCM 2.0 version is used with the double resolution. Such configuration provides a grid of 2.5° × 2.5° for latitude and longitude and 58 pressure levels in the vertical direction. The lower boundary of the model is at approximately 97 km, and the upper boundary ranges from 400 to 700 km depending on the solar activity and settings of solar flux. The option for lower boundary forcing is switched off to minimize the contribution from factors other than the magnetic field. The purpose of using TIEGCM is to reconstruct the I_{NDD} index at the altitude of a satellite; thus, we make an approximation between neighboring pressure levels in order to obtain the optimal agreement for the scale height.

Focusing on the role of the Earth's magnetic field and its impact on the formation of the WSA-like phenomena, we examine independent scenarios for the TIEGCM runs:

- Scenario #1: TIEGCM runs with a realistic magnetic field configuration determined by the IGRF model for a set of selected years.
- Scenario #2: Simplified magnetic field model reduced to dipole representation, with various configurations reflecting different eccentricity and tilt angle of the magnetic dipole.

Through all simulations, we used identical configuration of controlling parameters describing solar minimum and quiet geomagnetic conditions. The following parameters were used in the TIEGCM standalone runs: the solar flux ($F107 = 70$), the cross-tail potential ($CTPOTEN = 30$), and the hemispheric power ($POWER = 18$).

The model webpage (https://www.hao.ucar.edu/modeling/tgcm/tiegcm2.0/userguide/html/) provides more details on the physical meaning of the parameters used in the configuration and physics included in the model. Such configuration of model runs, minimizes the variability of the index originating from varying solar conditions, and allows to isolate effects related to changes in the main magnetic field. Before the index is computed, the TIEGCM output for the diagnostic field of the electron density N_e is converted to the LT frame. Using configurations defined above, we perform 5-day standalone runs, with the time-resolution of 10 min for March equinox, at two separate altitudes 360 km (corresponding to the CHAMP's orbit) and 460 km (as an equivalent of the Swarm's A/C orbit). Simulations are carried out for the years 1910, 1960, 2005, and 2015. The epoch 2005 and 2015 reflect the state of the core field for the CHAMP and Swarm mission, 1960 is selected as the representative of the magnetic field at the time when the WSA was discovered, while 1910 allows to expand analysis over the whole century.

4. Results

4.1. Recognition of NPDEs (Nighttime Plasma Density Enhancements)

Figure 1 presents results of monthly maps of I_{NDD} based on the satellite data from CHAMP (left column) and Swarm (right column) meeting the selection criteria defined in section 3.1. Global representation of the TIEGCM-based index is gathered in Figure 2. The numerical modeling results are provided at two altitude levels, 360 (left column in Figure 2) and 460 (right column in Figure 2) kilometers for midnight/noon conditions.

In order to facilitate recognition of the WSA and NPDEs and their evolution, we apply red-toned color coding to regions for which the I_{NDD} index obtains values greater than 0. Remaining areas, which show typical ionospheric behavior, are marked only with bluish isolines. The same method for data visualization is applied to model- and data-derived index. To simplify notation, throughout the text, we use one LT, but by referring to I_{NDD} at 00:00 LT, we keep in mind that the index is computed using the difference in electron densities between midnight and noon, and the same applies to every other hour.

In general, the spatial pattern of NPDEs derived with the CHAMP and Swarm data (Figure 1) as well as the TIEGCM model (see Figure 2) confirms findings from previous studies and indicates that in the Southern Hemisphere, region from the southern half of South America through Antarctic Peninsula and neighboring archipelagos and seas, the Weddell Sea and the Bellingshausen Sea and finally coasts of Antarctica, is the paramount sector for observations of reversed diurnal cycle. Corresponding effect in the Northern Hemisphere is localized in two spots, first one, in the central part of the Atlantic Ocean expanding towards the Southern Europe (for convenience we name it Northern Atlantic Enhancement—NAE) and the second one
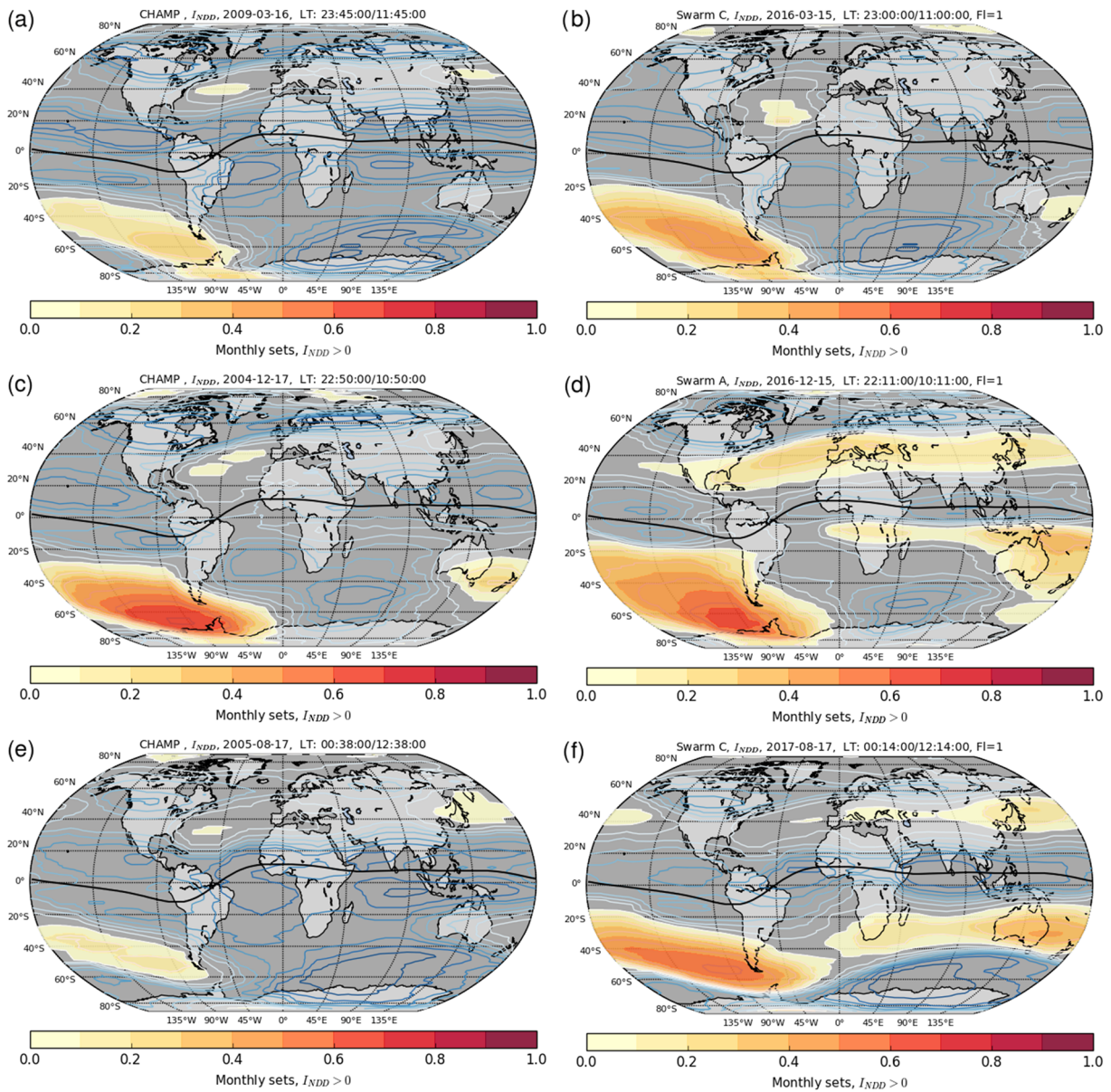
Figure 1. Global maps of I_{NDD} derived from in situ electron density measured onboard CHAMP and Swarm representing matching LT and seasons. Maps show regions where $I_{NDD} > 0$, indicating global pattern of WSA-like features. Left column presents data from CHAMP (a, c, e), right column Swarm A/C (b, d, f).

lays between the Kamchatka Peninsula, the Sea of Okhotsk and Japan (in brief Okhotsk Sea Enhancements - OSE). In general, model- and data-derived maps of the index show that northern hemispheric enhancements are weaker than the southern one and they tend to exhibit much stronger dependence on the altitude. According to numerical results, at 460-km only NAE emerges in 2005 and strengthens further on, but with no evidence of OSE. In contrast NAE intensifies and forms a structure slowly progressing from the continental Europe towards the east coast of Northern America. It is quite remarkable that the Swarm and CHAMP data show that OSE does not occur simultaneously at both satellites in all analyzed cases, giving evidence that in the North reversed ionospheric cycle is more dependent on altitude, LTs, and seasons.

One can notice that the TIEGCM-derived index has smaller amplitudes when compared with Swarm and CHAMP. As shown by Stolle et al. (2016), the IGRF model that is implemented in TIEGCM provides only representation of the main magnetic field (spherical harmonics up to degree 13) and does not contain contribution from external sources, lithospheric field, and the quiet-time magnetospheric field. In consequence,
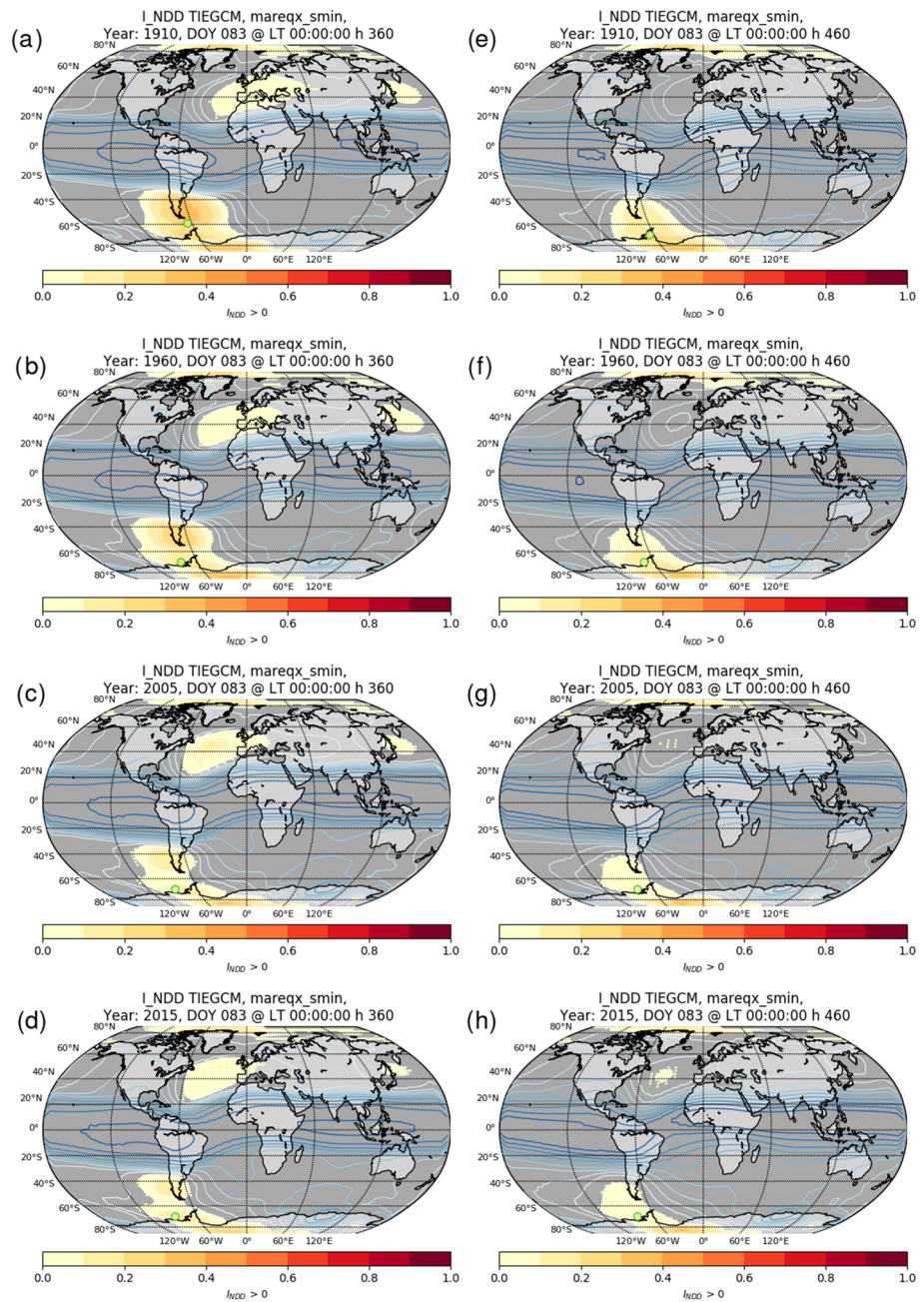
Figure 2. Synthetic index at the altitude of 360 km (left column) and 460 km (right column), for epochs: 1910, 1960, 2005, and 2015. Green point indicates maximum of the index in the region of the WSA.

model-derived index will not be able to fully reproduce such plasma density structures that can be associated with ionospheric currents occurring at low-latitude and midlatitude of the F-region. As shown by the authors, this can be improved when high-resolution models of the Earth's magnetic field are employed, such as the CHAOS-5 model.

Comparing two analyzed missions, we note more extended spatial coverage of NPDEs for Swarm than for CHAMP, which in particular is manifested by prolonged midlatitude (between 20° and 40° of latitude) bands of enhanced electron densities clearly marked in the hemisphere of local winter (in the North for December case [Figures 1c and 1d] and in the South for August case [Figures 1e and 1f] in Swarm data). Different orbital altitudes of these two missions possibly contribute to the observed patterns of I_{NDD}. Even though altitudinal differences are relatively small, for the March comparison (Figures 1a and 1b) the

Table 1
Maxima of I_{NDD} for Selection of Cases Presented in Figure 1

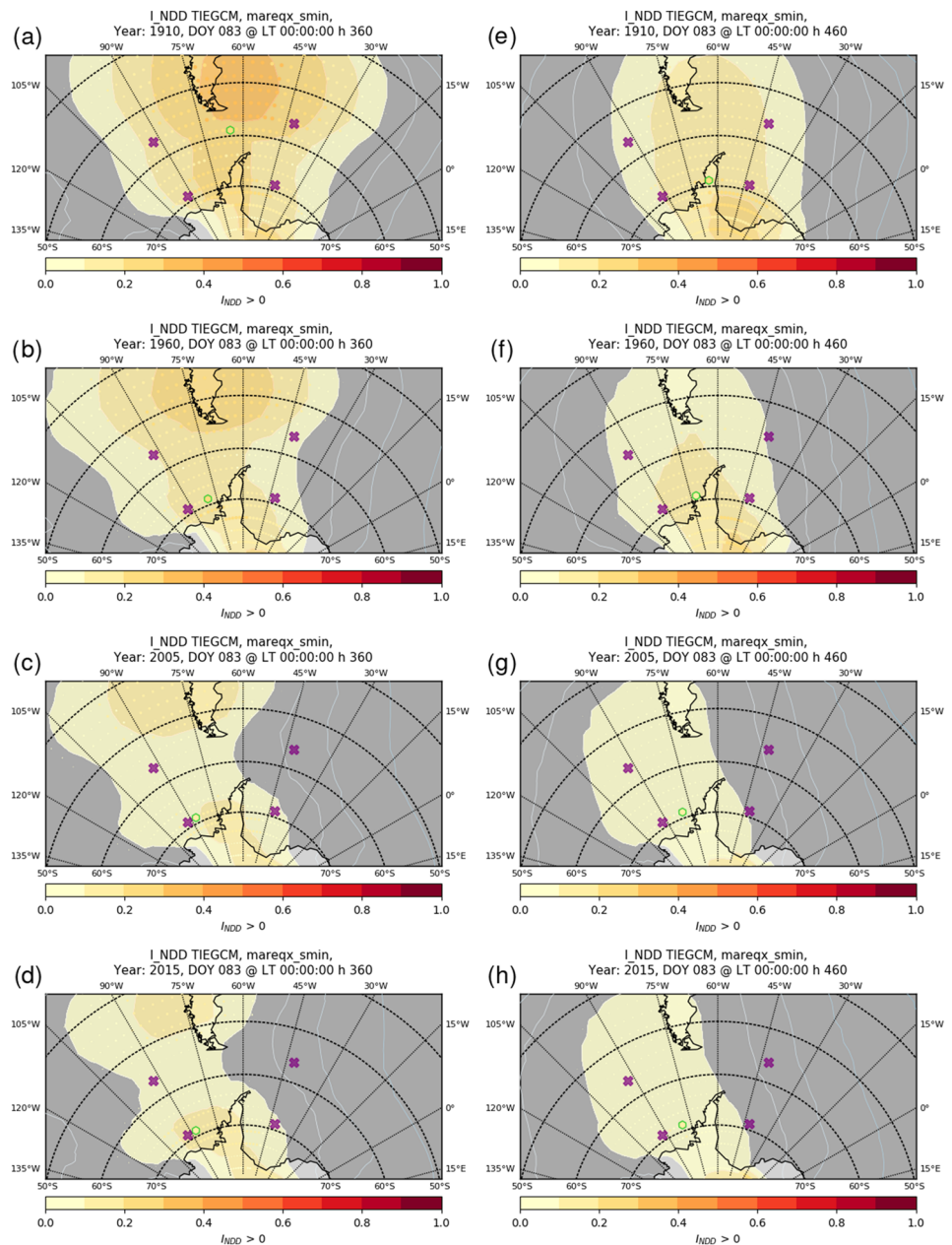|	Swarm		CHAMP	
Case	Max(I_{NDD})	Coordinates	Max(I_{NDD})	Coordinates
March	0.608	95.0° W/ 57.5° S	0.373	85.0° W/ 60.5° S
December	0.673	85.0° W/ 59.5° S	0.728	85.0° W/ 63.5° S
August	0.602	85.0° W/ 53.5° S	0.285	85.0° W/ 56.5° S

Figure 3. Same as Figure 2 with zoom on the region of the WSA. Violet markers indicate region of interest for deriving maxima of I_{NDD}.

Table 2
Maxima of I_{NDD} Derived From TIEGCM Simulations for Selected Years, at Two Altitude Levels (360 and 460 km) and LT Bins of 22:00/10:00 and 00:00/12:00

Year	Dipole moment	$Max.I_{NDD}$	Long./Lat.	$Max.I_{NDD}$	Long./Lat.
Alt: 360 km	$10^{22}Am^2$	LT 22:00/10:00		LT 00:00/12:00	
1910	8.27	0.470	65.0°W 58.75°S	0.299	65.0°W 58.75°S
1960	8.03	0.387	72.5°W 58.75°S	0.201	80.0°W 68.75°S
2005	7.77	0.283	87.5°W 58.75°S	0.178	87.5°W 68.75°S
2015	7.72	0.276	87.5°W 58.75°S	0.177	87.5°W 68.75°S
Alt: 460 km					
1910	8.27	0.443	65.0°W 58.75°S	0.209	65.0°W 68.75°S
1960	8.03	0.349	72.5°W 63.75°S	0.159	72.5°W 68.75°S
2005	7.77	0.233	87.5°W 58.75°S	0.107	80.0°W 68.75°S
2015	7.72	0.232	87.5°W 58.75°S	0.106	80.0°W 68.75°S

difference in altitude is greater than 100 km and in remaining instances is around 80 km, it is quite essential to note that CHAMP's orbit nearly cuts through the maximum of the *F*2 peak, while Swarm is slightly above. Zakharenkova et al. (2017) showed that the most-pronounced WSA effect, as a maximal electron density exceed over the noontime values, corresponds to altitudes above 400—500 km, which justifies stronger effects registered by Swarm. It is quite remarkable that despite seasonal correspondence, every single pair of monthly sets of measurements exhibits slight LT disparity, which may have a profound effect on the observed morphology of the index.

4.2. Tracking Local Maximum of the WSA

Long-term changes of the WSA are the scope of the study, and expected effect related to secular variation of the geomagnetic field would be in the form of a shift in position of the central part of the anomaly. Focusing only on satellite data and the region enclosed between 120°W and 45°W meridians and parallels of 50° S and 70° S, we look for the maximum of the index (see Table 1). In terms of absolute values, it looks like measurements from Swarm are considerably more stable, but also displaced with respect to the locations derived from CHAMP. Apparent differences between spatial distribution of the index derived from CHAMP and Swarm are present in all three examined cases, but as already mentioned in previous section, slight separation in LTs, as well as differences in the orbital settings between two missions, will have an impact not only on the observed morphology of the index but also its magnitude. Therefore, to quantify to what extent slowly changing main magnetic field impacts the WSA, we will concentrate only on the modeled results.

A closer look at the longitude sector between 0° and 60° W meridian in the numerical simulations (Figure 2, and zoom of the region in Figure 3) shows that throughout examined years, the eastern boundary of the WSA significantly shrinks and approaches 60° W meridian, while its western edge vaguely passes through 120° W. From the contour lines we see that in terms of the magnitude of the WSA, noticeable reduction is found.

In order to gauge the impact of geomagnetic secular variation, we search for a local maximum of the WSA in terms of the index, and we track its location. Analysis is performed in the southern sector of the Western Hemisphere (third quadrant of the map). Boundaries of interest are indicated by violet markers in Figure 3. To separate the WSA from the possible density enhancements occurring over the polar cap and to prevent from contamination resulting from auroral currents, we limit the region of interest with the poleward boundary set up at the latitude of 70°S. On the equatorward edge, we put the limit at the latitude of 55°S to avoid possible enhancements resulting from the close proximity of the equatorial ionization anomaly (EIA). Longitudinally, the region of interest spans from 90°W to 45°W. Local maxima derived in the extracted array are indicated with the green hexagonal markers in Figure 3. A summary of model-derived maxima is provided in Table 2. The selection of presented modeling results includes spatial smoothing for better visualization; however, it may hinder recognition of bin nodes containing maxima. Therefore, in the second part of the supplemental material, we provide the reader with the limited and extended view of the extracted array (without spatial smoothing) taken from the raw model output data. It has to be stressed out that estimated local maxima provide a quantitative measure of the migration; however, the a priori definition of the region of interest (ROI) has an implication on absolute values of displacement. Furthermore, due to relatively low
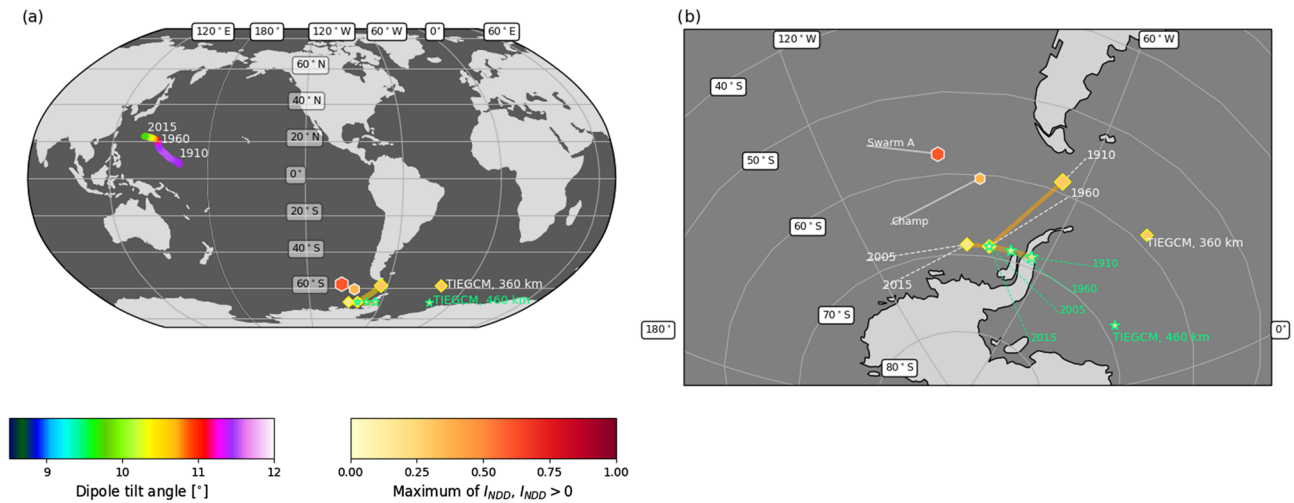
Figure 4. (a) Westward migration of the geomagnetic dipole and the Weddell Sea Anomaly. Rainbow color palette exhibits reduction of the geomagnetic dipole tilt angle, while the trace marks secular variation of the geomagnetic dipole position projected on the Earth's surface—trajectory derived for time frame 1900–2015. Warm toned yellow-red palette applies to maxima of the index I_{NDD} derived from the model (diamond and star markers) and data (hexagonal markers for March case). (b) A zoom on the region of the Antarctic Peninsula and the WSA, indicating derived maxima.

resolution of the model ($2.5° \times 2.5°$ size of the bin), the migration effect is captured when the maxima move from one node of the grid to another, while in reality, these changes may be much more subtle.

For the relatively short interval, spanning over the CHAMP and Swarm missions, between years 2005 and 2015, numerical simulations do not exhibit the drifting of the WSA, though a decrease of the amplitude of the index for examined LT bins and both altitudes is reported (see Table 2). However, on time scales longer than several decades (from 1910 to 2015), substantial westward migration of the WSA is observed in the numerical simulations. For a specified LT and altitude, maximum of the index relocates in the westward direction towards Pacific, with stronger effect at lower altitude (see Figure 4 for summary of locations for the 00:00 LT bin and both altitudes, based on Table 2). The altitudinal dependence suggests displacement of maxima for a given epoch, which implies that direct comparison of maxima derived from two examined missions may lead to misleading overestimation.

Analyzing the behavior of isolines outside the specified area, we see that general trend of migration should not be questioned, and as it is shown in the next section, it is in agreement with general behavior of the geomagnetic field, especially in the Western Hemisphere.

5. Discussion

5.1. Analysis of Simplified Configurations of Dipole-Field Approximations

Full set of Gauss coefficients of the IGRF-12 model allows to capture long-term changes in the main field, with contribution from dipole and non-dipole terms, and its impact on the spatial changes in the WSA morphology. For ionospheric applications, the dipole field dominates; therefore, for an explanation of modeled results, it is sufficient to focus mainly on secular variations of the dipole component. First eight Gauss coefficients define an eccentric dipole, displaced and tilted with respect to the Earth's rotation axis, while the first three Gauss coefficients represent contributions to a centered tilted dipole (Chapman & Bartels, 1962; Fraser-Smith, 1987). Conducting a simplified experiment using the TIEGCM model, we aim to show that changes in the tilt angle and eccentricity of the magnetic dipole have a profound influence on the spatial morphology of the WSA.

As a starting point, we take an eccentric dipole (see Figure 5a) with the tilt angle of $11°$ positioned about 400 km from the center of the Earth (specified by eight Gauss coefficients). In the next run, we reduce the eccentricity by placing the tilted geomagnetic dipole in the Earth's center (see Figure 5b). Results for spatial distribution of I_{NDD} for those two cases around midnight/noon (00:00LT) exhibit apparent signatures of the WSA manifested as patches of positive values of I_{NDD} located in the Southern Hemisphere and spanning over the longitude sector between $120°$ W to $45°$ W. Reduction of the offset between the geomagnetic dipole and
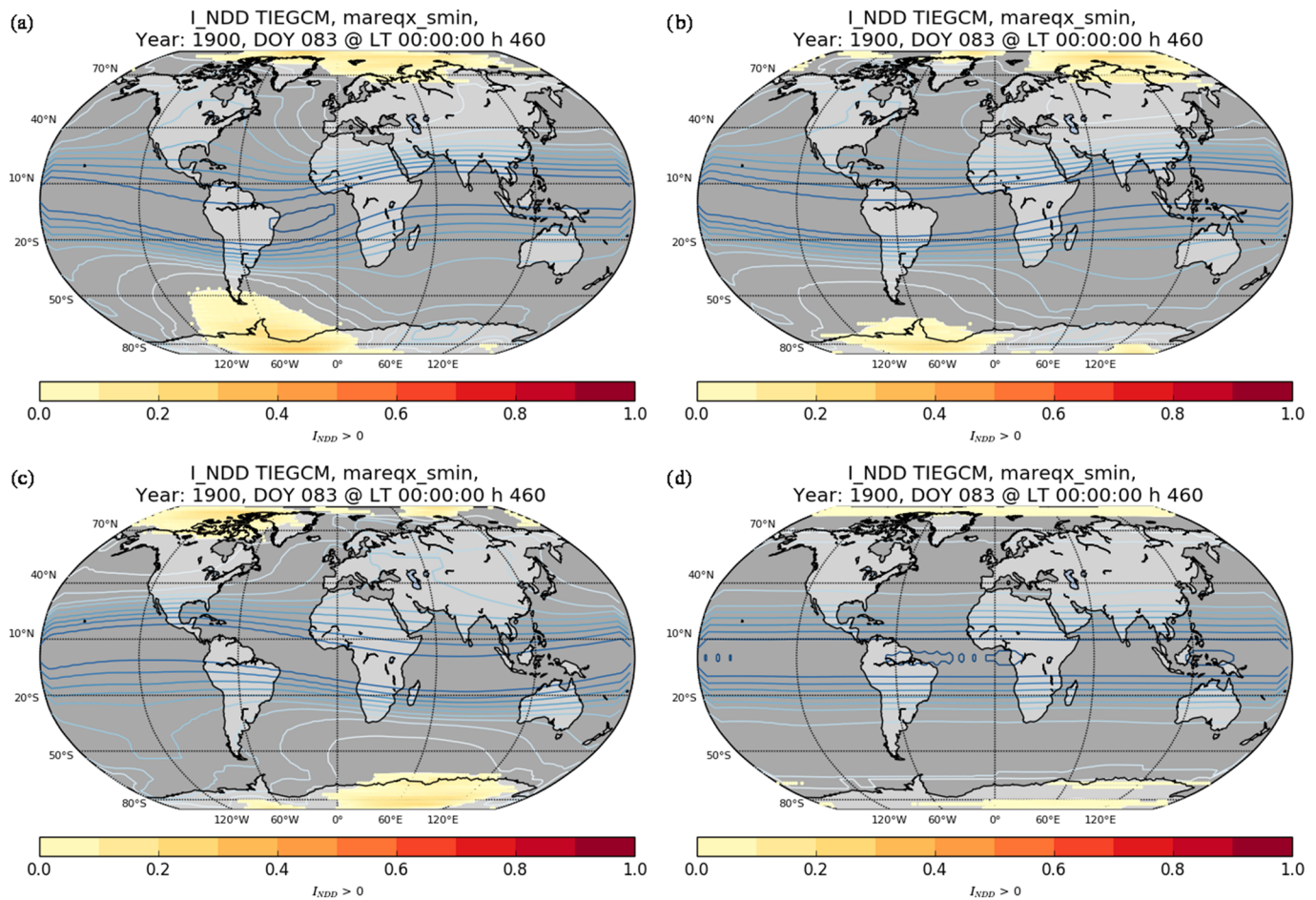
Figure 5. I_{NDD} derived in simplified experiments for LT conditions equal to midnight/noon (LT00:00)—(a) tilted eccentric dipole, (b) tilted dipole, (c) mirrored tilted dipole, and (d) axial dipole.

the Earth's rotation axis lessens interhemispheric asymmetry in the magnetic field and in consequence leads to more uniform distribution of the electron density and the index. In such configuration, not only the area of the WSA is reduced but also northern hemispheric enhancements spanning over parts of the Eastern Europe (longitude sectors between 15° E and 45° E) vanish. The third run formulates speculative and exaggerated scenario to the previous case where the orientation of the geomagnetic tilted dipole is opposite with respect to the Earth's rotation axis. In such configuration, the WSA occurs in the Indian Ocean sector, while all other typical ionospheric features (dip equator, location of auroral ovals) exhibit typical mirrored reflection (see Figure 5c). In the final run, the tilt angle is set to 0 (axial dipole), which in consequence eliminates the WSA. Under such conditions, there is full symmetry between both hemispheres, and ionospheric structure is homogenous, practically symmetric across latitudes regarding the straightened dip equator (see Figure 5d). Ionization controlled by the solar zenith angle plays the major role, and in consequence, for near midnight conditions, we observe nearly longitudinally uniform distribution of negative values of I_{NDD}.

5.2. Westward Drift of the WSA

Bearing in mind the results of numerical experiments with simplified configurations from the preceding subsection, we take a closer look at the secular variation of the dipole component. Following formalism provided by Chapman and Bartels (1962) and updated by Fraser-Smith (1987) and Koochak and Fraser-Smith (2017), we compute the properties of the eccentric dipole, using the first eight Gauss coefficients. This allows us to reconstruct time series of the dipole tilt angle and compute the total displacement of the geomagnetic dipole from the center of the Earth.

Figure 4 shows the variation of the eccentric dipole position projected on the Earth's surface with respect to the equatorial plane. Applied color scale reflects the tilt angle. Results indicate a systematic reduction in the

tilt angle (from purple through reds towards green), with a rapid decrease which commenced around 1960. As shown by Amit and Olson (2008), the declining trend in the dipole tilt is first and foremost caused by changes in the equatorial component of the dipole moment. Currently decreasing tendency is observed for the equatorial and the axial component of the dipole moment, as well as the dipole tilt angle and the total intensity of the dipole moment. From Figure 4, we note that geomagnetic dipole steadily moves away from the equatorial plane and the Earth's center. Koochak and Fraser-Smith (2017) estimated a rate of migration at the level of 2.5 km per year, showing that at the current stage the relocation reaches 9% of the Earth's radius with nearly 580 km, while in 1980, it was around 488.6 km.

As shown in previous studies (Cnossen & Richmond, 2012; Siscoe & Christopher, 1975) and in simplified simulations presented in the current paper, the dipole tilt angle determines the geographical location of the geomagnetic pole and polar cap boundaries. The strength of the Joule heating, the structure of ionospheric convection patterns, and the spatial distribution of energetic particle precipitation are also organized by the dipole tilt angle. Variations in the Joule heating with tilt angle lead to changes in temperature and neutral winds and in consequence impact thermospheric composition. Modulations in the O/N_2 ratio change electron-ion recombination rates and lead to variations in the $F2$ electron density.

On the one hand, decreasing dipole tilt angle implies that the WSA's expansion towards the low latitude regions as well as its longitudinal variation may be minimized. On the other hand, the second principal secular variation of the dipole field, the westward drift, also affects morphology of the WSA. The dipole part is moving away from the Earth's center, with the movement accompanied by steady northward migration above the equatorial plane (see Figure 4, position of the geomagnetic dipole projected on the Earth's surface). Stronger eccentricity of the dipole component may lead to much more pronounced asymmetries between two hemispheres, excessive longitudinal variations, and strengthening of the WSA across the Pacific Ocean, westward from the Antarctic Peninsula. Such behavior is consistent with the modeled pattern of the WSA migration, but also similar tendency seems to emerge from a visual comparison of selected Swarm and CHAMP maps of the index. The proximity of the Weddell Sea Anomaly to the region of the South Atlantic Anomaly (SAA) suggests that the impact of geomagnetic secular variation may be visible in the same way as it is observed for the SAA. Significant evidence of the westward migration of the Earth's magnetic field is documented by secular variation of the SAA. Numerous studies (Jones et al., 2017; Pavón-Carrasco & Santis, 2016, and references therein) confirm that the total intensity of the magnetic field is changing. Strong expansion of the South Atlantic Anomaly towards continental regions of South America is recorded, with the minimum of the magnetic field intensity located in Brazil.

Although the WSA as the most prominent example of NPDEs is the focal point of the study, to sum up conducted work, we provide quantitative evaluation of long-term changes in simulated I_{NDD} on a global scale. The measure is expressed through percentage difference δI_{NDD} between selected epochs (2015 and 1910) with respect to the maximum value of the I_{NDD} index for a given LT bin and altitude in 2015. Estimation is made for a given altitude and local times (see Figure 6). In most regions, at midlatitude and high-latitude, modifications, both positive and negative are rather small and do not go beyond 15% (in Figure 6 areas marked with pale grey and pale salmon tones). However, four separate spots emerge as areas of intensified changes of I_{NDD}, including the region of the Weddell Sea. Comparison for examined time intervals, indicates that the strength of the anomaly diminishes steadily in the Weddell Sea region (red tones denote negative tendency) and builds up on the western side of the Antarctic Peninsula in the Bellingshausen Sea and across the Pacific Ocean, giving evidence of general westward drift of this particular ionospheric feature. The most intense variations in spatial morphology of I_{NDD} are expected to occur in the longitude sector of the Atlantic Ocean, on both sides of the geomagnetic dip equator. It suggests that for examined March equinox conditions, nighttime enhancements in the Atlantic region are stronger than those in the Siberian region. Obtained global pattern of changes in the morphology of I_{NDD} is in agreement with results from comprehensive studies by Cnossen & Richmond, Cnossen & Richmond (2008, 2013), who concluded that in comparison to other parts of the world, in the Atlantic region, defined as the area between 40°S and 40°N and 100° W and 50°E, secular variation of the Earth's magnetic field is in charge of most ionospheric trends. Observed significant variations of magnetic field inclination dominate the overall behavior, having an impact on the vertical component of plasma transport. In terms of changes in the Sq (solar quite) current, Cnossen and Richmond (2013) recognized significant regional dependency, associated with already mentioned relocation of the dip equator and the westward drift of the geomagnetic field. It is worth to stress out that modulations of the field intensity were not considered as fundamental for derived patterns of ionospheric parameters.
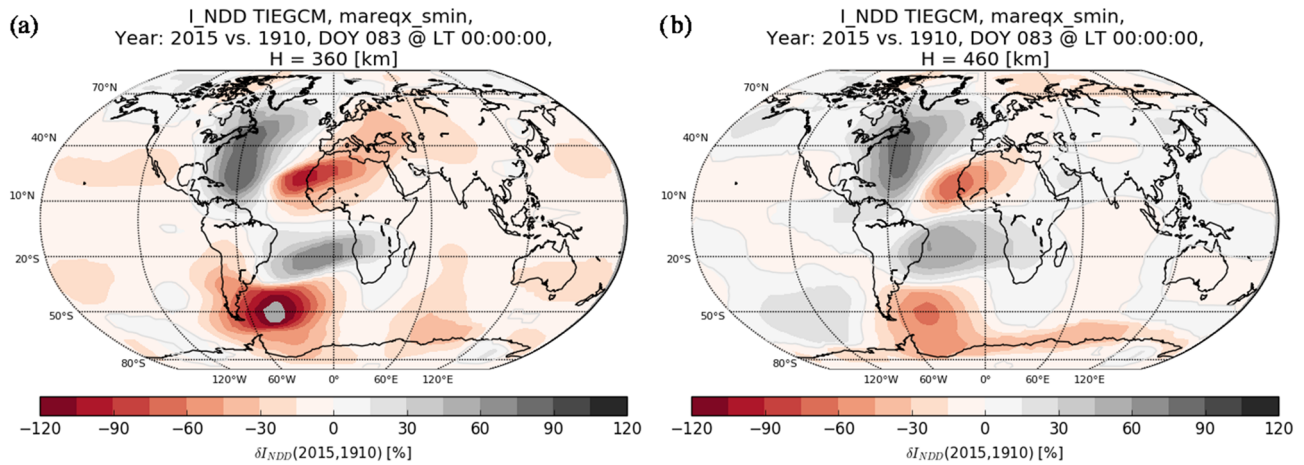
Figure 6. Percentage difference δI_{NDD} of the synthetic index, based on difference between epochs (2015 and 1910). (a) Altitude of 360 km, (b) altitude of 460 km.

Although the study concentrates on the time scales equal to decades, we should note that the longitudinal sector of the Atlantic Ocean is also the region of the most intense short-term variations of the magnetic field. As shown by Balasis et al. (2015), in terms of short-term magnetic field disturbances, Swarm and CHAMP provide complimentary results. In a statistical studies oriented on satellite observations of ultralow frequency (ULF) waves, Balasis et al. (2015) provide characteristics of Pc pulsations in the topside ionosphere and show that thanks to finer spatial resolution of Swarm, initial results from CHAMP were improved. In the same work, the authors recognize the region of the Atlantic Ocean, as the area that exhibits highest occurrence rates of Pc1 and Pc3 pulsations, while in the current analysis we show that this longitudinal sector should be of interest, due to growing intensification of NPDEs in its northern part.

The strength of the Earth's main magnetic field changes over time. Long-term changes in the magnetic field reveal decreasing tendency of the intensity of the main dipole component (see the second column in Table 2), which has an effect on ionospheric conductivity (expressed through the Pedersen and Hall conductivities). As shown by Takeda (1996) when the field strength decreases, altitudes of Pedersen conductivity maxima shift upward, and height-integrated Pedersen and Hall conductivities are enhanced. Although conductivity is proportional to the concentration of the electron and ions, and inversely proportional to the magnetic field intensity, we find a gradual decrease in the amplitude of I_{NDD}. Table 2 summarizes performed simulations, grouping maxima of the index with locations for analyzed LT bins and altitudes. Knowing that all simulations are performed at a fixed level of solar activity and identical seasons, we can exclude these factors as a plausible cause of the observed trend. Since I_{NDD} operates on the relative difference between dayside and nightside ionosphere, the relation between the index and changes in magnetic field intensity is not straightforward, and more complex dependencies take place. This finding awaits further verification with in situ measurements; however, at the current stage of the Swarm mission we still lack sufficient representation of data.

6. Conclusions

In this article, we have made an attempt to investigate the relationship between long-term changes in the magnetic field and spatial morphology of the WSA. To our knowledge, no dedicated study of this aspect has been conducted. The presented analysis joins the advanced ionospheric model and in situ measurements derived from two satellite missions. Utilizing the I_{NDD} index, we have tracked the location of the maximum of the anomaly. Modeled results indicate that

- from the time when the WSA was discovered (around 1960) to the present time, the central part of the anomaly migrated by approximately 7° in longitude westward;
- drift in latitude is less obvious and depends on considered local time, as well as the altitude.

Confrontation of results from numerical modeling with measurements from two satellite missions, Swarm and CHAMP, confirms a slight shift in the WSA location towards western parts of the Pacific Ocean; however,

obtained absolute values of displacement suggest to be overestimated. One of main reasons for such result is the fact that despite similar goals of two examined missions, altitudes of their orbits are not at equal, and this has a major implication on the data-derived maxima. Obtained result proves that is essential to acquire possibly long representation of high-resolution measurements from one satellite mission (at least 10 or 15 years of data) in order to conduct this type of analysis for more trustworthy outcome, with additional interest on thorough investigation of a complete solar cycle. Unfortunately, we also have to bear in mind that satellite missions have its limitations, when it comes to the mission duration. The Swarm mission is officially only planned until 2021 at the moment, with possible extension until 2023.

Through a series of simplified numerical experiments we aimed to investigate how varying configurations of the geomagnetic field affect the WSA phenomenon and prove that the structure and configuration of the geomagnetic field are crucial for the spatial pattern of the WSA. The WSA region was the focal point of the study, but it is worth to mention that the central sector of the Atlantic Ocean is characterized by more intense changes in the magnetic field configuration. A glimpse of results from simulations and limited selection of observations indicates that the occurrence of NAE exhibits prominent variations and tendency to strengthening over the century, which suggests that deeper analysis of this region should be considered in further studies. In particular, the constellation of Swarm satellites should provide more detailed image of changes in the spatial morphology of NPDEs on a global scale, simultaneously at two altitudinal levels.

References

Amit, H., & Olson, P. (2008). Geomagnetic dipole tilt changes induced by core flow. *Physics of the Earth and Planetary Interiors*, *166*(3-4), 226–238. https://doi.org/10.1016/j.pepi.2008.01.007

Balasis, G., Papadimitriou, C., Daglis, I. A., & Pilipenko, V. (2015). ULF wave power features in the topside ionosphere revealed by swarm observations. *Geophysical Research Letters*, *42*, 6922–6930. https://doi.org/10.1002/2015gl065424

Bellchambers, W. H., & Piggott, W. R. (1958). Ionospheric measurements made at Halley Bay. *Nature*, *182*(4649), 1596–1597. https://doi.org/10.1038/1821596a0

Chapman, S., & Bartels, J. (1962). *Geomagnetism*. Clarendon Press.

Chen, C. H., Huba, J. D., Saito, A., Lin, C. H., & Liu, J. Y. (2011). Theoretical study of the ionospheric Weddell Sea Anomaly using SAMI2. *Journal of Geophysical Research*, *116*, A04305. https://doi.org/10.1029/2010ja015573

Cnossen, I., & Richmond, A. D. (2008). Modelling the effects of changes in the Earth's magnetic field from 1957 to 1997 on the ionospheric hmF2 and foF2 parameters. *Journal of Atmospheric and Solar-Terrestrial Physics*, *70*, 1512–1524. https://doi.org/10.1016/j.jastp.2008.05.003

Cnossen, I., & Richmond, A. D. (2012). How changes in the tilt angle of the geomagnetic dipole affect the coupled magnetosphere-ionosphere-thermosphere system. *Journal of Geophysical Research: Space Physics*, *117*, A10317. https://doi.org/10.1029/2012JA018056

Cnossen, I., & Richmond, A. D. (2013). Changes in the earth's magnetic field over the past century: Effects on the ionosphere-thermosphere system and solar quiet (Sq) magnetic variation. *Journal of Geophysical Research: Space Physics*, *118*, 849–858. https://doi.org/10.1029/2012JA018447

Eyfrig, R. W. (1963). The effect of the magnetic declination on the F_2 layer. *Journal of Geophysical Research*, *68*(9), 2529–2530. https://doi.org/10.1029/JZ068i009p02529

Finlay, C. C., Olsen, N., Kotsiaros, S., Gillet, N., & Tøffner-Clausen, L. (2016). Recent geomagnetic secular variation from swarm and ground observatories as estimated in the CHAOS-6 geomagnetic field model. *Earth, Planets and Space*, *68*(1), 18. https://doi.org/10.1186/s40623-016-0486-1

Fraser-Smith, A. C. (1987). Centered and eccentric geomagnetic dipoles and their poles, 1600–1985. *Reviews of Geophysics*, *25*(1), 1. https://doi.org/10.1029/rg025i001p00001

Horvath, I. (2006). A total electron content space weather study of the nighttime Weddell Sea Anomaly of 1996/1997 southern summer with TOPEX/Poseidon radar altimetry. *Journal of Geophysical Research*, *111*, A12317. https://doi.org/10.1029/2006ja011679

Horvath, I., & Essex, E. A. (2003). The Weddell Sea Anomaly observed with the TOPEX satellite data. *Journal of Atmospheric and Solar-Terrestrial Physics*, *65*(6), 693–706. https://doi.org/10.1016/s1364-6826(03)00083-x

Horvath, I., & Lovell, B. C. (2009). Investigating the relationships among the South Atlantic Magnetic Anomaly, southern nighttime mid-latitude trough, and nighttime Weddell Sea Anomaly during southern summer. *Journal of Geophysical Research*, *114*, A02306. https://doi.org/10.1029/2008JA013719

Horvath, I., & Lovell, B. C. (2010). Investigating the southern daytime midlatitude trough's relation with the daytime Weddell Sea Anomaly during equinoxes. *Journal of Geophysical Research*, *115*, A01302. https://doi.org/10.1029/2008JA014002

Jee, G., Burns, A. G., Kim, Y.-H., & Wang, W. (2009). Seasonal and solar activity variations of the Weddell Sea Anomaly observed in the TOPEX total electron content measurements. *Journal of Geophysical Research*, *114*, A04307. https://doi.org/10.1029/2008JA013801

Jee, G., Schunk, R. W., & Scherliess, L. (2005). On the sensitivity of total electron content (TEC) to upper atmospheric/ionospheric parameters. *Journal of Atmospheric and Solar-Terrestrial Physics*, *67*(11), 1040–1052. https://doi.org/10.1016/j.jastp.2005.04.001

Jones, A. D., Kanekal, S. G., Baker, D. N., Klecker, B., Looper, M. D., Mazur, J. E., & Schiller, Q. (2017). SAMPEX observations of the South Atlantic anomaly secular drift during solar cycles 22-24. *Space Weather*, *15*, 44–52. https://doi.org/10.1002/2016sw001525

Klimenko, M. V., Klimenko, V. V., Karpachev, A. T., Ratovsky, K. G., & Stepanov, A. E. (2015). Spatial features of Weddell Sea and Yakutsk anomalies in foF2 diurnal variations during high solar activity periods: Interkosmos-19 satellite and ground-based ionosonde observations, IRI reproduction and GSM TIP model simulation. *Advances in Space Research*, *55*(8), 2020–2032. https://doi.org/10.1016/j.asr.2014.12.032

Koochak, Z., & Fraser-Smith, A. C. (2017). An update on the centered and eccentric geomagnetic dipoles and their poles for the years 1980–2015. *Earth and Space Science*, *4*(10), 626–636. https://doi.org/10.1002/2017ea000280

Lomidze, L., Scherliess, L., & Schunk, R. W. (2016). Modeling and analysis of ionospheric evening anomalies with a physics-based data assimilation model. *Journal of Atmospheric and Solar-Terrestrial Physics*, *140*, 65–78. https://doi.org/10.1016/j.jastp.2016.02.009

Olson, P., & Amit, H. (2006). Changes in Earth's dipole. *Naturwissenschaften*, *93*(11), 519–542. https://doi.org/10.1007/s00114-006-0138-6

Pavón-Carrasco, F. J., & Santis, A. D. (2016). The South Atlantic Anomaly: The key for a possible geomagnetic reversal. *Frontiers in Earth Science*, *4*, 40. https://doi.org/10.3389/feart.2016.00040

Penndorf, R. (1965). The average ionospheric conditions over the Antarctic, *Geomagnetism and Aeronomy: Studies in the Ionosphere, Geomagnetism and Atmospheric Radio Noise* (pp. 1–45). American Geophysical Union. https://doi.org/10.1029/AR004p0001

Ren, Z., Wan, W., Liu, L., Le, H., & He, M. (2012). Simulated midlatitude summer nighttime anomaly in realistic geomagnetic fields. *Journal of Geophysical Research*, *117*, A03323. https://doi.org/10.1029/2011JA017010

Richards, P. G., Meier, R. R., Chen, S.-P., Drob, D. P., & Dandenault, P. (2017). Investigation of the causes of the longitudinal variation of the electron density in the Weddell Sea Anomaly. *Journal of Geophysical Research: Space Physics*, *122*, 6562–6583. https://doi.org/10.1002/2016ja023565

Richmond, A. D., Ridley, E. C., & Roble, R. G. (1992). A thermosphere/ionosphere general circulation model with coupled electrodynamics. *Geophysical Research Letters*, *19*(6), 601–604. https://doi.org/10.1029/92GL00401

Rishbeth, H. (1997). Long-term changes in the ionosphere. *Advances in Space Research*, *20*(11), 2149–2155. https://doi.org/10.1016/s0273-1177(97)00607-8

Rishbeth, H. (1998). How the thermospheric circulation affects the ionospheric F2-layer. *Journal of Atmospheric and Solar-Terrestrial Physics*, *60*(14), 1385–1402. https://doi.org/10.1016/s1364-6826(98)00062-5

Siscoe, G. L., & Christopher, L. (1975). Effects of geomagnetic dipole variations on the auroral zone locations. *Journal of Geomagnetism and Geoelectricity*, *27*(6), 485–489. https://doi.org/10.5636/jgg.27.485

Slominska, E., Blecki, J., Lebreton, J.-P., Parrot, M., & Slominski, J. (2014). Seasonal trends of nighttime plasma density enhancements in the topside ionosphere. *Journal of Geophysical Research: Space Physics*, *119*, 6902–6912. https://doi.org/10.1002/2014JA020181

Stolle, C., Michaelis, I., & Rauberg, J. (2016). The role of high-resolution geomagnetic field models for investigating ionospheric currents at low earth orbit satellites. *Earth, Planets and Space*, *68*, 110. https://doi.org/10.1186/s40623-016-0494-1

Takeda, M. (1996). Effects of the strength of the geomagnetic main field strength on the dynamo action in the ionosphere. *Journal of Geophysical Research*, *101*(A4), 7875–7880. https://doi.org/10.1029/95ja03807

Thébault, E., Finlay, C. C., Beggan, C. D., Alken, P., Aubert, J., Barrois, O., et al. (2015). International geomagnetic reference field: The 12th generation. *Earth, Planets and Space*, *67*(1), 79. https://doi.org/10.1186/s40623-015-0228-9

Thampi, S. V., Balan, N., Lin, C., Liu, H., & Yamamoto, M. (2011). Mid-latitude summer nighttime anomaly (MSNA)—Observations and model simulations. *Annales Geophysicae*, *29*(1), 157–165. https://doi.org/10.5194/angeo-29-157-2011

Thampi, S. V., Lin, C., Liu, H., & Yamamoto, M. (2009). First tomographic observations of the midlatitude summer nighttime anomaly over Japan. *Journal of Geophysical Research*, *114*, A10318. https://doi.org/10.1029/2009ja014439

Titheridge, J. E. (1995). Winds in the ionosphere—A review. *Journal of Atmospheric and Terrestrial Physics*, *57*(14), 1681–1714. https://doi.org/10.1016/0021-9169(95)00091-f

Zakharenkova, I., Cherniak, I., & Shagimuratov, I. (2017). Observations of the Weddell Sea Anomaly in the ground-based and space-borne TEC measurements. *Journal of Atmospheric and Solar-Terrestrial Physics*, *161*, 105–117. https://doi.org/10.1016/j.jastp.2017.06.014

Zhang, Y., Paxton, L. J., & Kil, H. (2013). Nightside midlatitude ionospheric arcs: TIMED/GUVI observations. *Journal of Geophysical Research: Space Physics*, *118*, 3584–3591. https://doi.org/10.1002/jgra.50327

Experimental Evidence of a Link Between Lightning and Magnetic Field Fluctuations in the Upper Ionosphere Observed by Swarm

M. Strumik[1], J. Slominski[1], E. Slominska[2], J. Mlynarczyk[3], J. Blecki[1], R. Haagmans[4], A. Kulak[3], M. Popek[5], K. Martynski[3], R. Wronowski[1]

[1]Space Research Centre PAS (CBK PAN), Bartycka 18a, 00-716 Warsaw, Poland
[2]OBSEE, Warsaw, Poland
[3]AGH University of Science and Technology, Faculty of Computer Science, Electronics and Telecommunications, Department of Electronics, Krakw, Poland
[4]ESA ESTEC, Noordwijk, Netherlands
[5]Department of Space Physics, Institute of Atmospheric Physics, Czech. Acad. Sci., Prague, Czechia

Key Points:

- Lightning can generate ULF fluctuations leaking into the upper ionosphere
- Observations show that the fluctuation amplitude is proportional to the lightning charge moment
- The ULF fluctuations generated by lightning can be detected by low-Earth orbit satellites, e.g., the Swarm constellation

Corresponding author: M. Strumik, maro@cbk.waw.pl

Abstract

We present results of analysis of lightning observations and satellite measurements of ionospheric magnetic field fluctuations in the ultra low frequency (ULF) range. The fluctuations are measured by Swarm satellites, while the lightning observations are provided by the Geostationary Lightning Mapper (GLM) and the World ELF Radiolocation Array (WERA). We identify spatio-temporal relationships that demonstrate a leakage of electromagnetic fluctuations caused by lightning into the upper ionosphere. Causal association between the two phenomena is evidenced by investigating relations between lightning and fluctuation properties. The presented results suggest that lightning generate ULF fluctuations in the ionosphere that can be detected by satellites, if the lightning-satellite geographic distance is less than $\sim 5°$. Typical properties of the fluctuations caused by lightning are described in the paper. To our knowledge this is the first direct experimental confirmation of a link between lightning and magnetic field fluctuations in the upper ionosphere in the ULF range.

Plain Language Summary

It has been a matter of interest, if electromagnetic fluctuations caused by lightning can propagate from the lower atmosphere higher into the ionosphere, which is an ionized and electrically conducting medium. This process requires conversion of the electromagnetic perturbation propagating in the neutral atmosphere into an ionospheric plasma wave, which for ultra low frequencies (ULF) can attenuate strongly the wave amplitude. The attenuation is considered to be rather significant, thus one could argue that it is virtually not possible to observe the ionospheric magnetic field perturbations caused by lightning using currently available satellite magnetometers.

There are many remote observations of lightning and direct satellite measurements of ionospheric magnetic field fluctuations, that can be analyzed searching for a possible link between the two phenomena. Using Swarm satellite measurements and two types of lightning observations, we provide an evidence that lightning generate electromagnetic perturbations that propagate into the upper ionosphere and can be measured with magnetometers onboard low-Earth orbit satellites, e.g., by the Swarm constellation. We reveal links between lightning and ionospheric wave properties, that suggest a real causality relationship between the two phenomena. To our knowledge this is the first direct experimental confirmation of such a relation in the ULF range.

1 Introduction

Lightning around the Earth are known to generate electromagnetic fluctuations in a broad range of frequencies that propagate in the lower atmosphere. The highest power content is typically at frequencies of the order of $\sim$kHz [very low frequency (VLF) range], but some discharges maintain a continuing current and luminous activity on longer time scales corresponding to the ULF frequencies of the order of $\sim$Hz (Shindo & Uman, 1989; Ross et al., 2008). Although lightning events are known to modify the conductivity of the lower ionosphere that can lead to generation of transient luminous events (TLEs; see, e.g., Inan et al. (2010); Pasko et al. (2012)), the question of possible leakage of ULF fluctuations from the lower atmosphere into the upper ionosphere has not been fully understood yet. Observations of the Schuman resonance (Simes et al., 2011) and excitation of the ionospheric Alfvén resonator (IAR, see Simões et al. (2012)) in the equatorial ionosphere suggest possible connection between lightning and ionospheric ULF dynamics. For the ELF/VLF range, Błecki et al. (2009) showed that waves seen in measurements of the electric field by the DEMETER satellite can be linked to thunderstorm and sprite (a form of TLE) observations. Additionally, the idea of a leakage of lightning-generated electromagnetic fluctuations into the ionosphere has been investigated in a number of theoretical studies (see, e.g., Surkov et al. (2006); Plyasov et al. (2012); Mazur et al. (2018)).

However, a direct observational evidence confirming the leakage in the ULF range has been missing.

This Letter presents results of joint analysis of lightning observations and satellite measurements of the magnetic field aimed at pinpointing ionospheric ULF wave dynamics associated with lightning. Magnetic field measurements are provided by the VFM instrument onboard the Swarm A and C satellites (Tøffner-Clausen et al., 2016). The Swarm constellation consists of three satellites on low-Earth orbit dedicated to measurements of the geomagnetic field. All three satellites operate on a circular near-polar orbit of high orbital inclination. Satellites A and C are moving synchronously at the altitude ∼440 km separated by ∼1.5 deg. Satellite B operates independently at a higher altitude of ∼530 km. Among other instrumentation onboard, all satellites are equipped with the same type of vector magnetometer VFM that provides high-accuracy and high-resolution measurements of the local magnetic field vector. Observations of the luminous activity associated with lightning are based on data provided by the GLM instrument onboard the GOES-16/17 satellites (Goodman et al., 2013; GOES-R Algorithm Working Group and GOES-R Series Program, 2018). The satellite observations are supplemented with the ground-based ELF measurements of lightning-related activity acquired by the WERA radiolocator (see Młynarczyk et al. (2017) for details). Schematic view of the Swarm-GLM-WERA observations/measurements is shown in Fig. 1.

2 Data Selection Procedure

The vector magnetometers onboard the Swarm satellites provide a sequence of measurements of the magnetic field vector $\mathbf{B}_i$ (i indexes subsequent measurements in time) at a sampling frequency of 50 Hz. In the first step, the magnetic field strength B_i is computed, which is then detrended using a fourth-order polynomial fitting, applied over 128 samples. This step is applied to remove the Earth's main magnetic field component. Then we search for time intervals with good matching to a predefined signature (the derivative of a Gaussian function, time scales between 0.1 and 0.5 s) in the detrended magnetic field strength. Arguments supporting the choice of the specific signature are discussed in Text S1 in the supporting information. In the next step, the signature-matching fluctuations are examined, if they are preceded by lightning localized closely (i.e. within the geographic distance $\Delta \lesssim 5°$) to the satellite positions projected on the Earth surface. In this step, for a preliminary selection, we utilize a data source described at the World Wide Lightning Location Network (WWLLN) webpage as "Google Earth overlay for 1 hour of global data". Another selection criterion is used, where a given magnetic fluctuation must be observed by both Swarm A and C, since for these cases a cross-correlation analysis is possible as discussed further in this Letter. The next step involves visual inspection of the magnetic fluctuations to identify those that clearly stand out from the surrounding noise and are of isolated-impulse type (i.e., have small number of up-down swings), since such impulse-like fluctuations can be unambiguously attributed to particular lightning. In this Letter we focus on cases for which the GLM data is available, which provides detailed information on the time, location, optical energy and spatial extent of flashes associated with lightning.

Using the procedure described above we have identified 11 cases located in low-latitude regions between 35° S and 35° N (see Fig. 3), detected mainly in the northern hemisphere. Since we use the GLM data, we naturally focus here on the North and South America and adjacent oceanic regions.

3 Spatio-temporal Correlations Between Magnetic Fluctuations and Lightning

In Fig. 2 we show a juxtaposition of the selected cases, where a magnetic field fluctuation measured by Swarm A and C satellites is caused by lightning as evidenced fur-
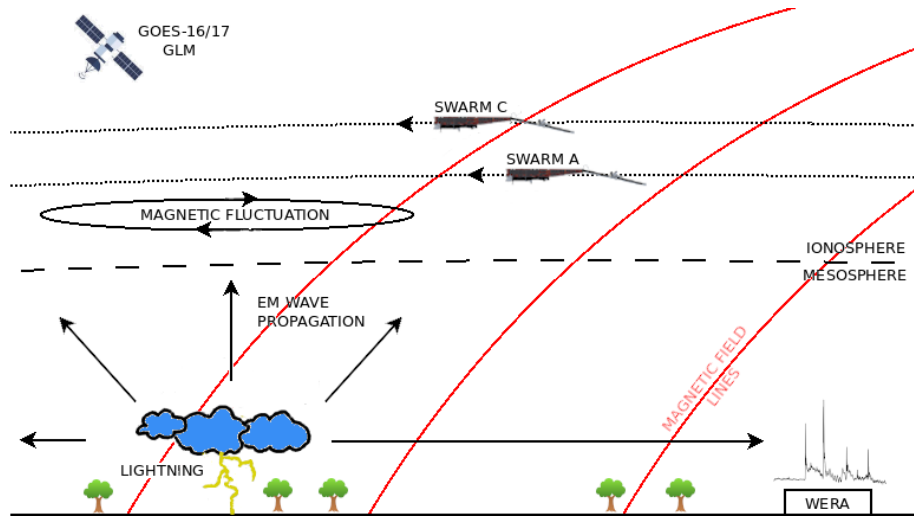
Figure 1. Schematic view of joint Swarm-GLM-WERA observations/measurements of lightning effects. A lightning discharge generates electromagnetic field that propagates in the Earth-ionosphere waveguide and can be detected by the ground-based WERA radiolocator. The fluctuation propagates also towards the ionosphere-mesosphere boundary, where it can be converted into a plasma wave. At higher altitudes, a magnetic field perturbation associated with the ionospheric wave can be measured by the Swarm satellites moving in their orbits around the Earth. The magnetic field perturbation in the ionosphere is shown schematically in the form of a circular loop (i.e., a toroidal magnetic fluctuation), since the dominant component is expected to be azimuthal in lightning-axis-centered cylindrical geometry as suggested by Mazur et al. (2018). Geostationary GOES-16/17 satellites are equipped with the GLM instrument that provides independent observations of top-of-clouds optical emission associated with lightning flashes. Earth's main magnetic field lines (low-latitudes) are shown schematically in red. Note that the view is not to scale, typical altitude for lightning is 2-3 km (-CG type) or 10-15 km (+CG type), the mesosphere-ionosphere boundary is at ∼90 km, the Swarm satellite orbit is at ∼440 km, while the GOES-16/17 geostationary orbit is located at ∼35700 km. The cases considered in the Letter were observed at local nighttime. Although during daytime the lower ionospheric boundary can be as low as ∼60 km, the nighttime boundary altitude of ∼90 km is considered here as a relevant estimate.
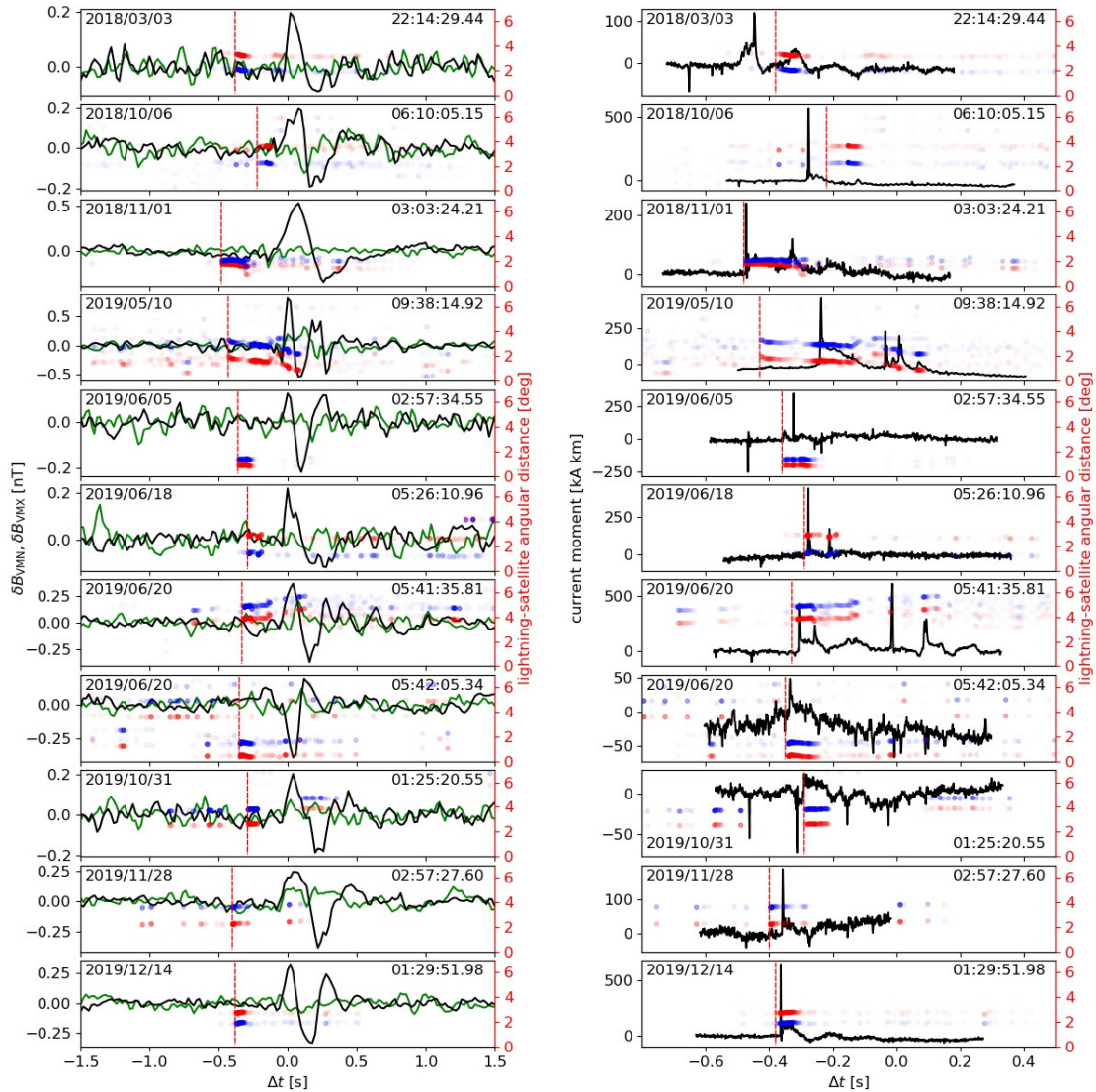
Figure 2. A juxtaposition of Swarm-GLM (left column) and GLM-WERA observations (right column). Data from the GLM satellites are presented in a form of time-distance-energy plots (see text). Long intense red or blue stripes indicate the occurrence of lightning flashes close to Swarm A and C , respectively. A vertical red dashed-line bar shows the beginning of the most intense long-lasting event in the GLM observations. In the left column, the GLM data are overplotted onto the Swarm A VFM measurements of magnetic field fluctuations. The maximum variance component δB_{VMX} is shown in black and the minimum variance δB_{VMN} – in green. In the right column, the same GLM observations are overplotted onto the WERA measurements. The inferred current moment of lightning is shown in black. Note that the time axis in the left column covers a range [-1.5,1.5] s, while for the right column it is [-0.8,0.5] s. Dates (YYYY/MM/DD) and UTC times of the observations can be identified by tags in every panel.

ther in the Letter. Originally, the Swarm satellite measurements of $\delta\mathbf{B}_i$ are provided in the NEC (north-east-center) frame, that we transform to so-called minimum/maximum variance (MV) frame to extract the maximum amplitude of a given fluctuation regardless of the lightning-satellite mutual orientation and wave polarization. A vector base for the MV frame is obtained by eigendecomposition of a covariance matrix computed for the time series $\delta\mathbf{B}_i$. An eigenvector corresponding to the smallest eigenvalue defines the minimum variance direction, while the largest-eigenvalue eigenvector corresponds to the maximum variance direction (see Sonnerup and Cahill (1967); Sonnerup and Scheible (1998) for details).

The left column in Fig. 2 shows that for the investigated cases the maximum-variance component δB_{VMX} (black line) has much higher variance than the minimum-variance component δB_{VMN} (green line), which is an indicator of the plane-wave character of perturbations under scrutiny. In all panels, the time is measured from the leading slope of δB_{VMX} fluctuation for Swarm A. In the panels on the left in Fig. 2, GLM data are overplotted onto the Swarm measurements, in a form of time-distance-energy plots. In this convention, red and blue markers contain information on groups of luminous events seen by the GLM. The timing of the groups relative to the Swarm measurements can be investigated looking at the horizontal axis. Red vertical axis on the right shows the distance of the GLM groups from Swarm A (red markers) and C (blue markers). The opacity of the markers indicates the energy of the GLM groups. Therefore, long intense red or blue stripes indicate the occurrence of lightning flashes lasting $\sim 0.1-0.3$ s and localized up to $\sim 5°$ from Swarm A and C. The beginning of the flashes is marked with a vertical red dashed-line bar, which allows us to determine the time lags between the most intense optical emission events seen by the GLM and the magnetic field fluctuations measured by Swarm satellites. The time lags are typically 0.2-0.5 s, while the peak-to-peak amplitude of δB_{VMX} is 0.3-1.3 nT. The GOES-16/17 satellites operate at the geostationary orbit, thus the detection of lightning flashes by the GLM instrument is significantly delayed (at least ~ 0.12 s) relative to the real emission time. However, the times of events occurence in the GLM Level-2 data sets are compensated for this effect, thus the lightning-satellite time lags estimated above should be considered as corrected for the photon time-of-flight delay.

The right column in Fig. 2 shows a juxtaposition of the WERA measurements overplotted onto the GLM time-distance-energy plots. Majority of the presented cases show a typical scenario, where the beginning of the optical emission seen by the GLM (red dashed bar) is shortly followed by a peak in the WERA current-moment waveform, which is associated with a return stroke. This peak-related disturbance is often accompanied by a continuing current on a longer time scale. There are three exceptions to this rule, namely the cases 2018/03/03, 2018/10/06, 2019/10/31, where peaks in the current moment have occurred before optical emissions. This indicates a different relation between charging processes, lightning leaders and optical effects. Generally, the presented WERA measurements confirm that the optical emissions seen by the GLM are indeed associated with lightning discharges.

In Fig. 3 we present maps showing spatial relations between the location of satellites and lightning for the 11 cases identified by the selection procedure described above. We can see that flashes generating the magnetic field fluctuations seen by the Swarm satellites are usually spatially extended. In general, there is a difference in the distance of a flash (black cross) to the satellites A (magenta) and C (orange). This feature is used in our inter-satellite cross-correlation analysis presented below. The dominant component of the ULF fluctuations generated by lightning is expected to be azimuthal in lightning-axis-centered cylindrical geometry as suggested by Mazur et al. (2018). Such toroidal geometry can be easily understood if a magnetic fluctuation generated by a discharge is considered as similar to the magnetic field around a straight wire. If modeling assumptions proposed by Mazur et al. (2018) are satisfied in nature, the dominant magnetic fluc-
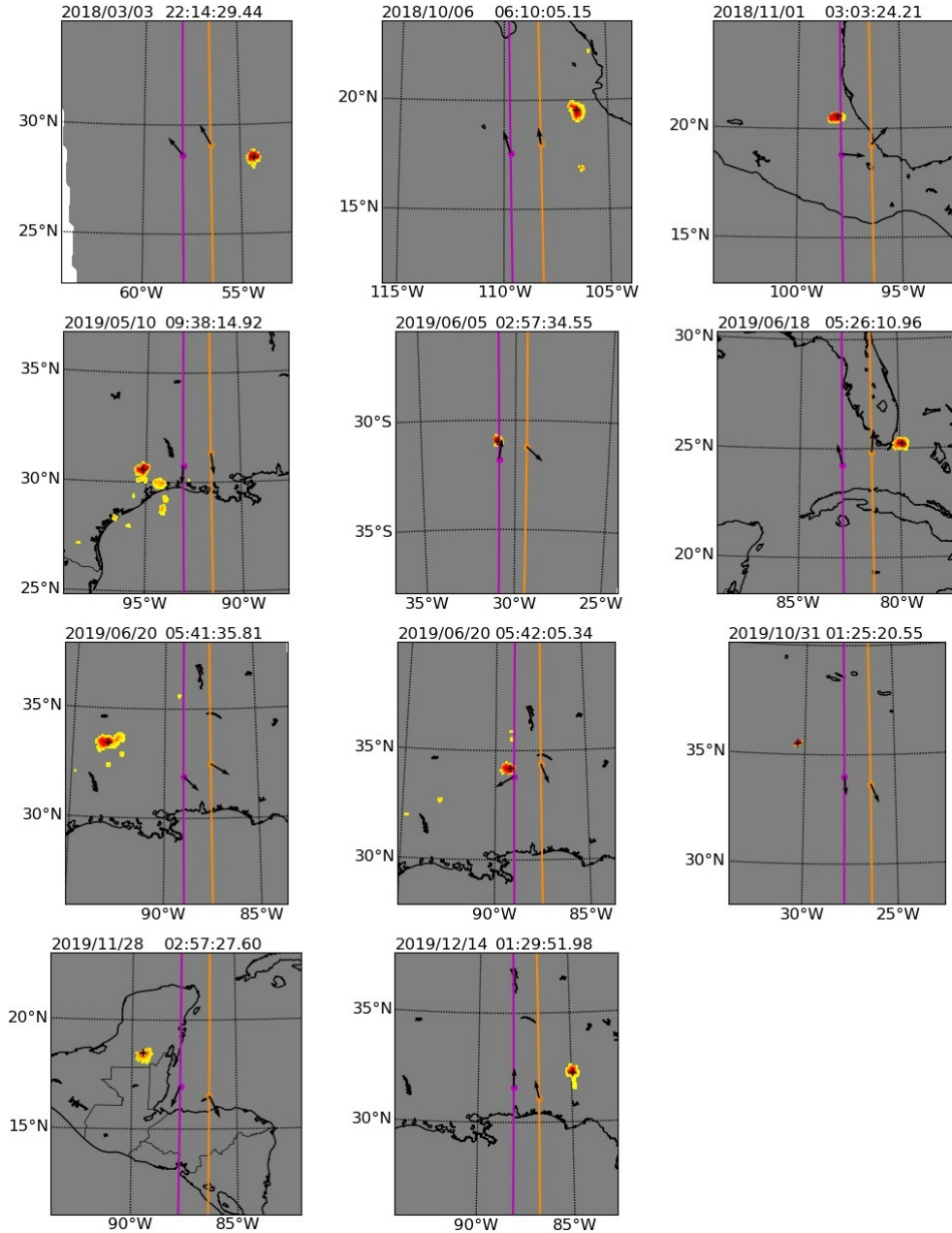
Figure 3. Maps showing geographic locations of lightning with respect to Swarm A and C. The yellow color shows locations of all optical emission events seen by the GLM instrument independent of their brightness. Red color on top of the yellow spots shows the brightness of the emission events, as the opacity for the red color is proportional to the intensity of events. Locations of the intensity-weighted centers of flashes are shown by black crosses on top of red spots. The GLM events are accumulated over 0.1 s following the red dashed-line bars shown in Fig. 2. Magenta line shows Swarm A orbit, where the position of the satellite at the time of detection of fluctuation is marked with a circle. In a similar manner, the Swarm C orbit is shown in orange. Black arrows show the maximum variance direction (projected on the Earth surface) computed from fluctuations measured by Swarm A and C. Tags above the maps identify the cases under investigation.

tuation vector should be aligned toroidally around flashes. In our analysis, the dominant fluctuation component corresponds to the maximum variance direction, that is shown by black arrows in Fig. 3, separately for satellites A and C. For majority of the presented cases, the arrows are indeed oriented approximately perpendicularly to a line between the satellite and flash locations, which is consistent with the toroidal alignment. There are however some cases, e.g., 2019/06/05 or 2019/06/20(05:41:35.81), where deviations from this behavior are observed – detailed understanding of these cases presumably requires considerations involving strongly non-vertical lightning axis.

For the fluctuation vector aligned toroidally, its vector direction can be translated into the direction of a current generating a given fluctuation. Clockwise direction for majority of analyzed cases suggests +CG discharge, where a positive charge is flowing from clouds to the ground. This result is also confirmed by the WERA measurements. Definitely counter-clockwise direction is observed only for the case 2018/11/01, while 2019/06/05 and 2019/06/20(05:41:35.81) are difficult to interpret in this regard.

Gray background in maps presented in Fig. 3 is introduced purposely to indicate the local nighttime. All lightning-fluctuation-correlation cases that we describe occurred on the nightside of the Earth, even though we do not use any explicit selection criterion based on the local time. Possibly the nighttime conditions foster the leakage of lower-atmosphere electromagnetic fluctuations into the ionosphere as suggested by Simes et al. (2011) in the context of satellite detection of the Schumann resonance. It is also possible, that since we require the GLM-data availability, we implicitly favor nighttime cases, due to superior flash detection efficiency by the GLM instrument during the night.

4 Relations Between Lightning and Fluctuation Properties

So far we have been discussing spatio-temporal correlations between lightning and ionospheric magnetic field fluctuations. In this section we present results suggesting a real causality relationship. Fig. 4(a) shows a dependence of the amplitude of the fluc-
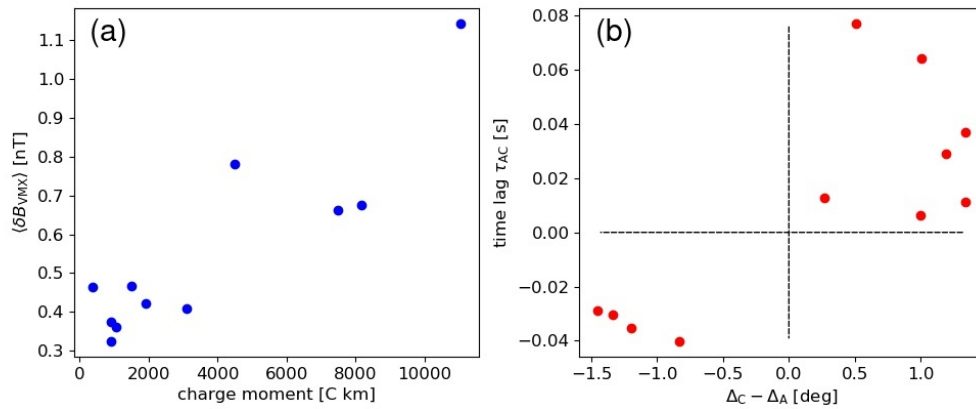

Figure 4. Relations between lightning features and fluctuations measured by the Swarm satellites. Panel (a) shows a relationship between the estimated charge moment of lightning (based on WERA measurements) and the amplitude of fluctuations $\langle \delta B_{\mathrm{VMX}} \rangle$ (averaged over two satellites). Panel (b) shows a dependence of a time delay τ_{AC} between measurements of the same fluctuation by two Swarm satellites (A and C) and a difference $\Delta_{\mathrm{C}} - \Delta_{\mathrm{A}}$ in the distance of the satellites to the lightning location as inferred from the GLM observations.

tuations on the estimated charge moment of associated lightning. The fluctuations δB_{VMX}

shown in Fig. 2 have bipolar character, but in general up-down disturbance is not symmetric relative to zero. For this reason, in Fig. 4(a), we use a peak-to-peak amplitude averaged over measurements of Swarm A and C, i.e., $\langle \delta B_{\mathrm{VMX}} \rangle = (1/2) \sum_{i=[A,C]} (\delta B_{\mathrm{VMX,i}}^{\mathrm{MAX}} - \delta B_{\mathrm{VMX},i}^{\mathrm{MIN}})$. The charge moment is computed by time-domain-integration of the WERA-measurement-based current moment shown in Fig. 2. Although some scatter is observed, Fig. 4(a) suggests a clear relationship between the amplitude of the fluctuations and the lightning charge moment. The current and charge moments were calculated using the method presented by Młynarczyk et al. (2015) (see also Młynarczyk et al. (2017)) and the ELF propagation model described by Kułak and Młynarczyk (2011).

The cases we discuss fall into a well-constrained range of the angular distance $\Delta \lesssim 5°$ and the time lag 0.2-0.5 s between lightning and fluctuations. Since the coupling mechanism between the two phenomena requires propagation of a wave disturbance, one could expect a relation between the lightning-satellite distance and the time lag between the lightning occurrence and detection of associated fluctuation by a satellite. Among many investigated distance-lag relations, we have found the following one as clearly supported by the Swarm-GLM observations. Since the selected fluctuations are observed by two satellites, it is possible to compute a lag-dependent cross-correlation coefficient between measurements of the same fluctuation by Swarm A and C. Global maximum of the cross-correlation function may serve as an indicator of an averaged inter-satellite time lag τ_{AC}. More detailed discussion of computations of the cross-correlation function and the time lag τ_{AC} can be found in Text S2 in the supporting information. We adopt a convention here, where $\tau_{\mathrm{AC}} < 0$ indicates the detection of a fluctuation by Swarm C earlier than by A, while $\tau_{\mathrm{AC}} > 0$ corresponds to Swarm A precedence over C. If Swarm A is located closer to a lightning event than Swarm C, i.e., $\Delta_{\mathrm{C}} - \Delta_{\mathrm{A}} > 0$, we expect a fluctuation to be seen by Swarm A first, so $\tau_{\mathrm{AC}} > 0$. Consequently, for $\Delta_{\mathrm{C}} - \Delta_{\mathrm{A}} < 0$ we expect $\tau_{\mathrm{AC}} < 0$. In Fig. 4(b) we present a dependence of τ_{AC} on $\Delta_{\mathrm{C}} - \Delta_{\mathrm{A}}$ estimated for the cases under investigation, which indeed shows the expected arrangement. In our understanding, this type of distance-lag relationship is possible to detect because it is based on the observation of the very same fluctuation propagating under similar conditions (in terms of background plasma density, concentration of ion species and the magnetic field). We expect that in general, refraction effects and variations of the ionospheric plasma state are presumably so significant, that detection of a simpler distance-lag relationship is very difficult, if possible at all.

Details regarding the 11 cases that have been selected for analysis can be found in Text S4 and Tabs. S1 and S2 in the supporting information.

5 Conclusions

We presented results suggesting direct relations between lightning observations and satellite measurements of ionospheric magnetic field fluctuations in the ULF range. In our study we identified 11 cases that are likely to demonstrate a leakage of electromagnetic fluctuations caused by lightning into the upper ionosphere in low-latitude regions. Spatio-temporal relations supported by links between properties of the lightning and ionospheric waves, suggest a real causality relationship between the two phenomena under investigation.

All analyzed cases were observed during nighttime and in low-latitude regions. Typical time delay between the lightning occurrence and the satellite detection is 0.2-0.5 s, which is generally consistent with theoretical predictions by Mazur et al. (2018). Such time delays indicate that we observe here rather a direct propagation of lightning-generated disturbance than effects of excitation of the IAR resonance, which would require a longer time scale. The waves under scrutiny propagate in the atmosphere presumably approximately at the speed of light, which implies very small time lags. After conversion to a plasma wave at the mesosphere-ionosphere boundary, a typical length scale for the prop-

agation in the ionosphere until detection by Swarm satellites can be estimated as $\sim$400 km. Combining this length scale with the time lags discussed above, we find a range of propagation speeds $\sim$800$-$2000 km/s, which well corresponds to order-of-magnitude estimations of the Alfven speed in the ionosphere. Our estimate of the propagation speed should be understood as the average over all layers of the ionosphere until detection by Swarm satellites.

Typical magnitude of the observed lightning-related magnetic perturbations is 0.3-1.3 nT (peak-to-peak), which is significantly smaller than $\sim$4 nT resulting from modeling by Mazur et al. (2018). It is not currently clear, what is the reason for the difference. In our understanding, the only significant difference between the model and the real cases in our analysis, is related to the orientation of the discharge axis relative to the vertical direction and the background magnetic field. Mazur et al. (2018) assume that the lightning axis is co-aligned with the purely vertical magnetic field, which is a good approximation rather for polar regions, where nonetheless lightning appear much less frequently than at lower latitudes. At low-latitudes, where the analyzed cases occurred, the Earth's main magnetic field lines are inclined with respect to the vertical direction and so also relative to the expected typical cloud-ground discharge axis. Another difference is related to the character of magnetic field disturbance. In Fig. 8 by Mazur et al. (2018), the fluctuation is strongly asymmetric relative to the equilibrium, while our Fig. 2 suggest rather bipolar character of the observed disturbances. Therefore, it is possible that non-vertical magnetic field introduces an additional complexity, that affects the propagation or wave conversion processes. The presence of the continuing current and relatively long time scale of luminous activity for the cases under scrutiny suggest possible connections to TLEs, which however requires further analysis that is beyond the scope of this Letter.

It is worth noting, that Fig. 4(b) shows the relation between the fluctuation amplitude and charge moment, where the vertical-axis intercept is $\langle \delta B_{\text{VMX}} \rangle \approx 0.3$ nT for the null current moment, if a linear fit would be used. One can obviously expect that the null charge moment should correspond to the null fluctuation amplitude. Therefore, the observed relationship suggests a strongly nonlinear character of the fluctuation-amplitude dependence on the charge moment.

One should note that the Swarm VFM instrument is dedicated to measure the Earth's main magnetic field, which is much stronger (typically $\sim$25$-$65 μT) than the amplitude of the fluctuations under investigation. Therefore only strong lightnings located closely to Swarm are able to generate spikes exceeding the VFM-instrument noise level ($\sim$0.1 nT). We anticipate that a dedicated instrument for the fluctuations could provide a significantly larger statistical sample for analysis. Our results show that the vector magnetometer technique provides additional essential information in comparison with measurements of the magnetic field strength only. As we show above, the Swarm VFM measurements make it possible to determine the maximum variance direction, characterizing wave properties of fluctuations in a more comprehensive way. Results presented in this Letter help to understand better how different lower-atmospheric phenomena are related to the dynamics of the ionosphere. In particular, the results shed light on mechanisms of conversion of lower-atmospheric electromagnetic waves into ionospheric plasma waves, which can be useful for various diagnostic purposes.

vironmental Information for providing access to GOES-16/17 GLM data. Swarm data are available through the access webpage
https://earth.esa.int/web/guest/swarm/data-access.
The glmtools package was used for analysis of GLM data, the software is available at https://github.com/deeplycloudy/glmtools.

References

Błecki, J., Parrot, M., & Wronowski, R. (2009). ELF and VLF signatures of sprites registered onboard the low altitude satellite DEMETER. *Annales Geophysicae*, *27*(6), 2599-2605. doi: 10.5194/angeo-27-2599-2009

GOES-R Algorithm Working Group and GOES-R Series Program. (2018). *NOAA GOES-R Series Geostationary Lightning Mapper (GLM) Level 2 Lightning Detection: Events, Groups, and Flashes.* https://data.nodc.noaa.gov/cgi-bin/iso?id=gov.noaa.ncdc:C01527. NOAA National Centers for Environmental Information. (Accessed: 2020-09-06) doi: 10.7289/V5KH0KK6

Goodman, S. J., Blakeslee, R. J., Koshak, W. J., Mach, D., Bailey, J., Buechler, D., ... Stano, G. (2013). The GOES-R Geostationary Lightning Mapper (GLM). *Atmospheric Research*, *125*, 34-49. doi: 10.1016/j.atmosres.2013.01.006

Inan, U. S., Cummer, S. A., & Marshall, R. A. (2010). A survey of ELF and VLF research on lightning-ionosphere interactions and causative discharges. *Journal of Geophysical Research (Space Physics)*, *115*(A3), A00E36. doi: 10.1029/2009JA014775

Kułak, A., & Młynarczyk, J. (2011). A new technique for reconstruction of the current moment waveform related to a gigantic jet from the magnetic field component recorded by an ELF station. *Radio Science*, *46*(2), RS2016. doi: 10.1029/2010RS004475

Mazur, N. G., Fedorov, E. N., Pilipenko, V. A., & Vakhnina, V. V. (2018). ULF Electromagnetic Field in the Upper Ionosphere Excited by Lightning. *Journal of Geophysical Research (Space Physics)*, *123*(8), 6692-6702. doi: 10.1029/2018JA025622

Młynarczyk, J., Bór, J., Kułak, A., Popek, M., & Kubisz, J. (2015). An unusual sequence of sprites followed by a secondary TLE: An analysis of ELF radio measurements and optical observations. *Journal of Geophysical Research (Space Physics)*, *120*(3), 2241-2254. doi: 10.1002/2014JA020780

Młynarczyk, J., Kułak, A., & Salvador, J. (2017). The Accuracy of Radio Direction Finding in the Extremely Low Frequency Range. *Radio Science*, *52*(10), 1245-1252. doi: 10.1002/2017RS006370

Pasko, V. P., Yair, Y., & Kuo, C.-L. (2012). Lightning Related Transient Luminous Events at High Altitude in the Earth's Atmosphere: Phenomenology, Mechanisms and Effects. *Space Science Reviews*, *168*(1-4), 475-516. doi: 10.1007/s11214-011-9813-9

Plyasov, A. A., Surkov, V. V., Pilipenko, V. A., Fedorov, E. N., & Ignatov, V. N. (2012). Spatial structure of the electromagnetic field inside the ionospheric Alfvén resonator excited by atmospheric lightning activity. *Journal of Geophysical Research (Space Physics)*, *117*(A9), A09306. doi: 10.1029/2012JA017577

Ross, M., Cummer, S. A., Nielsen, T. K., & Zhang, Y. (2008). Simultaneous remote electric and magnetic field measurements of lightning continuing currents. *Journal of Geophysical Research (Atmospheres)*, *113*(D20), D20125. doi: 10.1029/2008JD010294

Shindo, T., & Uman, M. A. (1989). Continuing current in negative cloud-to-ground lightning. *Journal of Geophysical Research (Atmospheres)*, *94*(D4), 5189-5198. doi: 10.1029/JD094iD04p05189

Simões, F., Klenzing, J., Ivanov, S., Pfaff, R., Freudenreich, H., Bilitza, D., ...

Yokoyama, T. (2012). Detection of ionospheric Alfvén resonator signatures in the equatorial ionosphere. *Journal of Geophysical Research (Space Physics)*, *117*(A11), A11305. doi: 10.1029/2012JA017709

Simes, F., Pfaff, R., & Freudenreich, H. (2011). Satellite observations of schumann resonances in the earth's ionosphere. *Geophysical Research Letters*, *38*(22). doi: 10.1029/2011GL049668

Sonnerup, B. U., & Cahill, L. J. (1967). Magnetopause Structure and Attitude from Explorer 12 Observations. *Journal of Geophysical Research*, *72*, 171. doi: 10.1029/JZ072i001p00171

Sonnerup, B. U., & Scheible, M. (1998). Minimum and Maximum Variance Analysis. *ISSI Scientific Reports Series*, *1*, 185-220.

Surkov, V. V., Hayakawa, M., Schekotov, A. Y., Fedorov, E. N., & Molchanov, O. A. (2006). Ionospheric Alfvén resonator excitation due to nearby thunderstorms. *Journal of Geophysical Research (Space Physics)*, *111*(A1), A01303. doi: 10.1029/2005JA011320

Tøffner-Clausen, L., Lesur, V., Olsen, N., & Finlay, C. C. (2016). In-flight scalar calibration and characterisation of the Swarm magnetometry package. *Earth, Planets, and Space*, *68*(1), 129. doi: 10.1186/s40623-016-0501-6

COMPARATIVE STUDY OF THE ENERGETIC ELECTRONS REGISTERED TOGETHER WITH THE BROAD BAND EMISSIONS IN DIFFERENT REGIONS OF THE IONOSPHERE

Jan BŁĘCKI[1], Roman WRONOWSKI[1], Jan SŁOMIŃSKI[1],
Sergey SAVIN[2], Rafał IWAŃSKI[3], Roger HAAGMANS[4]

[1] Space Research Centre, Polish Academy of Sciences, Warsaw, Poland
[2] Space Research Institute RAN, Moscow, Russia
[3] Satellite Remote Sensing Centre, IMWM, Cracow, Poland
[4] ESTEC, Noordwijk, The Netherlands

e-mails: jblecki@cbk.waw.pl, roman@cbk.waw.pl, jan@cbk.waw.pl, ssavin@iki.rssi.ru, iwanski.rafal@gmail.com, Roger.Haagmans@esa.int

ABSTRACT. ELF/VLF waves have been registered in the outer polar cusps simultaneously with high energy electrons fluxes by the satellites Magion 4 (subsatellite to Interball 1), Polar and CLUSTER. Further, we discuss similar observations in the different regions of the ionosphere, where DEMETER registered energetic electrons. The DEMETER satellite operating on the nearly polar orbit at the altitude 650 km crossed different regions in the ionosphere. Registrations of ELF/VLF/HF waves together with the energetic electrons in the polar cusp, in the ionospheric trough and over thunderstorm areas are presented in this paper. The three satellites of ESA's Swarm mission provide additional information on the ELF waves in the mentioned areas together with electron density and temperature. A brief discussion of the generation of these emissions by the so-called "fan instability" (FI) and beam instability is presented.

Keywords: Atmosphere-ionosphere-magnetosphere system, thunderstorms, energetic electrons, ELF/VLF/HF waves, plasma instabilities, DEMETER, Swarm

1. INTRODUCTION

The main reservoirs of energetic particles in the Earth's environment are radiation belts (Van Allen belts) within the magnetosphere. Nevertheless, fluxes of electrons and ions with high energy are registered in many other places of the space surrounding the Earth, even in the atmosphere. The origin of these fluxes is different and some originate from a distant astronomical object even outside our Galaxy. These are galactic cosmic rays. Some of them originate from the Sun and are solar cosmic rays. In this paper, we will present observations of energetic particles together with ELF/VLF/HF plasma waves as a result of the plasma processes going on in the vicinity of Earth. The plasma waves are the most general feature of the plasma environment. These play an important role leading to anomalous processes like diffusion, resistivity, energy redistribution and particle acceleration in collision free space plasma. Different types of waves are present in different regions of space. These are one of the characteristics of these regions with different particle populations. One of the most

interesting regions is the polar cusp. Plasma particles from the magnetosheath directly enter there. The primary types of wave emissions observed in the polar cusp region are: broadband ULF-ELF magnetic noise, whistler mode bursts, broadband electrostatic noise, electron cyclotron harmonics waves, auroral hiss and auroral kilometric radiation. Earlier observations of waves in the polar cusp originate from Hawkeye—in the outer cusp, from Viking in the middle cusp, and from Freya and DE-1 in the lower cusp. These indicate the presence of Alfven, lower hybrid, electron and ion cyclotron waves as the most typical modes in this region of the magnetosphere (Scarf et al., 1972; Gurnett and Frank, 1978; Erlandson et al., 1988; Pottelette et al., 1990). Later, the Polar, Interball and Cluster satellites enabled the discovery of the presence of high energetic particles (electrons and ions) in the polar cusps. Strong wave activity is associated with this population of plasma particles (Chen et al., 1998; Blecki et al., 1999, 2005; Pickett et al., 1999; Savin et al., 2002). Further analysis of the plasma waves and energetic particles by DEMETER satellite in the ionosphere at the altitude 660 km shows the presence of fluxes of energetic electrons together with plasma waves in other areas as the ionospheric trough and over thunderstorms areas. The observations of this type of event are presented in the next sections of this paper: the polar cusp in the third section, the ionospheric trough in the fourth and thunderstorms in the fifth section. The last section is devoted to the brief discussion of the generation mechanism of plasma waves due to instabilities associated with the presence of energetic electron beams.

2. EXPERIMENTAL SYSTEM

To study the presence of energetic particles and their interaction with ionosphere and upper atmosphere, we use the data originating from the DEMETER and Swarm satellites. DEMETER was a low-altitude microsatellite operated from June 2004 until December 2010 in a polar, circular orbit initially at 710 km and slowly decaying to 660 km. DEMETER measured variations of the electric field in the very low frequency (ELF-VLF) range from 0 to 20 kHz and in the high frequency range up to 4 MHz. These measurements were performed in two modes, a survey mode and a burst mode. The spectrum of one electric component is computed on board in the VLF/HF range during both modes. During the burst mode, waveforms of the electric and magnetic field components were transmitted in the range up to 2 kHz (Berthelier et al., 2006; Parrot et al., 2006).

The plasma analyzer instrument measured variations of ion density at a 4 s time resolution. An energetic particle detector measured electrons and protons with energies from 70 keV to 2.34 MeV every 4 s in survey mode or every 1 s in burst mode.

The Swarm satellite constellation is devoted to study the magnetic field of the Earth and the influence of the effects caused by the Sun. It consists of three identical Swarm satellites (A, B, and C), launched on 22 November 2013 into a near-polar orbit. The initial constellation of satellites was formed on April 17, 2014. Satellites A and C are the lower pair flying separated by 1.4° in longitude at the equator at an altitude of about 470 km in 87.30° inclined orbit, Swarm B is operating at a higher orbit initially of about 520 km with an inclination of 87.75°. All three satellites have an identical set of instruments. The absolute scalar magnetometer, vector field magnetometer and Langmuir probe are important for our studies. The magnetometers measure regularly main magnetic field with sampling rates of 1 Hz (absolute value) and 50 Hz (3 vector components). The effects in the ionosphere we are targeting are mainly seen in variations of the electromagnetic fields in a very broad frequency range. Swarm capabilities limit our studies to very low frequencies called ULF (ultra-low frequencies) and ELF (extra low frequencies), and in our case, we are able to analyze them up to 25 Hz. Another instrument, which will be useful for our studies is the Langmuir probe giving information on the electron temperature and concentration. Swarm does not measure

the energetic particle fluxes, but some effect of these fluxes can be seen in the increase of the plasma temperature (Olsen et al., 2013).

3. OBSERVATIONS IN THE POLAR CUSP

Earth's magnetic field can be assumed in first approximation as a dipole field deformed by the stream of solar wind. Topologically, field lines can be divided into two parts according to their location on the sunward or tailward side of the Earth. Between them at the dayside, the polar cusps are located.

These structures are characterized by a depletion magnetic field intensity and it allows a plasma from the magnetosheath to directly enter into the magnetosphere. These regions of the magnetosphere can be considered as key regions for the transfer of mass, momentum and energy from the solar wind into the magnetosphere (e.g., Frank, 1971; Marklund et al., 1990; Yamauchi et al., 1996; Fritz and Zong, 2005; https://wiki.oulu.fi/display/SpaceWiki/Cusps).

The polar cusp can be divided into two parts: the high-altitude cusp, also called outer cusp and the low altitude cusp. The outer polar cusp is usually treated as a part of magnetosphere occupying altitudes over 1500 km, while low altitude cusp is located at ionospheric altitudes. Satellite measurements have shown that the cusp extends about 2.5 hours in local time around noon and about one degree or less in latitude. However, its position can vary between 70° and 80° in geomagnetic latitude and strongly depends on Interplanetary Magnetic Field (IMF) conditions: its direction and intensity and solar wind pressure.

The plasma, many types of waves and turbulent flows find its way to the ionosphere via the outer cusp due to depletion of the magnetic field. The low frequency plasma waves control the dynamics of the ions in collision free plasma and play a very important role in the formation and behavior of this region. Multi-satellite observations demonstrate that the cusp is a locus of accelerated plasma. There is evidence that cusp is a substantial source of energetic particles (Chen et al., 1998; Fritz et al., 1998; Fritz, 2001). The energizing is related to strong turbulence (Błęcki et al., 2001), which was mapped by Interball-1 (Savin et al., 1998, 1999, 2001; Romanov et al., 1999). At the boundary of the inner cusp, the correlation of the low frequency waves with the acceleration of magnetosheath plasma up to ~ 1 keV has been pointed out (Pottelette et al., 1990).

The observed fluxes of accelerated plasma particles, the electron and ion populations with higher temperature than ambient plasma and the very strong wave activity, particularly at low frequencies, suggest the existence of the wave particle interaction processes (Błęcki et al., 2001). One of the finding from the Polar, Interball 1 and Magion 4 satellites is the presence of high-energy particles (ions and electrons) in the outer polar cusp. Strong emissions of the plasma waves are associated with these fluxes (Błęcki et al. 1999; Pickett et al. 1999).

DEMETER satellite has been operating at 660 km altitude with regular crossings of the proper polar cusp. Mainly due to operating scientific instruments in regions with magnetic latitude below 65°, measurements in the polar cusp were performed only occasionally. A French scientific campaign was organized in December 2007 to obtain simultaneous ground base registration on Spitsbergen and on DEMETER. The studies of the waves and particles in the cusp at the ionospheric altitude presented in this paper originate from the time of this campaign.

Swarm satellites with their quasi-polar orbit operate without any gaps and the entire globe is covered by registrations of parameters that are of interest to us. Figure 1 gives an example on April 1, 2016, of electron temperature along a Swarm A orbit shown in the upper panel, electron concentration (black line), electron temperature (red line) both in the middle panel

and magnetic field variations spectra in the bottom panel. The satellite crossed the ionospheric trough (this formation is discussed in next chapter) twice in the northern hemisphere at 20:20 UT and in the southern hemisphere at 21:00 UT. The southern polar cusp was crossed at 21:07 UT. Strong enhancements of the magnetic field variation can be observed both during the crossing of the polar cusp and the ionospheric trough. This wave activity is accompanied by strong variations of the electron temperature and concentration. The increase in plasma density at 20:40 UT and 21:30 UT are associated with crossing of the ionospheric equatorial anomaly.
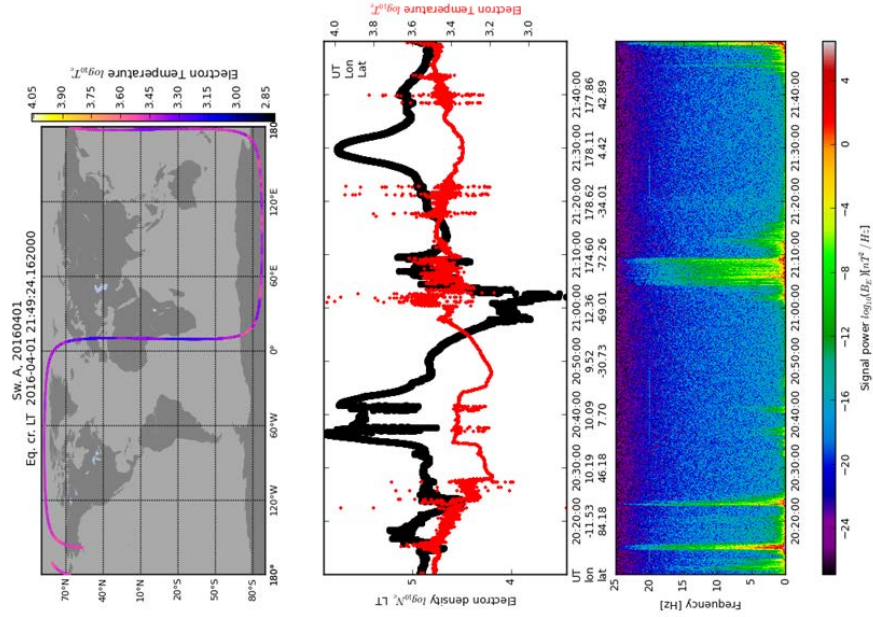
Figure 1. A plot of electron temperature along a complete Swarm A satellite orbit (upper panel) on April 1 2016. The values of the temperature measured along the orbit are shown by dots with different colors. Measurements of the electron temperature (red line) and concentration (black line) are presented in the middle panel. The bottom panel shows the dynamic spectrogram of the magnetic field variations. The registrations were done during geomagnetically very quiet time. Kp was not higher than 1 summary Kp for entire day was 4-, Dst around zero, only days later weak geomagnetic storm appears.

133

Figure 2 presents an example of measurements done by DEMETER on December 10, 2010 in the polar cusp at ionospheric altitude, when an event with strong wave activity and energetic electrons was registered during the ground base French campaign on Spitsbergen. Simultaneously, the DEMETER satellite, which entered polar cusp at 10:07:03 UT, observed these processes in the high latitude ionosphere. This is visible as an increase of the plasma density and the intensity of the wave activity in the ELF and VLF ranges. The exit from polar cusp was at 10:07:28 UT.
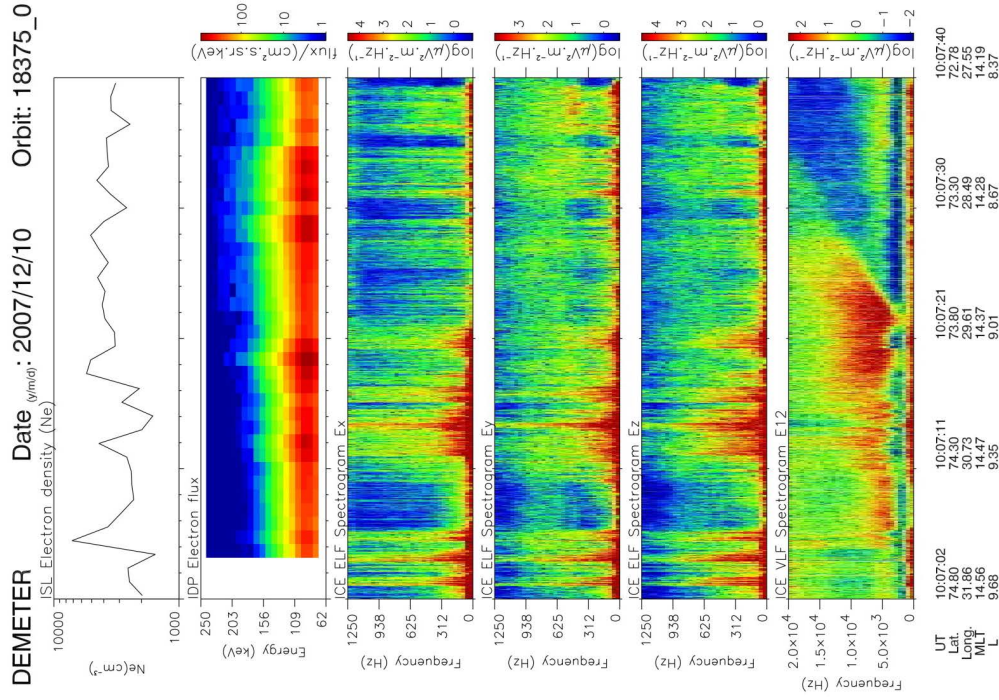
Figure 2. Electron density (upper panel), spectrogram of electron energy (second panel) and wave spectra of three components of the electric field in the ELF range and one component in the VLF range (4 bottom panels) observed by DEMETER in the polar cusp at ionospheric altitude

134

This case as the case from Swarm presented above were registered during very quiet time. Kp index was even lower and maximum value was 0+ and summary 1-. Dst until December 20, when very weak disturbance of this index was registered, fluctuated around zero.

The wave spectra in both frequency ranges indicate strong variability in time, which correspondents to spatial changes that can be associated with internal filamentary structure of the cusp (Błęcki et al., 2003). The broadening into higher energy (~200keV) of the electron spectrograms is clearly visible at 10:07:12 UT, 10:07:20 UT and 10:07:30 UT. At the same time, an increase of ELF emissions in frequency up to 1250 Hz appears. VLF emissions are present during the entire time of the cusp crossing.
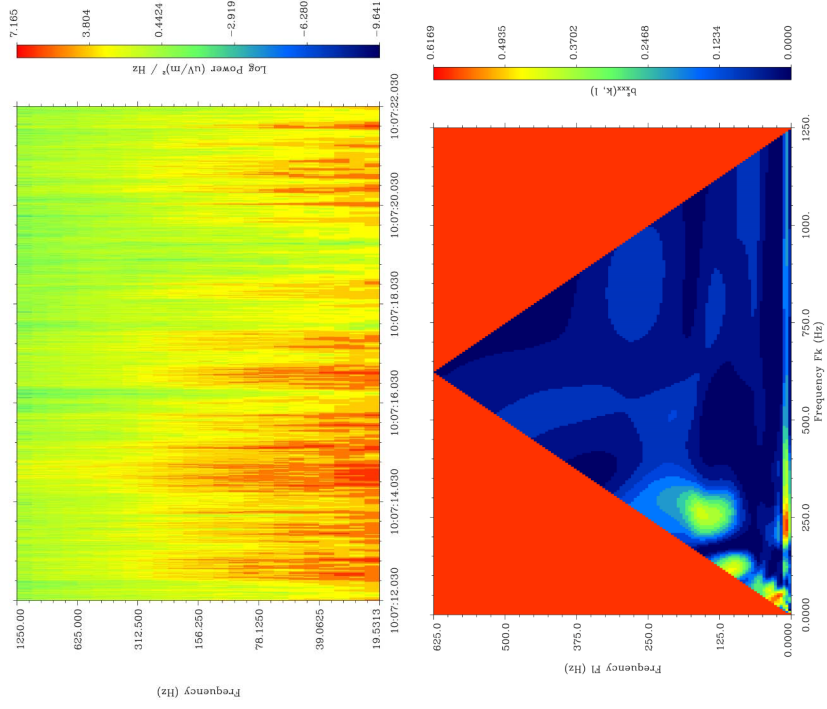

Figure 3. Wavelet spectrogram (19–1250 Hz) of the electric field variations (upper) and bispectrum of the same for time interval 10:07:12–10:07:22 UT when most intensive ELF/VLF emissions were registered (bottom)

The development of the wave processes seen during this event is nonlinear, which can be learned from wavelet and bispectral analysis shown in Figure 3. The same analysis was applied for processes in the outer polar cusp registered by the CLUSTER satellites (Błęcki et al., 2007; Savin et al., 2019). In the latter paper, the horizontal red maximum is associated with nonlinear "pumping" to be effective for the electron acceleration. The red negatively

inclined maximum corresponds to the nonlinear decay at the fixed sum frequency. The nonlinearity observed in higher-order spectra of the ELF wave spectra is shown on the lower Figure 3 where the interactions of three waves in the lowest part of frequency is visible as a maximum of the bispectrum. It leads to spectra broadening in the wavelet spectrogram on the upper part of Figure 3. Similar nonlinear processes were reported in the past for the cases seen in the outer polar cusp (Błęcki et al., 2001).

More detailed information about energetic electrons spectra is provided in Figure 4. One can observe the broadening of spectra in the energy range up to 230 keV at 10:07:16–10:07:30 and 10:07:45–10:08:00 UT. This effect is accompanied by the emissions in the high frequency range 0.5–1.8 MHz as shown in Figure 5. Also, some beams of electrons can be distinguished at 10:07:13, 10:07:18, 10:07:29, 10:07:33 UT around energy 80–90 keV. They can generate beam instability, but we are not able to see it due to upper limit of frequency measured by Demeter.
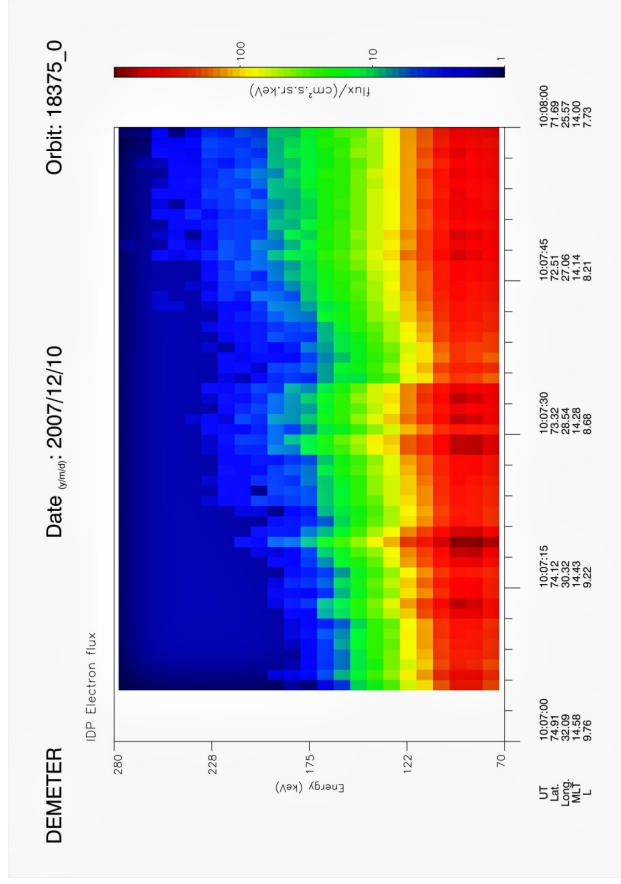

Figure 4 Spectrogram of electron energy from DEMETER in the polar cusp. Fluxes of electrons with energy up to 230 keV are seen at 10:07:16, 10:07:30 and 10:07:45 until 10:08:00 UT The beams of electrons can be distinguished at 10:07:13, 10:07:18, 10:07:29, 10:07:33 UT around energy 80–90keV.

The simultaneous presence of VLF, ELF, HF waves and fluxes of the energetic electrons suggests the following physical picture of these observed processes. The ELF and VLF waves interact in resonance with electrons. This leads to precipitation of the energetic electrons and their generated plasma instabilities creating emissions in the HF range. Two types of instabilities, fan instability and electron beam instability, need to be discussed in relation to the presented observations. A brief discussion is provided in Chapter 6 of this paper.
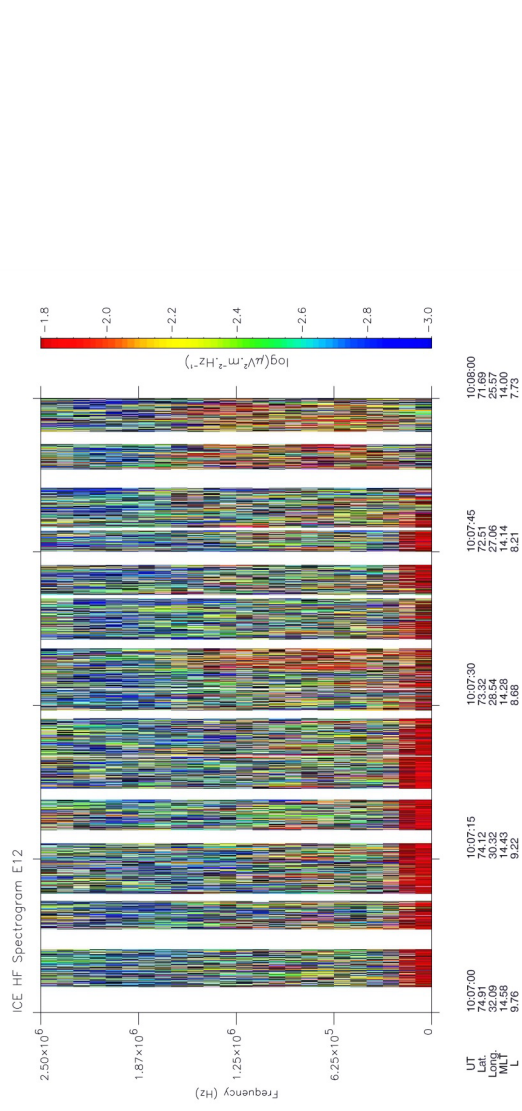
136

Figure 5. High frequency (0.55–1.8 MHz)—electric field variations observed by DEMETER in the polar cusp during an energetic electron event. A good correlation of energetic electrons presence (as shown in Figure 4) with enhancement of HF emissions is apparent at 10:07:30 and 10:07:45–10:08:00 UT. The plasma frequency at this epochs was fpe≈0.8 MHz and electron cyclotron frequency fce≈1.33 MHz.

4. OBSERVATIONS IN THE IONOSPHERIC TROUGH

The ionospheric trough is a location in the high-latitude region of the F layer characterized by distinct depletion of plasma density mostly seen as electron density decrease in the high-latitude ionosphere mainly determined by magnetospheric processes (Moffett and Quegan, 1983). The ionospheric trough width is several degrees in latitude and extends in longitude. The latitude changes with local time from about 70° to 55°. Contrary to polar cusp, which is dayside region, the ionospheric trough is mainly nightside phenomenon, although appears, in weaker form, at all local time (Evans et al., 1983; Collis et al., 1988). It changes its structure and position within time scales of several hours to one day. During increasing geomagnetic activity, the trough moves to lower latitudes. Satellite and ground-based observations allow determination of the large-scale structure of the high-latitude ionosphere, the main ionospheric trough can be imagined as a natural boundary between the middle and subauroral ionosphere. It is associated with another boundary—the boundary between cold plasma escaping from the ionosphere into the plasmasphere and hot plasma in the outer magnetosphere. The ionospheric trough is a projection of this boundary onto the ionosphere (Anderson et al., 2008). A new results related to the structure and its variability were recently obtained from the FORMOSAT-3/COSMIC (Lee et al., 2011) and DEMETER satellites (Rothkaehl et al., 2008; Chen et al., 2018). The ELF/VLF waves strongly interact with energetic electrons from the outer magnetosphere leading to electron precipitation into ionosphere. The energetic electrons fluxes generate high frequency emissions due to the instabilities, as mentioned in the previous chapter (Evans et al., 1983; Collis and Haggstrom,

137

1988). Figures 6 and 7 show the effects of these explained processes observed by DEMETER satellite.
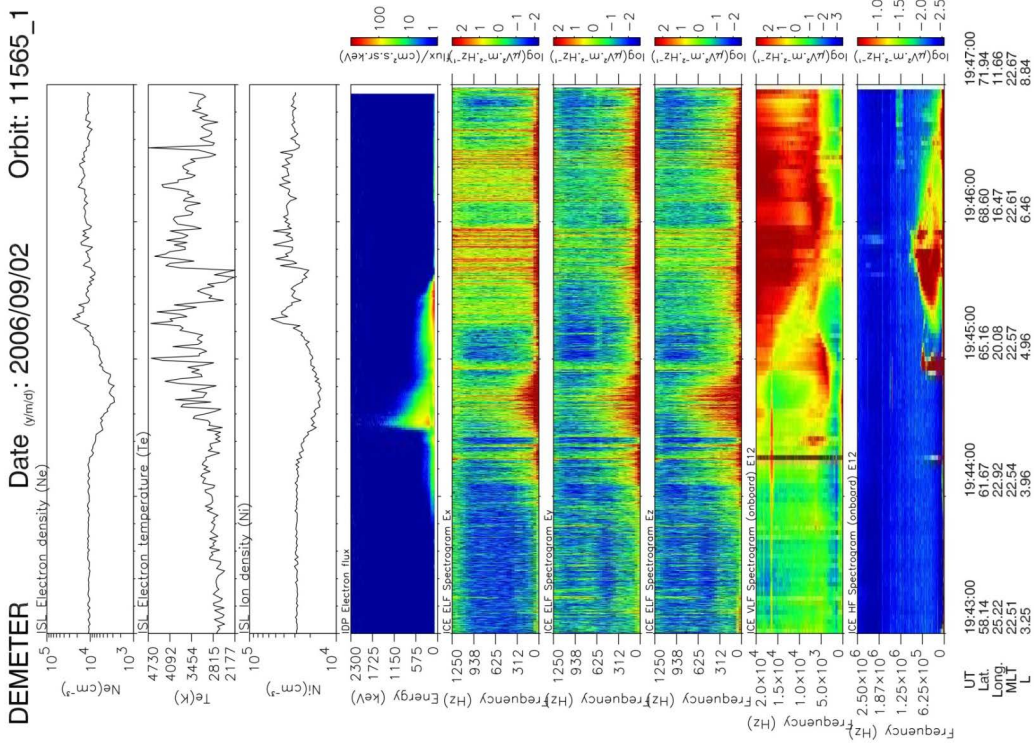

Figure 6. The measurements (from top to bottom) of the electron density, electron temperature, ion density, spectrogram of the electron energy, spectrograms of the electric field variations—three components in ELF, one component in VLF and one in HF frequency range. The entry of DEMETER satellite in the ionospheric trough was around 19:44:00 and exit around 19:45:00 UT

The entry of the satellite on September 6, 2006 into the ionospheric trough results as depletion of electron and ion density and an increase of ELF/VLF wave activity, which reaches a maximum around 19:44:21 UT co-incident with a maximum of the energetic electrons flux.

Strong variations of the electron temperature are present during crossing of the trough. The wavelet and bispectral analysis show the non-linear development and broadening of the wave spectrum. These waves are able to resonantly interact in very broad range with electrons and accelerate them. As one can see in the bottom panel in Figure 6, it leads to the generation of emission in the HF range up to 0.8 MHz (around 19:45:00 UT). The time of this case was related to very weak disturbance of the geomagnetic filed. Kp was 1 during trough crossing by DEMETER.
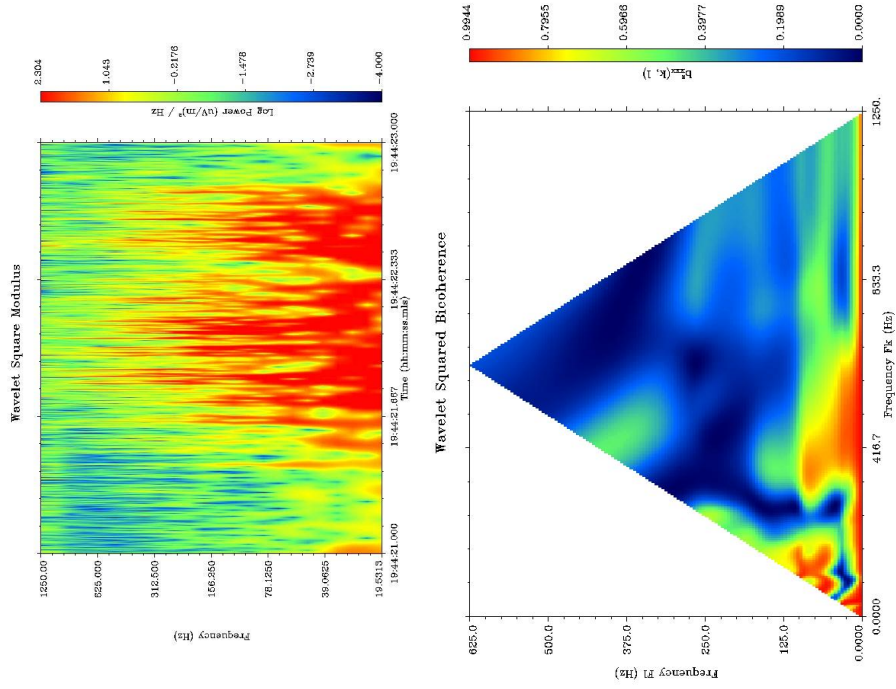

Figure 7. The wavelet spectrogram and bispectrum of ELF electric field variations during the presence of most energetic electrons and the strongest wave activity (19:44:21–19:44:23 UT). Strong nonlinear "pumping" (horizontally spread maxima at fixed vertical frequencies) supports the strong particle heating (cf. Fig. 3).
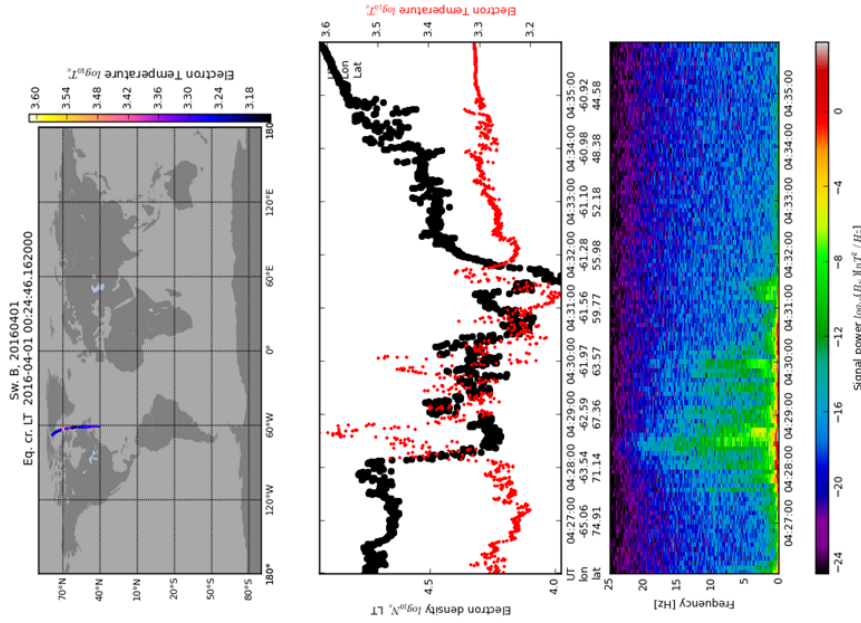
Figure 8. The trough crossing by the Swarm B satellite. The upper panel shows the part of orbit related to measurements presented in the middle and bottom panels. The colors of dots along the orbit correspond to the value of the electron temperature. The plots in the middle panel represent the electron concentration (black line) and temperature (red line). The bottom panel gives the spectrogram of the magnetic field variations.

Swarm satellites crossed the polar trough regularly. As already mentioned, Swarm can measure electron density and temperature, but not energetic particles. These effects, which have been registered by DEMETER as a fluxes of energetic electrons, would only be seen as variation of electron temperature being a consequence of heating of ionospheric plasma by fluxes of energetic electrons. Figure 8 presents an example of a trough crossing on April 1, 2016. As it was mentioned above, it was a very quiet day. The depletion of electron density at 4:28:10 UT indicates the entry of Swarm B into the trough. Its entrance from higher latitude is associated with strong enhancement (at 4:28:15 UT) of ELF waves for frequencies in the lowest part of this range (up to 20 Hz). At the same time, a strong jump of electron temperature (from 1990 K to 3900 K) is visible. Swarm exits the trough at 4:31:30 UT. Much weaker emissions and variations of the temperature are registered at this edge of the trough.

140

5. OBSERVATIONS IN THE IONOSPHERE OVER STRONG THUNDERSTORM

Thunderstorms are one of most powerful, beautiful, but also dangerous natural phenomena. Lightning events are associated with many physical processes of interactions in the atmosphere-ionosphere-magnetosphere system. The separation of the charge in thunderstorm clouds leads to the accumulation of a great amount of energy. This energy is released as lightning discharge on time scales less than 1 sec in a very localized area in space causing formation of plasma channels with temperatures ~25000 K and with electron densities exceeding 10^{17} cm^{-3}. The temperature of plasma in lightning discharge reaches a value higher than that characterizing solar chromosphere. These values are higher than average values measured in Earth's ionosphere.

So a powerful lightning discharge is a source of disturbances in the ionosphere. Lightning is also a source of acoustic gravity waves, which can propagate over long distances without damping creating a good way of energy transfer into the ionosphere.

The DEMETER satellite delivered new results about the influence of thunderstorms, lightning and particularly TLE (Transient Luminous Event) on the ionosphere. The electromagnetic and plasma effects were clearly observed in a broad range of electromagnetic emissions, changes in electron density and temperature and in energetic electron fluxes (Parrot et al., 2008, 2013; Bourriez et al., 2016). Below we discuss an example of DEMETER registrations over a strong thunderstorm in Poland on June 30, 2009. This day was geomagnetically very quiet, Kp index during discussed thunderstorm was on the level 0+, Dst close to zero. So influence on the ionosphere from outer space is negligible in the discussed thunderstorm region. The 136 IC (inter clouds), 89 CG- (cloud to ground negative) and 3 CG+ (cloud to ground positive) discharges has been detected by PERUN system in time interval 19:58–20:03 UT during DEMETER flight above this thunderstorm active region. Table 1 gives the time, locations and values of the maximum current for the most powerful strokes. These parameters are evaluated from the system PERUN run by Institute of Meteorology and Water Management-National Research Institute. The value of the currents during positive cloud to ground discharge on 19:57:54 and 20:00:47 UT could suggest that the effects observed by DEMETER are related to sprite, but there was no optical evidence to support that. Figure 9 presents spectra of the electric field variations in ELF (upper panel) and VLF (lower panel) range during flight over this thunderstorm. The spectrogram of ELF variations is limited only to time interval when burst mode was on. Emissions are present during the entire time of the flight over the thunderstorm area. The characteristic vertical lines in the spectra represent the so called sferics connected with direct transmissions of signal from the lightning discharge to the satellite.

Table 1. The time, locations and values of the maximum current for the most powerful strokes

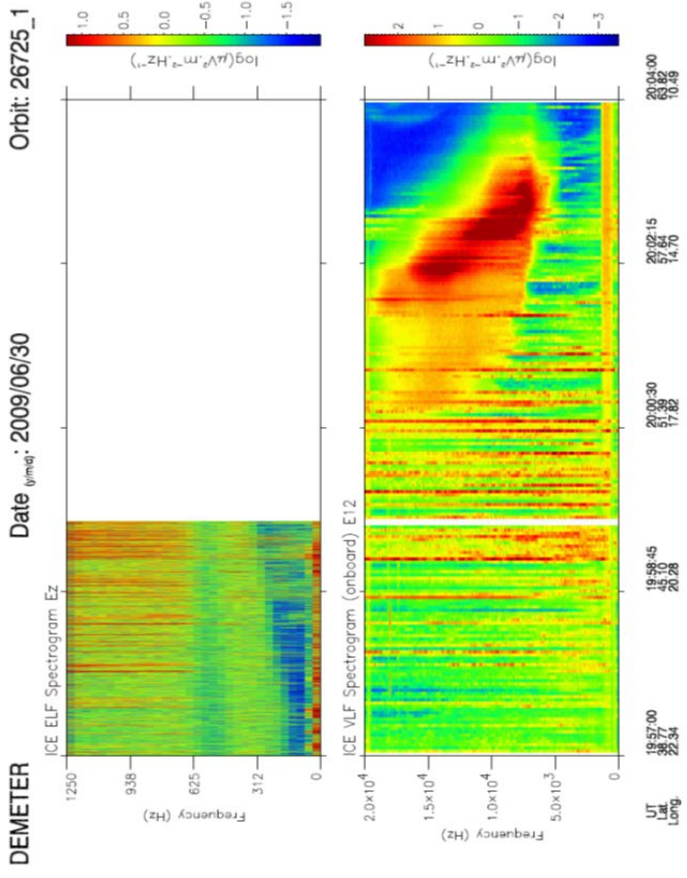| Date	Time UT	Latitude	Longitude	Current max in kA
30/06/2009	19:57:54	52,4105	15,0033	103,380
30/06/2009	20:00:47	53,0546	23,4310	107,170
30/06/2009	20:02:07	51,9554	21,0176	63,700
30/06/2009	20:02:32	52,4673	15,3552	60,980
30/06/2009	20:03:25	52,3102	14,3756	94,850

Figure 9. Spectra of the electric field variations in the ELF (upper panel) and VLF (bottom panel) ranges observed by DEMETER in the ionosphere over strong thunder-storms in Poland. ELF spectra are presented for the time interval related to burst mode.

The detailed spectrograms for this time interval together with ELF wave form are given in Figure 10. Strong variations of electric field up to 0.5 mV/m are present 20:57:54 in the ELF wave form as well as in spectrogram. Developing of VLF whistler following the stroke is seen in the spectrogram in the lower panel of Fig 10. Second very short impulse appears 4 seconds later and reaches value more than 0.6 mV/m, which is not related to any registrations by PERUN system. The characteristic delay of the ELF waves in relation to VLF in order of 0.05 sec is due to dispersion of the velocity, which is proportional to square root of the wave frequency.
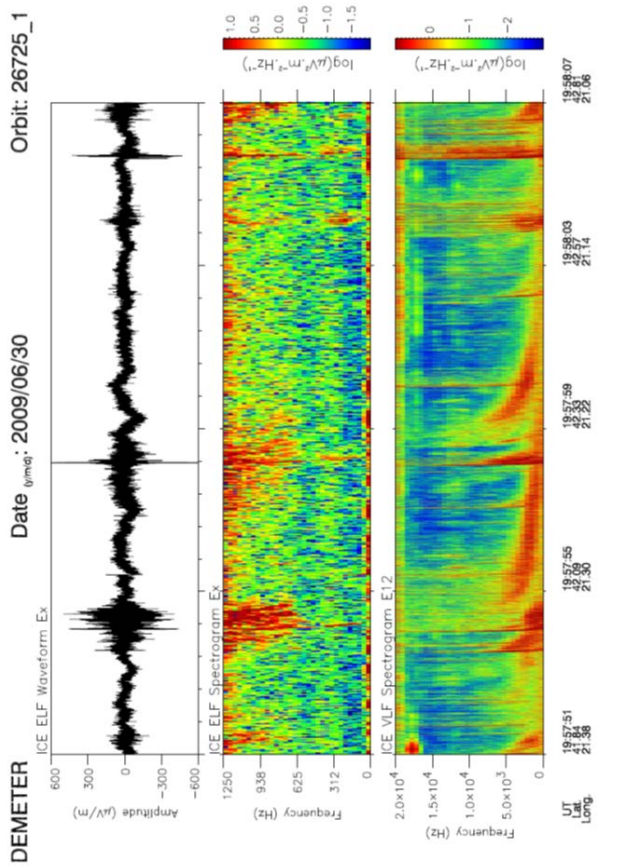
142

Figure 10. The wave form of the ELF electric field variations (upper panel) and spectrogram of it (middle panel) and spectrogram of VLF—whistler waves (bottom panel).

Figure 11 presents the measurements of the electron temperature, the energetic electrons spectrum, the energetic electron flux together with spectrograms of the VLF variations of the electric field and HF (high frequency) electromagnetic emissions. The spectrogram of the high frequency waves in this area is shown in the bottom panel of Figure 11. The strong enhancements of the HF wave intensity and broadening of the spectra up to 0.25 MHz are present in time interval 20:00:30–20:00:45 when Perun did not registered any CG discharge, but many interclouds ones. The electron temperature increases at 20:00:30 and 20:00:45 UT are present. Broadening of HF and VLF spectra appears after that shortly.

Weak enhancements of the energetic electrons fluxes are seen at 20:01:58 and 20:02:30 UT, the second one is also seen in the spectrogram with energy up to 122 keV. The presence of the energetic electrons in the ionosphere above the thunderstorm areas is well known experimental fact and were reported in many papers (see, e.g., Fullekrug et al, 2013). Their origin is related to the precipitation of energetic electrons from radiation belts due to resonant interaction of the VLF waves with trapped electrons.

Strong enhancements are seen in VLF spectrograms in band around 15 kHz in first case and around 10 kHz and is associated with this precipitation. Another effect is the action of the energetic electrons with ionospheric plasma and generation of plasma instability. It is shortly discussed in the next part.
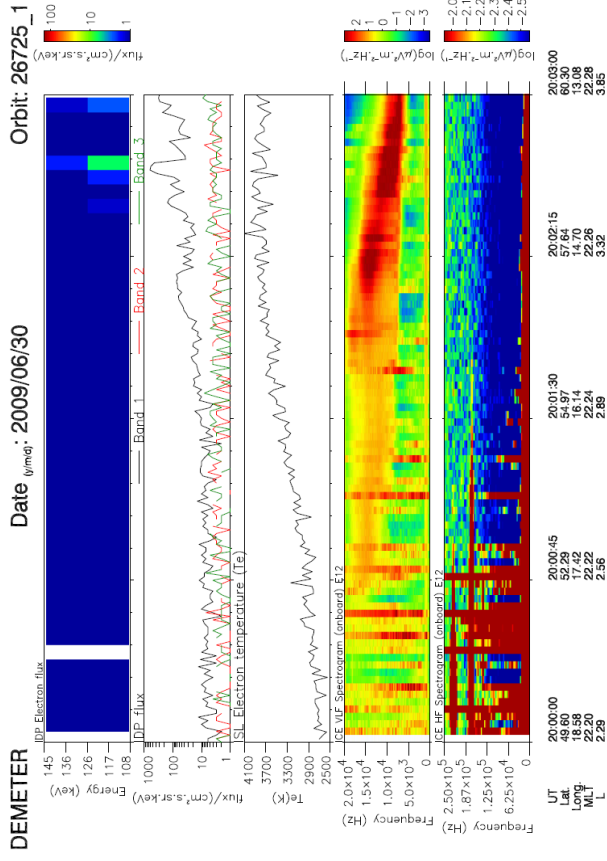
Figure 11. The parameters of ionospheric plasma at 660 km altitude observed by DEMETER together with VLF and HF over thunderstorms in Poland on June 30, 2009. The panels present from the top to the bottom: energetic electrons energy spectrum, integrated flux of energetic electrons in three ranges: band 1 – 971-2350 keV, band 2 – 526-971 keV and band 3 – 72-526 keV, electron temperature and spectrograms of VLF and HF emissions.

6. DISCUSSION

The presented observations of simultaneous presence of energetic electrons and plasma waves in different regions of the near-Earth space from the DEMETER and Swarm satellites can be interpreted as a development of an unstable plasma state. All these events were registered during very quiet geomagnetic conditions. It can suggest that registered effects are associated with internal conditions in the discussed structures (polar cusp, ionospheric trough, lightning) and no influence from outer space. One can consider taking into account the presence of energetic electrons fluxes, two types of plasma instabilities—fan instability and beam instability. These are briefly discussed in the next two subsections.

6.1. Fan instability

Kadomtsev and Pogutse (1967) first studied this instability for a case where energetic electrons were present in Tokamak. Omelchenko (1994) and Vaivads (1995) discussed this phenomenon in relation to the auroral region, Krafft and Volokitin (2003) for the solar wind and Savin (2004) in case of the magnetopause.

A particle beam along magnetic field lines is needed to develop this instability, but in contrast to the usual beam-plasma instabilities, it does not require a threshold in relative velocity and a positive slope in the distribution function. The presence of the long superthermal tail in the

144

distribution function is enough for developing of this instability. This condition is relevant to observations of DEMETER inside energetic particles fluxes. The maximum intensity seen in the wave spectrogram is related to the maximum of growth rate of the instability, which was calculated in the aforementioned theoretical works and would appear in the ionosphere at frequency of 0.2 $\omega_{ce} < \omega < 0.4\ \omega_{ce}$, It results in values at DEMETER altitude between 0.256 and 0.512 MHz in the ionosphere above a thunderstorm and 0.56 to 1.12 MHz in polar regions. This condition is in good agreement with the spectra of the high frequency emissions shown in figures 5, 6 and 11.

6.2 Beam instability

The presence of fluxes of the energetic electrons on a background of thermal plasma suggests the possibility of another instability: beam instability. This instability can develop when the strong beam of electrons is present on a background of ambient, thermal plasma. The threshold for the development of it is associated with the velocity of the beam. This should be higher than the thermal plasma velocity. This condition is fulfilled in the cases considered in the previous chapters. Beams of electrons can be distinguished at 10:07:13, 10:07:18, 10:07:29, 10:07:33 UT around energy 80–90 keV in Fig. 4. They can generate beam instability, with frequencies of waves around the local plasma frequency (cf. Treumann and Baumjohann 1997), but we are not able to see them, because it is over upper limit of frequency measured by DEMETER.

7. SUMMARY AND CONCLUSIONS

This paper presents observations of waves appearing together with plasma and energetic electrons in the polar cusp, ionospheric trough and over thunderstorms from the DEMETER satellite. These show that broad band (ELF/VLF/HF) wave phenomena can occur in these regions when energetic electrons are present. The same type of event was reported for the outer polar cusp observed by Prognoz 8, Magion 4 and CLUSTER satellites (Błęcki et al., 2005, 2006). The interpretation of the observations suggests multi-steps processes. ELF/VLF waves resonantly interact with energetic particles (electrons) in the magnetosphere, which leads to precipitation of electrons into the ionosphere. The next step is the stimulation of plasma instabilities. In the presented cases, two types of instabilities can develop generating HF waves. These are: fan and beam instability. Previous registrations done by CLUSTER and Interball show that fan instability should be seen as one of the important mechanism of waves generation in the outer polar cusp responsible for the redistribution of the energy in cusp plasma. The results from DEMETER presented in the present paper confirm that frequencies of registered waves are in the ranges related to prediction based on the theory of these instabilities. The plasma frequency calculated on the basis of the electrons concentration in examined regions is in the range from 0.6 MHz in polar cusp to 3.6 MHz over thunderstorm, while the electron cyclotron frequency from 2.8 MHz to 1.28 MHz respectively. These values correspond to the registrations given in figures 5, 6 and 11. Swarm satellites cannot perform directed measurements of energetic particles, but results presented in figures 1 and 8 contain the information about strong variations of the electron temperature and density, which are considered to result from the aforementioned processes.

REFERENCES

Anderson, P. C., Johnston, W. R., and Goldstein, J. (2008). Observations of the ionospheric projection of the plasmapause. *Geophysical Research Letters*, 35, L15110. https://doi.org/10.1029/2008GL033978

Berthelier, J.J., Godefroy, M., Leblanc, F., Malingre, M., Menvielle, M., Lagoutte, D., Brochot, J.Y., Colin, F., Elie, F., Legendre, C., Zamora, P., Benoist, D., Chapuis, Y., Artru, J. And Pfaff, R., (2006), ICE – the electric field experiment on DEMETER. *Planetary and Space Science*, 54, pp. 456–471.

Bourriez F., J.-A. Sauvaud, J.-L. Pinçon, J.-J. Berthelier, and M. Parrot, (2016), A statistical study over Europe of the relative locations of lightning and associated energetic burst of electrons from the radiation belt, *Ann. Geophys.*, 34, 157–164, doi:10.5194/angeo-34-157-2016

Błęcki J., K.Kossacki, R.Wronowski, Z.Nemecek, J.Safrankowa, S.Savin, J.A.Sauvaud, S. Roma-nov, J. Juchniewicz, S.Klimov, P.Triska, J.Smilauer, J.Simunek, (1999), Low Frequency Plasma Waves Observed In The Outer Polar Cusp, *Adv.in Space. Res.*, 23, No 10, 1765.

Błęcki J., S. Savin, H. Rothkaehl, K. Stasiewicz, R. Wronowski, Z. Nemecek, J.Safrankowa, K.Kudela, (2001), Wave–Particle Interaction In The Polar Cusp in "*Multiscale and multipoint measurements in space plasmas*" ESA, SP-492 , pp 87–92, Nordwijk.

Błęcki J., S. Savin, N. Cornilleau-Wehrlin, K. Kossacki, M. Parrot, H. Rothkaehl, K. Stasiewicz, R. Wronowski, O. Santolik, J-A. Sauvaud, (2003), Fine Structure Of The Polar Cusp As Deduced From The Plasma Wave And Plasma Measurements, *Adv. Space Res.*, 32, No 3, pp. 315–321..

Błęcki J., S.Savin, N.Cornilleau-Wehrlin, K.Kossacki, M.Parrot, Z.Nemecek, J.Safrankova, R. Wronowski, K. Kudela, O. Santolik, (2005), The Low Frequency Plasma Waves In The Outer Polar Cusp – Review Of Observations From Prognoz 8, Magion 4, Interball 1 And Cluster Satellites, *Survey in Geophysics*, 26, 177–191.

Błęcki J., N. Cornilleau-Wehrlin, M. Parrot, S. Savin, E. Amata, R. Bucik, R. Wronowski, (2006) Instability Of The Energetic Electron Beams In The Polar Cusp-Observations By Cluster And Interball-1, in *Proceedings of the Symposium 5th Years of CLUSTER in Space*, SP-598, ESA, Noordwijk (cd-rom).

Błęcki J., S. Savin, M. Parrot, R. Wronowski, (2007), Nonlinear Interactions of the Low Frequency Plasma Waves in the Middle-altitude Polar Cusp as Observed by Prognoz-8, Interball-1 and Cluster Satellites, *Acta Geophysica*, 55, no. 4, pp. 459-468,

Chen C. Y., Tiger J. Y. Liu, I. T. Lee, H. Rothkaehl, D. Przepiorka, Loren C. Chang, B. Matyjasiak, K. Ryu, and K.-I. Oyama, The Midlatitude Trough and the Plasmapause in the Nighttime Iono-sphere Simultaneously Observed by DEMETER During 2006–2009, (2018) *Journal of Geophysical Research: Space Physics*, 123, 5917–5932. https://doi.org/10.1029/2017JA024840

Chen, J., Fritz, T. A., Sheldon, R. B., Spence, H. E., Spjeldvik, W. N., Fennell, J. F., Livi,S., Russell, C. T., Pickett, J. S., and Gurnett, D. A.:, (1998), 'Cusp Energetic Particle Events: Implications for a Major Acceleration Region in Magnetosphere', *J. Geophys. Res.* 103, 69–78.

Collis, P. N., and I. Häggström, (1988), Plasma convection and auroral precipitation processes as-sociated with the main ionospheric trough at high latitudes, *J. Atmos. Terr. Phys.*, 50, 389–404.

Evans, J. V., J. M. Holt, W. L. Oliver, and R. H. Wand, (1983), On the formation of daytime troughs in the F-region within the plasmasphere, *Geophys. Res. Lett.*, 10, 405–408.

Frank, L.A., ((1971), Plasma in the Earth's Polar Magnetosphere, *J. Geophys. Res.*, 76, 5202–5219.

Fritz, T.A., J. Chen, R.B. Sheldon, H.E. Spence, J.F. Fennell, S. Livim, C.T. Russell and J.S. Pickett, (1999), Cusp Energetic Particle Events Measured by POLAR Spacecraft, *Phys. Chem. Earth* (C), 24, 135.

Fritz, T.A., (2001), The Cusp as a Source of Magnetospheric Energetic Particles, Currents, and Electric Fields: A New Paradigm, *Space Science Reviews*, 95: 469. https://doi.org/10.1023/A:1005286908441.

Fritz T. A. and Q. G. Zong, (2005), The Magnetospheric Cusps: A Summary, *Surveys in Geophysics*, 26: 409–414, DOI 10.1007/s10712-005-1904-2.

Fullekrug M., Declan Diver, Jean-Louis Pincon, Alan D. R. Phelps, Anne Bourdon, Christiane Helling, Elisabeth Blanc, Farideh Honary, R. Giles Harrison, Jean-Andre Sauvaud, Jean-Baptiste Re-nard, Mark Lester, Michael Rycroft, Mike Kosch, Richard B. Horne, Serge Soula, Stephane Gaffet, Energetic Charged Particles Above Thunderclouds, (2013), *Surveys in Geophysics*, 34:1–41, DOI 10.1007/s10712-012-9205-z

Gurnett, D. A., Frank, L. A., (1978), Plasma waves in the polar cusp: Observations from Hawkeye 1, *J. Geophys. Res.* 83, 1447–1462..

Kadomtsev, B. B. and Pogutse, O. P., (1967): Electric conductivity of a plasma in a strong magnet-ic field, *Soviet Phys. JETP*, Vol. 26, 1146..

Krafft C. and A. Volokitin (2003), Interaction of suprathermal solar wind electron fluxes with sheared whistler waves: fan instability, *Annales Geophysicae*, 21: 1393–1403.

Lee, I. T., Wang, W., Liu, J. Y., Chen, C. Y., & Lin, C. H. (2011). The ionospheric midlatitude trough observed by FORMOSAT-3/COSMIC during solar minimum, *J.Geophys. Res.*, 116, A06311. https://doi.org/10.1029/2010JA015544

Marklund, G. T., L. G. Blomberg, C.-G. Fälthammar, R. E. Erlandson, and T. A. Potemra, (1990), Signatures of the high-altitude polar cusp and dayside auroral regions as seen by the Viking electric field experiment, *J. Geophys. Res.*, 95, 5767–5780.

Moffett, R. J., & Quegan, S. (1983). The midlatitude trough in the electron concentration of the ionospheric F-layer: A review of observations and modeling, *J. Atmos. Terr. Phys.*, 45(5), 315–343. https://doi.org/10.1016/S0021-9169(83)80038-5

Olsen N, Friis-Christensen E, Floberghagen R, Alken P, Beggan CD, Chulliat A, Doornbos E, Teixeira da Encarnacao J, Hamilton B, Hulot G, van den IJssel J, Kuvshinov A, Lesur V, Lühr H, Macmillan S, Maus S, Noja M, Olsen PEH, Park J, Plank G, Püthe C, Rauberg J, Ritter P, Rother M, Sabaka TJ, Schachtschneider R, Sirol O, Stolle C, Thebault E, Thomson AWP, Tøffner-Clausen L, Velimsky, J, Vigneron P, Visser P N, (2013), The Swarm Satellite Constellation Application and Re-search Facility (SCARF) and Swarm data products, *Earth Planets Space*, 65:1189–1200, doi:10.5047/eps.2013.07.001.

Omelchenko, Yu., (1994): Modified lower hybrid fan instability excited by precipitating auroral electrons, *J. Geophys. Res.*, 99, 5965–5976.

Parrot M., D. Benoist, J.J. Berthelier, J.Błęcki, Y.Chapuis, F.Colin, F. Elie, P. Fergeau, D. Lagoutte, F. Lefeuvre, M. Lévêque, J.L. Pinçon, H-C. Seran, P. Zamora, (2006), The magnetic field experiment and its data processing onboard DEMETER: scientific objectives, description and first results, *Planetary and Space Science*, 54, 441–455.

Parrot M., J. A. Sauvaud, S. Soula, J. L. Pinçon, and O. van der Velde, Ionospheric density perturbations recorded by DEMETER above intense thunderstorms, *J. Geophys. Res.*, (2013), 118, 5169–5176, doi:10.1002/jgra.50460.

Parrot M., J.J. Berthelier, J.P. Lebreton, R. Treumann, J.L. Rauch, (2008), DEMETER Observations of EM Emissions Related to Thunderstorms, *Space Sci Rev*, 137: 511–519, DOI 10.1007/s11214-008-9347-y

Pickett, J.S., et al., (1999), Plasma waves observed during cusp energetic particle events, *Adv.in Space Res.*, 24, 23–34.

Pottelette, R., Malingre, M., Dubouloz, N. et al., (1990), High-frequency waves in the Cusp/Cleft regions, *J. Geophys. Res.*, 95, 5957–5971.

Quegan, S., Bailey, G. J., Moffett, R. J., Heelis, R. A., Fuller-Rowell, T. J., Rees, D., & Spiro, R. W. (1982). A theoretical study of the distribution of ionization in the high-latitude ionosphere and the plasmasphere: First results on the mid-latitude trough and the light-ion trough, *J. Atmos. Terr. Phys.*, 44(7), 619–640. https://doi.org/10.1016/0021-9169(82)90073-3

Roger, A. S., R. J. Moffett, and S. Quegan, (1992), The role of ion drift in the formation of the ionization troughs in the mid- and high-latitude ionosphere - a review, *J. Atmos. Terr. Phys.*, 54, 1–30.

Rothkaehl, H., Krankowski, A., Stanislawska, I., Błęcki, J., Parrot, M., Berthelier, J.-J., & Lebreton, J.-P. (2008). Wave and plasma measurements and GPS diagnostics of the main ionospheric trough as a hybrid method used for space weather purposes, *Annales Geophysicae*, 26(2), 295–304. https://doi.org/10.5194/angeo-26-295-2008

Savin, S., J. Błęcki, N. Pissarenko, V. Lutsenko, I. Kirpichev, E. Budnik, N. Borodkova,M. Nozdrachev, L. Zelenyi, V. Romanov, I. Sandahl, J.A. Sauvaud, C.T. Russell, J. Buechner, B. Nikutowski, G. Gustafsson, K. Stasiewicz and V. Korepanov, (2002), Accelerated particles from turbulent boundary layer, *Adv. Space Res.*, 30, 2821–2830.

Savin S., (2004), *Experimental studies of the nonlinear interactions and processes of the transport in the critical regions at the magnetopause*, doctoral dissertation, (in Russian), Moscow.

S. Savin, E.Amata, L. Zelenyi, C. Wang, H. Li, B. Tang, G. Pallocchi, J. Safrankova, Z. Nemecek, S. Sharma, F. Marcucci, L. Kozak , J. L. Rauch, V. Budaeva, J. Blecki, L. Legen, M. Nozdrachev, (2019), Collisionless Plasma Processes at Magnetospheric Boundaries: Role of Strong Nonlinear Wave Interactions, ISSN 0021-3640, *JETP Letters*. DOI: 10.1134/S0021364019170028

Scarf, F. L., Fredricks, R. W., Green, I. M., Russell, C. T., (1972), Plasma waves in the dayside polar cusp 1. Magnetospheric observations, *J. Geophys. Res.*, 77, 2274–2293.

David Shklyar and Hiroshi Matsumoto, (2009), Oblique Whistler-Mode Waves in the Inhomogeneous Magnetospheric Plasma: Resonant Interactions with Energetic Charged Particles, *Surv. Geophys.*, 30, 55–104, DOI 10.1007/s10712-009-9061-7.

Treumann R.A. and W. Baumjohann, (1997), *Advanced space plasma physics*, Imperial College Press, London.

Vaivads, A., et al., (1995), Generation of ion acoustic waves by fan instability, *J. Geophys. Res.*, 100, 19435–19440.

Yamauchi, M., H. Nilsson, L. Eliasson, O. Norberg, M. Boehm, J. H. Clemmons, R. P. Lepping, L. Blomberg, S.-I. Ohtani, T. Yamamoto, T. Mukai, T. Terasawa, and S. Kokubun, (1996), Dynamic response of the cusp morphology to the solar wind: A case study during passage of the solar wind plasma cloud on February 21, 1994, *J. Geophys. Res.*, 101, 24675–24687.